INVESTIGATION OF MULTISCALE DAMAGE INITIATION AND PROPAGATION CAPABILITIES

A Dissertation

Presented to the Faculty of the Graduate School

of Cornell University

In Partial Fulfillment of the Requirements for the Degree of

Doctor of Philosophy

by

Albert Rosario Cerrone III

August 2014

INVESTIGATION OF MULTISCALE DAMAGE INITIATION AND PROPAGATION CAPABILITIES

Albert Rosario Cerrone III, Ph. D.

Cornell University 2014

Fracture is largely a microstructure-based phenomenon, but for experimentalists, computational mechanicians, and fleet managers operating at the macroscale, this fact might seem inexplicable, inapplicable, or even inconsequential. The latter response is what the three chapters of this dissertation address. Together, they attempt to dispel the notion that microstructural effects do not translate in any useful way to the structural scale. They also present models which are verified and validated herein to ease this disconnect. These three chapters are individual papers submitted to refereed journals for publication.

The paper in the first chapter appears in Engineering Fracture Mechanics (DOI: http://dx.doi.org/10.1016/j.engfracmech.2014.03.010). It generalizes the Park-Paulino-Roesler potential-based cohesive zone model to three-dimensions, a means to model fracture even under a high degree of mode-mixity at both the macro- and micro-scales. The generalization is validated against several material tests at the macroscale: T-Peel, MMB, ECT, and BDWT. Its ability to model intergranular fracture at the microscale is also explored.

The paper in the second chapter fills a void in the Digital Twin community— it presents for the first time a straight-forward use case which both clarifies and motivates this new paradigm in fleet management. Specifically, ductile fracture is modeled in a non-standardized specimen which fails along one of two likely crack paths. This crack

path ambiguity, the result of grain-size deviations in specimen geometry, underpins the importance of considering as-manufactured component geometry in the design, assessment, and certification of structural systems, a cornerstone of Digital Twin. It also highlights the limitations of a continuum plasticity damage model in resolving accurately this ambiguity particularly close to the bifurcation, on the order of a few grain sizes, and motivates the need to consider crack nucleation at the microscale.

The paper in the third chapter demonstrates Digital Twin at the microscale. It details the implementation, verification, and validation of a microstructure-based, Digital Twin framework which accounts for the predominant microcrack nucleation mechanism in the nickel-based superalloy LSHR. Also included is an extensive grain boundary analysis, an investigation that would otherwise be impossible to conduct to any appreciable fidelity without the as-processed, Digital Twin microstructural model.

BIOGRAPHICAL SKETCH

Albert Cerrone III was born and raised in Petaluma, California on November 14, 1986 to parents Albert (Jr.) and Margaret alongside identical twin Daniel. With Daniel, he graduated co-valedictorian from St. Vincent de Paul High School in June 2005. From there, he enrolled in undergraduate studies at the University of Notre Dame where he earned a Bachelor of Science in Civil Engineering and a minor in theology, graduating in 2009. Following his undergraduate studies, he enrolled in graduate studies at Cornell University and joined the Cornell Fracture Group not long after. His Ph.D. research, presented in this dissertation, was focused in computational fracture mechanics and microstructure-based failure prediction and advised by Professor Anthony Ingraffea, with Professor Alan Zehnder, Professor Derek Warner, and Professor Anthony Rollett as minor advisors.

To Aunt Lilly, in Heaven

All things are ready, if our minds be so.

Henry V (4.3.2307)

ACKNOWLEDGEMENTS

First and foremost, I would like to acknowledge my Cornell Fracture Group family. I thank my advisor, Professor Anthony Ingraffea, a fellow Domer, for giving me four particular items: a long leash to explore and mature as an engineer, friendship, confidence, and unfettered access to amazing people. I acknowledge Gerd Heber, my Skype / Lync / Google Hangout buddy of five years, for always satisfying my mathematical and philosophical curiosities. I thank Bruce Carter for having an overabundance of patience— my incessant programming questions and dry sense of humor would have drove anyone else crazy. I thank Brett Davis and Ashley Spear and former colleagues Michael Veilleux and Jacob Hochhalter for being amazing coworkers and even better friends. I also thank my minor committee advisors, Professor Derek Warner, Professor Alan Zehnder, and Professor Anthony Rollett for their guidance, advice, and the courses they taught which shaped me greatly as a young graduate student. I also acknowledge the several visitors the group has hosted, in particular Aida Nonn, Silvia Corbani, Markos Oliveira Freitas, Joaquim Bento Cavalcante-Neto, and Niko Weber, whom I have the privilege to call lifelong friends.

I would also like to acknowledge the many sources of funding from which I have benefited greatly. First, I thank the Air Force Office of Scientific Research, especially Dr. David Stargel, for funding a large majority of this effort under grant number FA9550-10-1-0213. I acknowledge the XSEDE Science Gateways program, supported by the National Science Foundation, for access to Texas Advanced Computing Center's supercomputer Stampede on allocation TG-MSS110031. I also thank Dr. Bernard Ross of Exponent for sponsoring the Ross-Tetelman Fellowship at Cornell University, of which I was a proud recipient.

I thank the many collaborators who helped make this work a reality. In particular, I acknowledge Professor Anthony Rollett of Carnegie Mellon University for his

hospitality whenever I visited his group in Pittsburgh, his hundreds of e-mails offering priceless technical advice, and allowing me to work with his exceptional students Joe Tucker and Clay Stein, who I also thank for a tremendous collaboration. I thank Devin Pyle of RPI and Saikumar Reddy Yeratapally of Purdue University for our many tech-related e-mail threads, telecons, and Skype sessions. I also thank Dr. Ahmet Kaya and Dr. Adrian Loghin of GE Global Research (Niskayuna) for making my internships at GE edifying and enjoyable experiences. I also acknowledge all of the users of my polycrystal meshing program— it has been a joy to help you all.

Most importantly, I owe an unpayable debt to my family. I thank my mom and dad for catapulting me and my brother, first-generation college students, to heights I never envisioned as a kid. I thank you, mom, for enduring your sons' hijinks still to this day, and always doing it with a smile. I thank you, dad, for reminding me "It's Bobby Orr Time" whenever I needed the pick-me-up. Finally, I thank my best friend, my identical twin Daniel. I only hope to progress as far in my field as you will undoubtedly progress in pediatrics.

TABLE OF CONTENTS

LIST OF FIGURES

LIST OF TABLES

LIST OF ABBREVIATIONS

ALA	as-large-as
APS	Advanced Photon Source
BDWT	Battelle drop-weight tear test
CP-FEM	crystal-plastic, finite element method
CZM	cohesive zone model
ECT	edge crack torsion
FCC	face-centered cubic
FEAWD	finite element all-wheel drive
GBCD	grain boundary character distribution
HCF	high-cycle fatigue
LCF	low-cycle fatigue
LSHR	low-solvus, high-refractory
MMB	mixed-mode bending
nf-HEDM	near-field high energy X-ray diffraction microscopy
PETSc	Portable, Extensible Toolkit for Scientific Computation
PPR	Park-Paulino-Roesler
PSB	persistent slip band
SFC	Sandia Fracture Challenge
VVUQ	verification, validation, uncertainty quantification

LIST OF SYMBOLS

$\boldsymbol{b}$	vector aligned with Burgers vector
$\boldsymbol{B}$	strain-displacement matrix
$\boldsymbol{C}$	fourth order elasticity tensor
c	concentration
$\boldsymbol{D}$	material tangent stiffness matrix
D	coupled damage parameter
d	average grain size
$\boldsymbol{E^e}$	Green elastic strain tensor
E	Young's modulus
$\boldsymbol{F}$	deformation gradient
$\boldsymbol{F^e}$	elastic deformation gradient
$\boldsymbol{F^p}$	plastic deformation gradient
$\boldsymbol{f}$	internal force vector
f	void/particle volume fraction
f_c	critical void volume fraction
f_f	void volume fraction at total failure
f_N	volume fraction of nucleated voids
g	hardness
G_o	hardening parameter
g_o	critical resolved shear stress
g_s	saturation strength
H_o	hardening parameter
$\boldsymbol{J}$	Jacobian
J_3	third invariant of the deviatoric stress tensor
K	stiffness matrix
K	strength coefficient, bulk modulus
k	fitting parameter, strengthening constant
L	slip line length
M	polycrystalline Taylor factor
m, n	non-dimensional exponents
m	Schmid factor, strain rate sensitivity
N_1, N_2, N_3, N_4	shape functions for 8-noded cohesive element
N_{SS}	number of slip systems
N_{SP}	number of slip planes
$\boldsymbol{n}_{GB}$	grain boundary normal
$\boldsymbol{n}_p$	slip plane normal
n, t1, t2	opening and sliding directions
$\boldsymbol{P}$	Schmid tensor
q_1, q_2, q_3	yield surface parameters
r	relative density, particle radius
$\boldsymbol{S}$	2nd Piola-Kirchhoff stress tensor
s_N	standard deviation of nucleation strain

T_{n}	normal cohesive traction
T_{t}	effective tangential cohesive traction
T_{t1}, T_{t2}	tangential cohesive tractions in sliding directions
$T_{max\ coupled}$	coupled cohesive strength
$\boldsymbol{t}$	traction vector, vector aligned with loading direction
t	stress triaxiality below which damage is induced manually
α, β	shape parameters
Γ_{n}, Γ_{t}	energy constants
Γ_{APB}	antiphase boundary energy
$\dot{\gamma}$	slip rate
Δ	$\boldsymbol{\epsilon}_{\mathrm{JKL}}\mathbf{F}^{\mathrm{p}}_{\mathrm{iL,K}}$
Δ_{n}	normal separation
Δ_{t}	effective sliding displacement
Δ_{t1}, Δ_{t2}	sliding displacements
$\Delta_{\mathrm{n}}^{max}$, $\Delta_{\mathrm{t}}^{max}$	max normal and tangential separations reached during loading / unloading
$\Delta\sigma$	strengthening increment
δ_{n}, δ_{t}	normal and tangential final crack opening widths
δ_{nc}, δ_{tc}	normal and tangential critical opening displacements at which T_{n} and T_{t} equal $\sigma_{\max}$ and $\tau_{\max}$, respectively
$\bar{\delta}_{\mathrm{n}}$, $\bar{\delta}_{\mathrm{t}}$	normal and tangential conjugate final crack opening widths
ε_{N}	mean nucleation strain
ε_p	plastic strain
λ	elastic constant
ξ, η	natural coordinate system axes
η	elastic constant
λ_{n}, λ_{t}	initial slope indicators
μ	elastic constant
ν	Poisson's ratio
ρ	dislocation density
σ_e	effective Mises stress
σ_k^k	3 × (macroscopic mean stress)
σ_M	yield stress of fully dense matrix
σ_n	normal stress
τ	resolved shear stress
$\sigma_{\max}$, $\tau_{\max}$	normal and tangential cohesive strengths
ϕ_{n}, ϕ_{t}	fracture energies
Ψ	PPR model's potential function
$\langle\cdot\rangle$	Macaulay Bracket $\langle x\rangle = \begin{cases} 0, & x < 0 \\ x, & x \geq 0 \end{cases}$

PREFACE

Chapter 1

Implementation and Verification of the Park-Paulino-Roesler Cohesive Zone Model in 3D

Albert Cerrone, Paul Wawrzynek, Aida Nonn, Glaucio Paulino, Anthony Ingraffea

published in Engineering Fracture Mechanics

DOI: http://dx.doi .org/10.1016/j.engfracmech.2014.03.010

Chapter 2

A Use Case for Digital Twin

Albert Cerrone, Jacob Hocchhalter, Gerd Heber, Anthony Ingraffea

submitted to International Journal of Aerospace Engineering

Chapter 3

Digital Twin at the Microscale: Implementation and Verification of a Microstructure-Based Capability for Modeling Microcrack Nucleation in LSHR at Room Temperature

Albert Cerrone, Clayton Stein, Reeju Pokharel, Christopher Hefferan, Jonathan Lind, Harris Tucker, Robert Suter, Anthony Rollett, Anthony Ingraffea

submitted to Modeling and Simulation in Materials Science and Engineering

CHAPTER 1

IMPLEMENTATION AND VERIFICATION OF THE PARK-PAULINO-ROESLER COHESIVE ZONE MODEL IN 3D

Cohesive zone models (CZMs) date back to Dugdale's foundational strip yield model from the 1960s. Since then, hundreds of CZMs have been proposed in the literature, and in general, they have grown in sophistication to the present day. However, until very recently, no model existed which characterized different fracture energies and cohesive strengths in each fracture mode, provided for several material failure behaviors, and demonstrated a monotonic change of the work-of-separation for both proportional and non-proportional paths of separation. In other words, no CZM was capable of modeling accurately highly mixed-mode failure processes such as intergranular fracture. Enter the Park-Paulino-Roesler (PPR) potential-based model, a cohesive constitutive model formulated to be thermodynamically consistent under a high degree of mode-mixity. It was published in 2009 and verified against two-dimensional applications. Herein, the PPR's generalization to three-dimensions is detailed, its implementation in a finite element framework is discussed, and its use in single-core and high performance computing (HPC) applications is demonstrated.

The PPR model is shown to be applicable at both the macro- and micro-scales. This is a clear advantage over continuum plasticity damage models which are not relevant at the microscale and sometimes lack enough fidelity to model fracture accurately at the macroscale— limitations discussed in Chapter 2 of this dissertation. Specifically, the PPR is used to model the degradation of adhesive in a T-peel (Mode I) specimen. Additionally, it is leveraged to model fracture in a mixed-mode bending (Modes I and II) specimen. It is also used to model delamination between plies in a composite in an edge crack torsion (Modes II and III) test. Moreover, it is used to model fracture

propagation in linepipe steel under dynamic loading conditions. Finally, coupled with the crystal-plastic finite-element method, it is shown to model effectively intergranular fracture in polycrystals. Consequently, the PPR model could be coupled with the microstructure-based framework detailed in Chapter 3 to model propagation along grain boundaries.

1.1 Introduction and Motivation

Cohesive zone modeling of fracture processes dates to Dugdale's strip yield model [1]. In this model, yield magnitude closure stresses are applied between the actual crack tip and a notional crack tip, the length of the total plastic zone, to circumvent the unrealistic prediction of infinite stresses at the crack tip. Barenblatt [2] placed material-specific stresses according to a prescribed distribution in the aforementioned zone, leading to the many cohesive zone models (CZMs) available today. Applications of CZMs abound in the literature. Hillerborg *et al*. [3] were the first to model failure in a material by adapting a CZM into a finite element analysis. The cohesive finite element method (CFEM) has been used to conduct studies across a wide range of material systems: rock (e.g. Boone *et al*. [4]), ductile materials at the microscale (e.g. Needleman [5] and Iesulauro [6]), ductile materials at the macroscale (e.g. Tvergaard and Hutchinson [7] and Scheider and Brocks [8]), concrete (e.g. Ingraffea *et al*. [9]; Elices *et al*. [10]; Park *et al*. [11]), bone (e.g. Tomar [12] and Ural and Vashishth [13]), functionally graded materials (Zhang and Paulino [14]), and asphalt pavements (Song *et al*. [15]). Hui et al. [16] and Park and Paulino [17] have presented a review of the literature in the field and thus the reader is referred to these articles and the references therein.

The fracture behavior in potential-based cohesive zone models is characterized by a potential function, from which traction-separation behavior proceeds. Taking the first derivative of this potential function with respect to the displacement separation results in the cohesive tractions. The second derivative, in turn, provides the material tangent modulus. A cursory search of potential-based cohesive zone models in the literature will undoubtedly return hundreds of models. Needleman's potential from 1987 [5], often cited in the literature, describes the normal, Mode I, interaction with a polynomial potential; however, it is limited because it only considers decohesion by normal separation. Tvergaard extended Needleman's potential to better account for mode-

mixity with the use of an interaction formula defining an effective displacement [18]. Needleman later developed a potential accounting for debonding by tangential separation [19] whereby the normal and tangential interactions are described by exponential and periodic functions, respectively. Alternatively, Xu and Needleman developed a potential where the normal and tangential separations are both described by exponential functions [20].

Park *et al*. published a unified potential-based CZM, the PPR (Park-Paulino-Roesler) CZM [21], that addresses the shortcomings of the prevailing potential-based CZMs in the literature, particularly with respect to mode-mixity, user flexibility, and consistency. First, it characterizes different fracture energies and cohesive strengths in each fracture mode, an accommodation not made by most CZMs. Moreover, it provides for several material failure behaviors by allowing the modeler to define the shape of the softening curve in both the normal and shear traction-separation relations; in most CZMs, softening behavior is hard-coded and cannot be changed. Finally, and perhaps most important, it is consistent in anisotropic fracture energy conditions; it demonstrates a monotonic change of the work-of-separation for both proportional and non-proportional paths of separation, a quality not seen in most CZMs.

This paper describes the generalization of the PPR model to three dimensions, details its implementation in a finite element framework, and presents its use in single-core and high performance computing (HPC) applications. We identify a variety of examples which assess the various features of the PPR model considering different loading conditions (e.g. quasi-static and dynamic), mode-mixity, bulk material behavior, and interfacial behavior (investigating the parameter space that defines the traction-separation relationship). The examples include a mode I T-peel specimen, a mixed-mode (I and II) bending specimen, an edge crack torsion (ECT) specimen (modes II and

III), the Battelle Drop-Weight Tear (BDWT) test, and intergranular fracture (grain-boundary decohesion) at the microstructural scale.

1.2 Implementation

A description of the PPR's implementation and verification in two-dimensions can be found in Park *et al*. [21]. The generalization of the intrinsic PPR model to three-dimensions is discussed here.

1.2.1 Brief Overview

Figure 1.1 gives an overview of the cohesive interactions of the PPR model. The normal cohesive interaction region is rectangular and bounded by δ_n and $\bar{\delta}_t$. Complete cohesive normal failure occurs when the normal separation, Δ_n, reaches the normal final crack opening width, δ_n, or the effective sliding displacement, Δ_t, reaches the tangential conjugate final crack opening width, $\bar{\delta}_t$. The tangential cohesive interaction, in turn, is rectangular and bounded by δ_t and $\bar{\delta}_n$. Complete cohesive tangential failure occurs when the effective sliding displacement reaches the tangential final crack opening width, δ_t, or normal separation reaches the normal conjugate final crack opening width, $\bar{\delta}_n$.

The shape parameters α and β control the normal and tangential softening curve shapes. A shape parameter less than 2 causes plateau-type behavior, whereas a shape parameter greater than 2 yields behavior indicative of quasi-brittle materials. When Δ_n reaches the critical opening displacement, δ_{nc}, the normal cohesive traction is at its maximum, σ_{max} (the normal cohesive strength). When the sliding displacement reaches the critical sliding displacement, δ_{tc}, the effective tangential traction is at its maximum, τ_{max} (the tangential cohesive strength). The area under the normal cohesive interaction for $\Delta_t = 0$ corresponds to the normal fracture energy, ϕ_n, while the area under the tangential cohesive interaction for $\Delta_n = 0$ corresponds to the tangential fracture energy, ϕ_t.

The three cohesive tractions T_n, T_{t1}, and T_{t2} are dependent upon the normal separation, Δ_n, and two sliding displacements, Δ_{t1} and Δ_{t2}. Figure 1.2 illustrates these displacements. The effective sliding displacement, Δ_t , is given by

$$\Delta_t = \sqrt{(\Delta_{t1})^2 + (\Delta_{t2})^2} \quad . \tag{1.1}$$

The tangential cohesive tractions, T_{t1} and T_{t2}, relate to Δ_t as follows:

$$T_{t1}(\Delta_n, \Delta_t, \Delta_{t1}) = \frac{\Delta_{t1}}{\Delta_t} T_t(\Delta_n, \Delta_t) \tag{1.2}$$

$$T_{t2}(\Delta_n, \Delta_t, \Delta_{t2}) = \frac{\Delta_{t2}}{\Delta_t} T_t(\Delta_n, \Delta_t)$$

where T_t is an effective tangential traction formulated in the next section.

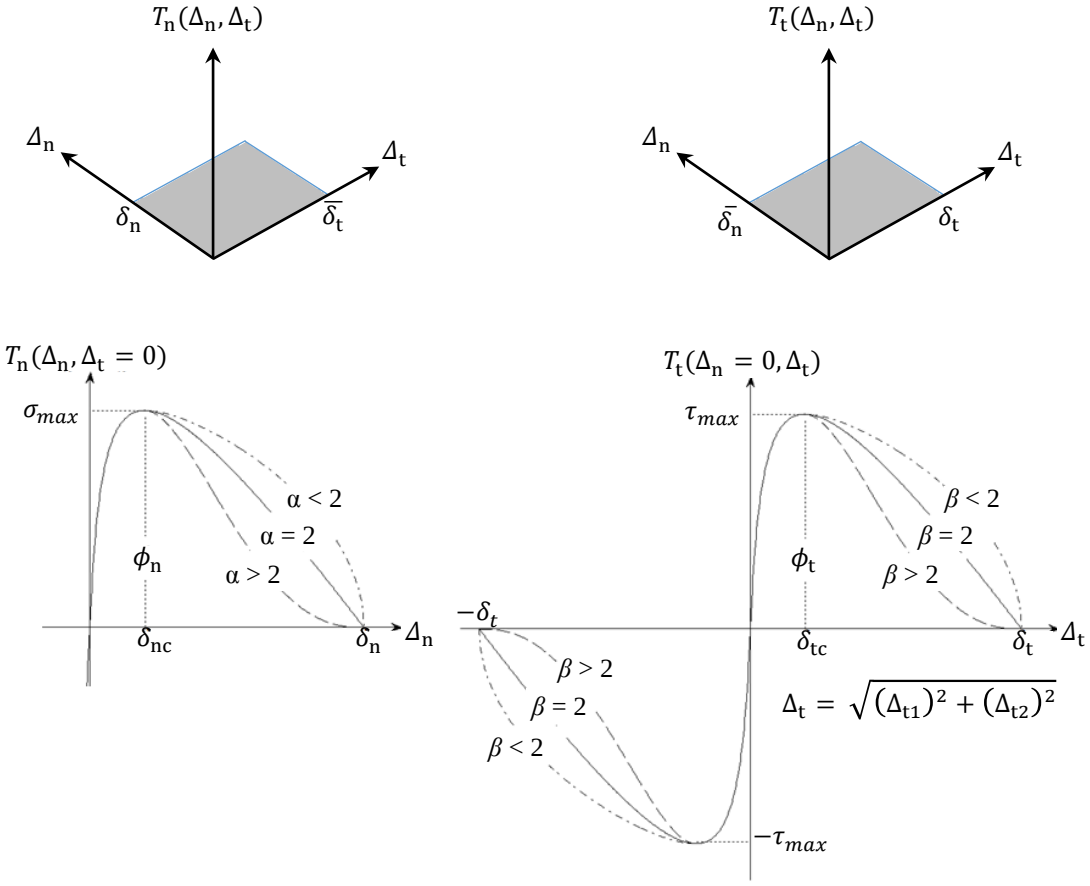

Figure 1.1: Traction-separation relation of the PPR model.

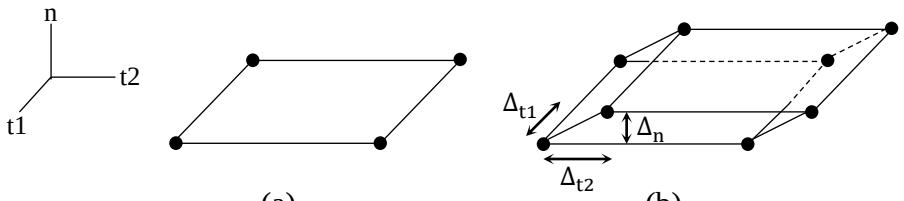

Figure 1.2: Cohesive element collapsed (a) and deformed (b) with separations demarcated.

1.2.2 Expressions for the Cohesive Tractions

The PPR model is a function of four basic independent parameters in the normal and shearing fracture modes, namely cohesive strength, fracture energy, shape of softening curve, and initial slope of the traction-separation relationship. The potential, Ψ, is given by:

$$\Psi(\Delta_{\mathrm{n}}, \Delta_{\mathrm{t1}}, \Delta_{\mathrm{t2}}) = min(\phi_{\mathrm{n}}, \phi_{\mathrm{t}}) + \left[\Gamma_{\mathrm{n}}\left(1-\frac{\Delta_{\mathrm{n}}}{\delta_{\mathrm{n}}}\right)^{\alpha}\left(\frac{m}{\alpha}+\frac{\Delta_{\mathrm{n}}}{\delta_{\mathrm{n}}}\right)^{m}+\langle\phi_{\mathrm{n}}-\phi_{\mathrm{t}}\rangle\right] \tag{1.3}$$
$$\times\left[\Gamma_{\mathrm{t}}\left(1-\frac{\sqrt{(\Delta_{\mathrm{t1}})^2+(\Delta_{\mathrm{t2}})^2}}{\delta_{\mathrm{t}}}\right)^{\beta}\left(\frac{n}{\beta}+\frac{\sqrt{(\Delta_{\mathrm{t1}})^2+(\Delta_{\mathrm{t2}})^2}}{\delta_{\mathrm{t}}}\right)^{n}+\langle\phi_{\mathrm{t}}-\phi_{\mathrm{n}}\rangle\right]$$

As a matter of notation, the energy constants are Γ_{n} and Γ_{t}; the fracture energies are ϕ_{n} and ϕ_{t}; the non-dimensional exponents are m and n; the shape parameters are α and β; the final crack opening widths are δ_{n} and δ_{t}; the normal cohesive separation is Δ_{n}; and the effective sliding displacement is Δ_{t}. Note that $\langle\cdot\rangle$ is the Macaulay bracket, where $\langle x\rangle = \begin{cases}0, & x<0\\ x, & x\geq 0\end{cases}$.

The energy constants Γ_{n} and Γ_{t} are given by:

$$\Gamma_{\mathrm{n}} = \begin{cases}\left(\frac{\alpha}{m}\right)^{m}, & \phi_{\mathrm{n}} < \phi_{\mathrm{t}}\\ -\phi_{\mathrm{n}}\left(\frac{\alpha}{m}\right)^{m}, & \phi_{\mathrm{n}} \geq \phi_{\mathrm{t}}\end{cases} \tag{1.4}$$

$$\Gamma_{\mathrm{t}} = \begin{cases}\left(\frac{\beta}{n}\right)^{n}, & \phi_{\mathrm{t}} \leq \phi_{\mathrm{n}}\\ (-\phi_{\mathrm{t}})\left(\frac{\beta}{n}\right)^{n}, & \phi_{\mathrm{t}} > \phi_{\mathrm{n}}\end{cases}$$

The non-dimensional exponents m and n are functions of the shape parameters and initial slope indicators, λ_n and λ_t, as:

$$m = \frac{\alpha(\alpha-1)\lambda_n^2}{1-\alpha\lambda_n^2} \quad , \quad n = \frac{\beta(\beta-1)\lambda_t^2}{1-\beta\lambda_t^2} \tag{1.5}$$

$$\lambda_n = \frac{\delta_{nc}}{\delta_n} \quad , \quad \lambda_t = \frac{\delta_{tc}}{\delta_t} \tag{1.6}$$

The initial slope indicators are measures of cohesive stiffness and control cohesive elastic behavior. Smaller initial slope indicators cause higher cohesive stiffness, which in turn decrease artificial elastic deformation. They are functions of δ_{nc} and δ_{tc}, the normal and tangential critical crack opening widths, respectively, corresponding to maximum normal and tangential cohesive strength, and δ_n and δ_t, the normal and tangential final crack opening widths, respectively, given by the expressions:

$$\delta_n = \frac{\phi_n}{\sigma_{max}}\alpha\lambda_n(1-\lambda_n)^{\alpha-1}\left(\frac{\alpha}{m}+1\right)\left(\frac{\alpha}{m}\lambda_n+1\right)^{m-1} \tag{1.7}$$

$$\delta_t = \frac{\phi_t}{\tau_{max}}\beta\lambda_t(1-\lambda_t)^{\beta-1}\left(\frac{\beta}{n}+1\right)\left(\frac{\beta}{n}\lambda_t+1\right)^{n-1}$$

Taking the gradient of the potential Ψ yields the normal and effective tangential cohesive tractions T_n and T_t, respectively. They are given below:

$$T_n(\Delta_n,\Delta_t) = \frac{\Gamma_n}{\delta_n}\left[m\left(1-\frac{\Delta_n}{\delta_n}\right)^{\alpha}\left(\frac{m}{\alpha}+\frac{\Delta_n}{\delta_n}\right)^{m-1} - \alpha\left(1-\frac{\Delta_n}{\delta_n}\right)^{\alpha-1}\left(\frac{m}{\alpha}+\frac{\Delta_n}{\delta_n}\right)^{m}\right]$$
$$\times \left[\Gamma_t\left(1-\frac{|\Delta_t|}{\delta_t}\right)^{\beta}\left(\frac{n}{\beta}+\frac{|\Delta_t|}{\delta_t}\right)^{n} + \langle\phi_t-\phi_n\rangle\right] \tag{1.8}$$

$$T_t(\Delta_n,\Delta_t) = \frac{\Gamma_t}{\delta_t}\left[n\left(1-\frac{|\Delta_t|}{\delta_t}\right)^{\beta}\left(\frac{n}{\beta}+\frac{|\Delta_t|}{\delta_t}\right)^{n-1} - \beta\left(1-\frac{|\Delta_t|}{\delta_t}\right)^{\beta-1}\left(\frac{n}{\beta}+\frac{|\Delta_t|}{\delta_t}\right)^{n}\right]$$
$$\times\left[\Gamma_n\left(1-\frac{\Delta_n}{\delta_n}\right)^{\alpha}\left(\frac{m}{\alpha}+\frac{\Delta_n}{\delta_n}\right)^{m} + \langle\phi_n-\phi_t\rangle\right]\frac{\Delta_t}{|\Delta_t|}$$

The shear tractions, T_{t1} and T_{t2}, are subsequently determined from (2). The normal, shear, and effective shear tractions are plotted in Figure 1.3 for $\phi_t > \phi_n$, quasi-brittle behavior for mode I, and plateau-type behavior for modes II and III.

1.2.3 Implementation in FE Frameworks

For details regarding the formulation of the material tangent stiffness matrix, **D,** and provisions for unloading/reloading and contact, refer to Appendix I. Of particular interest:

- The traction-separation relation for the 3D implementation is defined by ϕ_n, ϕ_t, λ_n, λ_t, σ_{max}, τ_{max}, α, and β, the same as the 2D implementation.
- Resistance to sliding in the two shearing directions is equal— T_{t1} and T_{t2} are not scaled to yield anisotropic sliding behavior, but could theoretically be altered to do so.

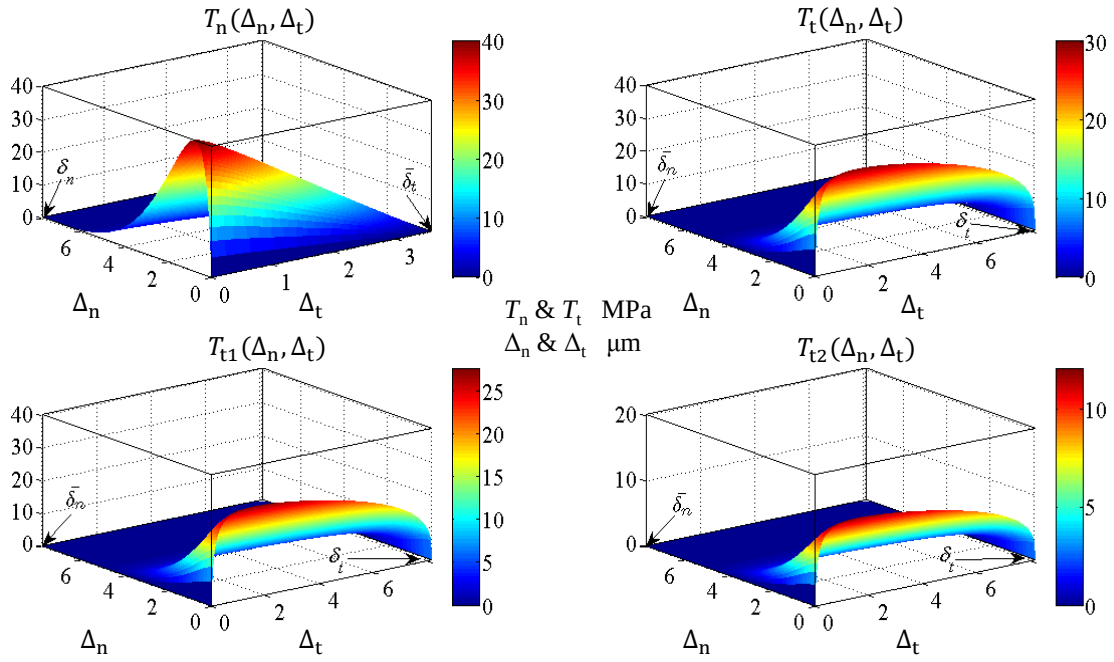

Figure 1.3: Cohesive tractions with $\phi_n = 100$ N/m, $\phi_t = 200$ N/m, $\sigma_{max} = 40$ MPa, $\tau_{max} = 30$ MPa, $\alpha = 5$, $\beta = 1.3$, $\lambda_n = 0.1$, and $\lambda_t = 0.2$. It is assumed that $\Delta_{t2} = 0.4\Delta_t$, where $\Delta_{t1} = \sqrt{\Delta_t^2 - \Delta_{t2}^2}$.

- The normal conjugate final crack opening width is determined by solving the nonlinear equation:

$$T_{\mathrm{n}}\left(\Delta_{\mathrm{n}}=0,\Delta_{\mathrm{t}}=\bar{\delta}_{\mathrm{t}}\right)=0=\frac{\Gamma_{\mathrm{n}}}{\delta_{\mathrm{n}}}\left[m\left(\frac{m}{\alpha}\right)^{m-1}-\alpha\left(\frac{m}{\alpha}\right)^{m}\right]\left[\Gamma_{\mathrm{t}}\left(1-\frac{|\Delta_{\mathrm{t}}|}{\delta_{\mathrm{t}}}\right)^{\beta}\left(\frac{n}{\beta}+\frac{|\Delta_{\mathrm{t}}|}{\delta_{\mathrm{t}}}\right)^{n}+\langle\phi_{\mathrm{t}}-\phi_{\mathrm{n}}\rangle\right], \quad (1.9)$$

while the tangential conjugate final crack opening width follows in the same manner from:

$$T_{\mathrm{t}}\left(\Delta_{\mathrm{n}}=\bar{\delta}_{\mathrm{n}},\Delta_{\mathrm{t}}=0\right)=0=\frac{\Gamma_{\mathrm{t}}}{\delta_{\mathrm{t}}}\left[n\left(\frac{n}{\beta}\right)^{n-1}-\beta\left(\frac{n}{\beta}\right)^{n}\right]\left[\Gamma_{\mathrm{n}}\left(1-\frac{\Delta_{\mathrm{n}}}{\delta_{\mathrm{n}}}\right)^{\alpha}\left(\frac{m}{\alpha}+\frac{\Delta_{\mathrm{n}}}{\delta_{\mathrm{n}}}\right)^{m}+\langle\phi_{\mathrm{n}}-\phi_{\mathrm{t}}\rangle\right]. \quad (1.10)$$

- The PPR model is implemented in Abaqus as an 8-noded UEL with four integration points in the natural coordinate system over the domain $-1 \leq \xi \geq 1$ and $-1 \leq \eta \geq 1$:

  $\xi = -0.707 \quad \eta = -0.707$

  $\xi = \ \ 0.707 \quad \eta = -0.707$

  $\xi = \ \ 0.707 \quad \eta = \ \ 0.707$

  $\xi = -0.707 \quad \eta = \ \ 0.707$

  The isoparametric formulation is given in Figure 1.4 where **K** is the element stiffness matrix, **f** the internal force vector, **B** the strain-displacement matrix, and |**J**| the determinant of the Jacobian. The source code of the UEL is included in Appendix II.

- The initial thickness of a cohesive element is simply the distance in the normal direction between nodes belonging to the same nodal pair. For zero-thickness cohesive elements, the two nodes forming a pair are initially collapsed upon one another. For cohesive elements with an initial thickness, this thickness is not

included in the measure for Δ_n as cohesive normal separation is a relative measure.

- Finite Element All-Wheel Drive (FEAWD) [22] is employed for HPC applications. FEAWD is an "in-house" high performance research finite element code developed at Cornell University. It is built on MPI, FemLib, PETSc [23–25], ParMETIS, and HDF5.

$$\begin{aligned} \mathrm{N1} &= \frac{1}{4}(1-\varepsilon)(1-\eta) \\ \mathrm{N2} &= \frac{1}{4}(1+\varepsilon)(1-\eta) \\ \mathrm{N3} &= \frac{1}{4}(1+\varepsilon)(1+\eta) \\ \mathrm{N4} &= \frac{1}{4}(1-\varepsilon)(1+\eta) \end{aligned} \quad (1.11)$$

$$\boldsymbol{K} = \int_{-1}^{1}\int_{-1}^{1} \boldsymbol{B}^{\mathrm{T}}\boldsymbol{D}\boldsymbol{B}|\boldsymbol{J}|\,\mathrm{d}\xi\,\mathrm{d}\eta \quad (1.12)$$

$$\boldsymbol{f} = \int_{-1}^{1}\int_{-1}^{1} \boldsymbol{B}^{\mathrm{T}}\boldsymbol{t}|\boldsymbol{J}|\,\mathrm{d}\xi\,\mathrm{d}\eta \quad (1.13)$$

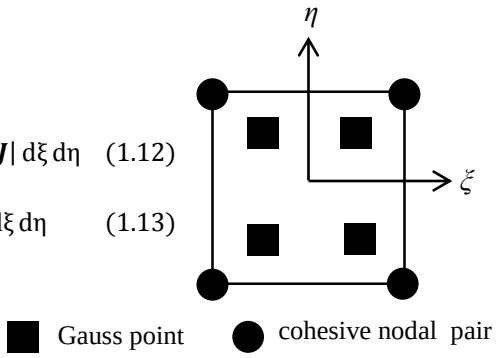

Figure 1.4: Isoparametric formulation of 8-noded cohesive elements.

1.3 Application Case Studies

1.3.1 Mode I: T-Peel Specimen

Debonding is investigated in aluminum / epoxy T-peel joints. Mechanical tests performed by Alfano *et al*. [26] and Alfano [27] using the T-peel joint specimen, Figure 1.5(a), investigated bond strengths for grit blasted specimens. The experiment is simulated here in both 2D (plane stress) and 3D using the PPR model.

The bulk material, AA6085-T6, was modeled with a Mises plasticity model. The yield stress and plastic modulus were 250 MPa and 525.8 MPa, respectively. It was assigned a linear elastic, isotropic material model with E = 68 GPa and ν = 0.33. The epoxy, Loctite Hysol 9466, was modeled with the PPR and was represented by a single layer of cohesive elements with an initial thickness of 0.25 mm. A maximum acceptable cohesive zone length was determined from the plastic zone size estimates discussed in Rice [28]. Both 2D and 3D models were loaded in displacement-control. The 2D mesh was composed of 4-noded bilinear elements with reduced integration and hourglass

control (CPS4R) and four-noded, quadrilateral PPR UELs. The 3D mesh was composed of 8-noded linear bricks with reduced integration and hourglass control (C3D8R) and eight-noded PPR UELs of length 0.450 mm.

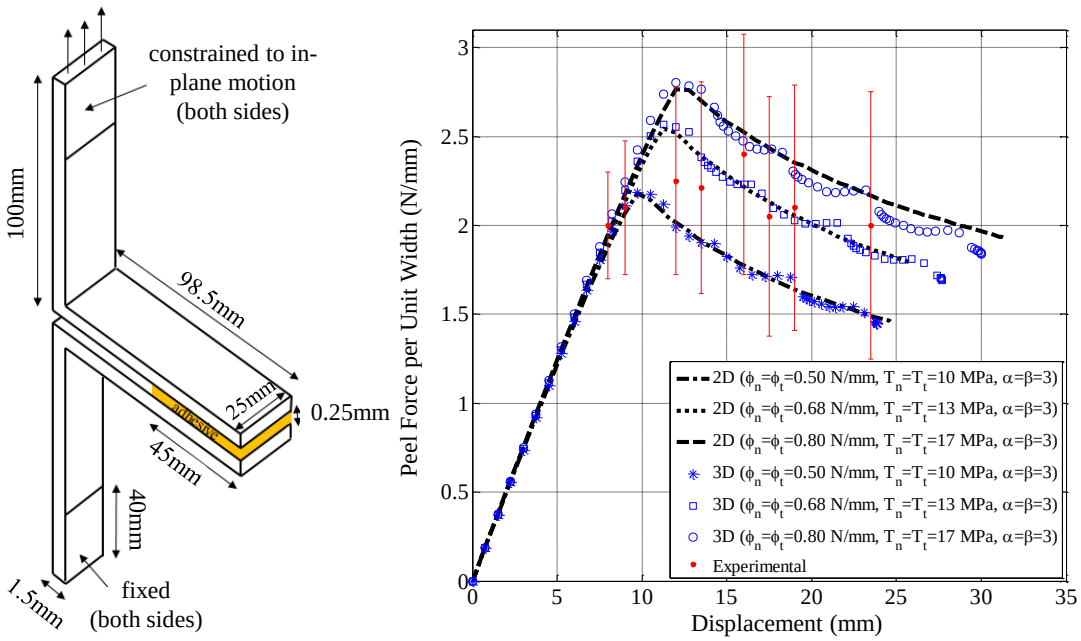

Figure 1.5: T-Peel Joint Specimen (a) and comparison between experimental data and numerical simulations (b).

A comparison of the experimental results and the numerical simulations is given in Figure 1.5(b). It is apparent that the 2D and 3D simulations qualitatively reproduce the experimental data within the error bounds. For the 2D simulations, the curves in Figure 1.5(b) do not exhibit the fluctuations in post-peak strength which the 3D simulations and experimental results reflect.

Given that the adhesive is a ductile material, it would seem that relatively low shape parameters, α and β, would replicate more accurately experimental behavior; however, as Figure 1.6 suggests, the 3D solution shows no sensitivity to softening behavior.

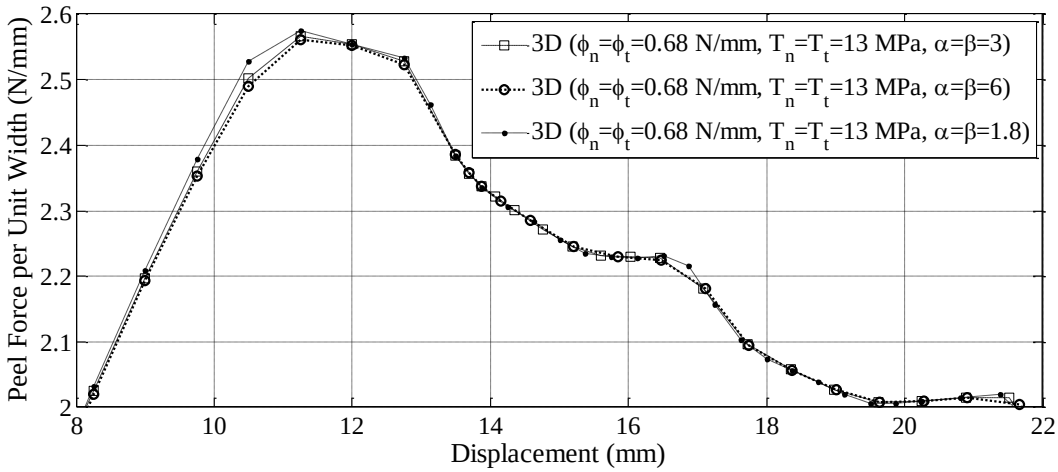

Figure 1.6: Comparison of 3D numerical simulations with varying softening behaviors.

1.3.2 Modes I and II: Mixed-Mode Bending (MMB) Specimen

The MMB specimen is detailed in ASTM standard D 6671/D 6671M [29]. The MMB test [30], a combination of the double cantilever beam and end-notch flexure tests, was developed by Reeder and Crews and is used widely to investigate mixed-mode fracture in composites, Figure 1.7.

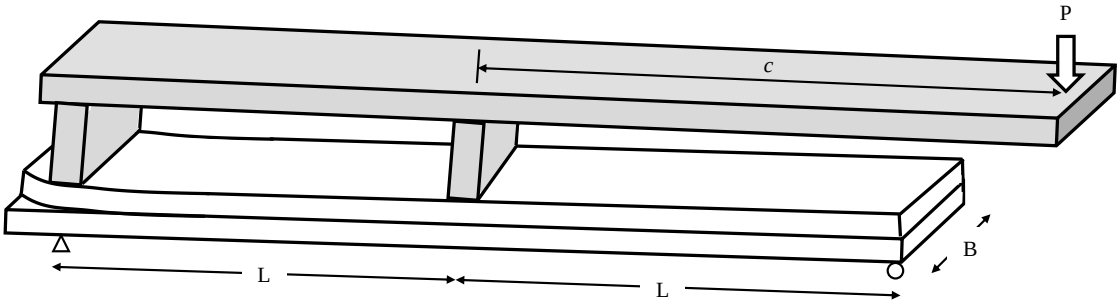

Figure 1.7: MMB specimen with rigid lever. A load P is applied to a rigid lever a distance *c* from the specimen's midspan. L = 51.0 mm, B=25.4 mm, and c = 60 mm for geometry modelled.

Numerical simulations with the PPR model replicating the MMB test were conducted in 2D by Park *et al*. [21], and the numerical results were compared against the analytical solution given by Mi *et al*. [31]. The simulations are extended here to 3D using Abaqus. A modified Riks method was employed to capture the negative stiffness of the load-displacement response. The zero-thickness cohesive elements were

extended along the beam's midplane, just beyond the initial delamination. The mesh was composed of 0.398 mm-length 8-noded PPR UELs and 8-noded linear bricks with reduced integration and hourglass control (C3D8R). The specimen was assigned a linear elastic, isotropic material model with E = 122 GPa and ν = 0.25. Informed by Park *et al*. [21], the initial slope indicators λ_n and λ_t were assigned values 0.005 and 0.025, respectively, while the shape parameters α and β were both assigned a value of 3. Normal and tangential cohesive strengths, σ_{max} and τ_{max}, were both set to 10 MPa and the normal and tangential fracture energies, ϕ_n and ϕ_t, were 0.5 N/mm.

A comparison of the analytical solution and numerical simulation is given in Figure 1.8. Here, the simulation results converge to the analytical.

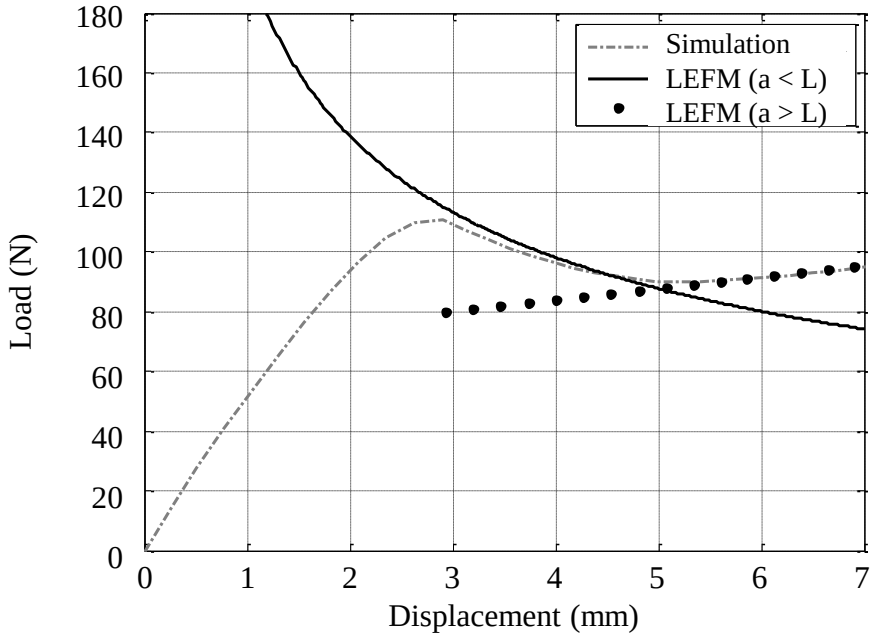

Figure 1.8: Plot of Load (P) versus crack opening displacement measured below hinge connection. Analytical solution overlaid.

1.3.3 Modes II and III: Edge Crack Torsion (ECT) Specimen

The edge crack torsion (ECT) specimen is used to characterize mode III delamination fracture in laminated composites. Considering Ratcliffe's modified ECT specimen [32], Figure 1.9, the rectangular specimen has an edge delamination at the mid-plane. Two

pins impart load to the specimen in a symmetric fashion causing Mode III shear sliding at the mid-plane. Mode II develops at the edges of the specimen. Ratcliffe's modified ECT specimen is considered here for verification of the three-dimensional PPR model under mixed-mode loading.

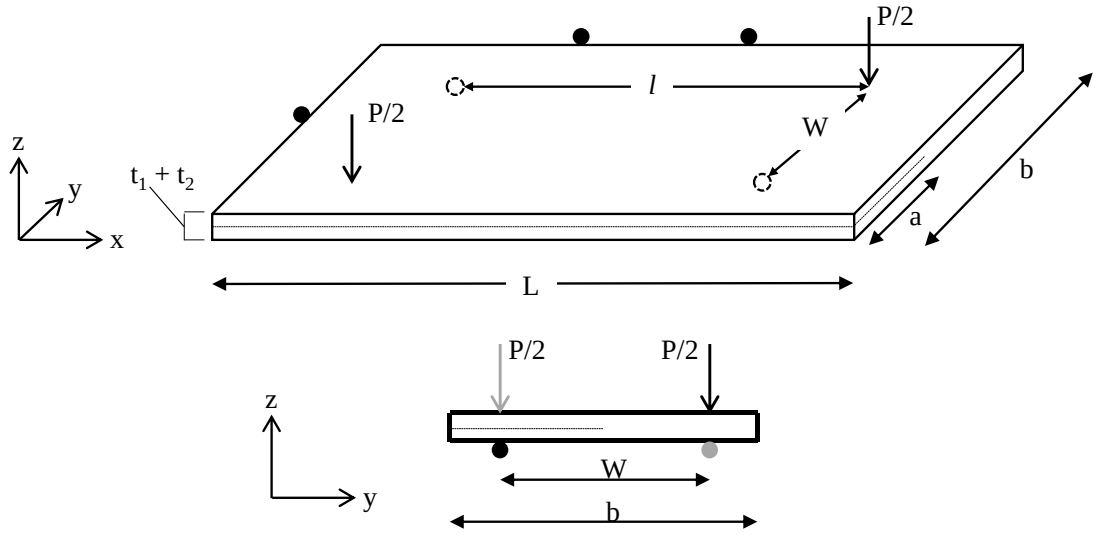

Figure 1.9: Modified ECT Specimen. L = 108 mm, *l* = 76 mm, b = 38 mm, W = 32 mm, $t_1 = t_2 = 3.75$ mm, a = variable. The circles represent roller supports.

The material is S2/8552, a glass-epoxy prepreg, with properties given in Table 1.1 [33]. The stacking sequence was $[90/0/(+45/-45)_7/(-45/+45)_7/0/90]_s$, with each ply modeled as a single, orthotropic layer. The specimen was modeled in Abaqus with 8-noded linear bricks with reduced integration and hourglass control (C3D8R) and 8-noded PPR UELs ranging in length from 0.210 mm to 1.0 mm. The two crack surfaces were assigned frictionless tangential contact controls, and to prevent interpenetration, augmented Lagrangian contact controls were assigned. The specimen was loaded on the top surface via two node-based kinematic boundary conditions in the z-direction. Roller supports were positioned on the bottom, min-x, and max-y surfaces, per Figure 1.9.

Table 1.1: S2/8552 Material Properties.

Property	Value
E_{11}	47.71 GPa
E_{22}, E_{33}	12.27 GPa
ν_{12}, ν_{13}	0.278
ν_{23}	0.403
G_{12}, G_{13}	4.83 GPa
G_{23}	4.48 GPa

A visualization of the deformed configuration and a load-displacement plot with simulation and Ratcliffe's experimental results [32] are given in Figure 1.10 and Figure 1.11, respectively. Two initial crack lengths, 15.2 mm and 19.0 mm, were investigated. From a calibration study on the a = 19.0 mm configuration, each cohesive element at the midplane was assigned parameters $\phi_n = 1.5$ N/mm, $\phi_t = 4.7$ N/mm, $\sigma_{max} = \tau_{max} = 58$ MPa, $\lambda_n = \lambda_t = 0.002$, and $\alpha = \beta = 6$. For the uncalibrated a = 15.2 mm configuration, the numerical simulation's peak load was approximately 4,560 N at displacement 3.9 mm, 180 N higher than the experimental peak at displacement 3.6 mm. It is apparent that the PPR-based simulations can reproduce observed Mode II/III behavior within a reasonable tolerance.

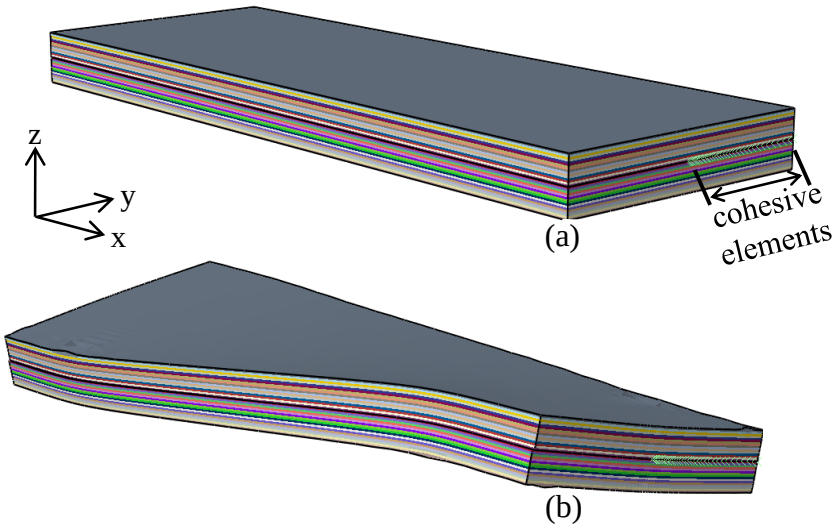

Figure 1.10: Undeformed (a) and deformed (b) configurations of ECT numerical model. Colors denote plies.

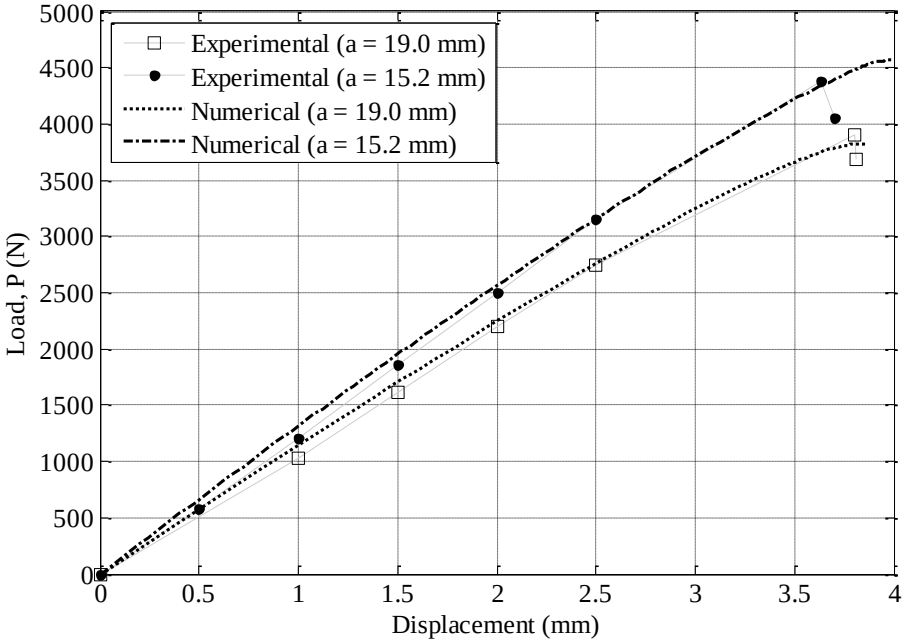

Figure 1.11: Numerical and experimental load-displacement curves for ECT test.

1.3.4 Dynamic Analysis: Battelle Drop-Weight Tear Test

The Battelle Drop-Weight Tear (BDWT) test is used commonly in the steel pipeline industry to determine transition temperature based on evaluated fracture surface appearance. Recent investigations in Igi *et al*. [34] and Nonn and Kalwa [35] are focused on the study of this test to determine the crack propagation characteristics of long-running ductile cracks, specifically the crack arrest capabilities of the underlying material. Associated standards are given in the following references [36–38]. A schematic of the apparatus showing hammer, supports, and test specimen is given in Figure 1.12(a). This test was conducted with drop energy of 105 kJ resulting from a hammer weight of 2.8 tonnes and falling height of 3.8m. The test specimen was a rectangular bar with dimensions of 76 mm height, 305 mm length, and a thickness corresponding to the thickness of linepipe, here 18.4 mm. The full thickness specimen extracted circumferentially from the pipe contained a 5 mm pressed notch to increase the probability of cleavage fracture initiation at the root of the notch. When the

specimen was impacted in three-point bending, a crack nucleated at the root of the pressed notch and propagated upwards towards the hammer. The test was conducted at room temperature and instrumented to register force vs. time curves, which allow for the determination of specific crack initiation and propagation energies. In addition, shear area fractions were evaluated from the appearance of the fracture surface without considering a length equal to the pipe thickness at each end. This is due to the fact that the material below the notch and at the back end of the specimen experiences work hardening during the indentation of the notch and by the impact of the hammer, respectively.

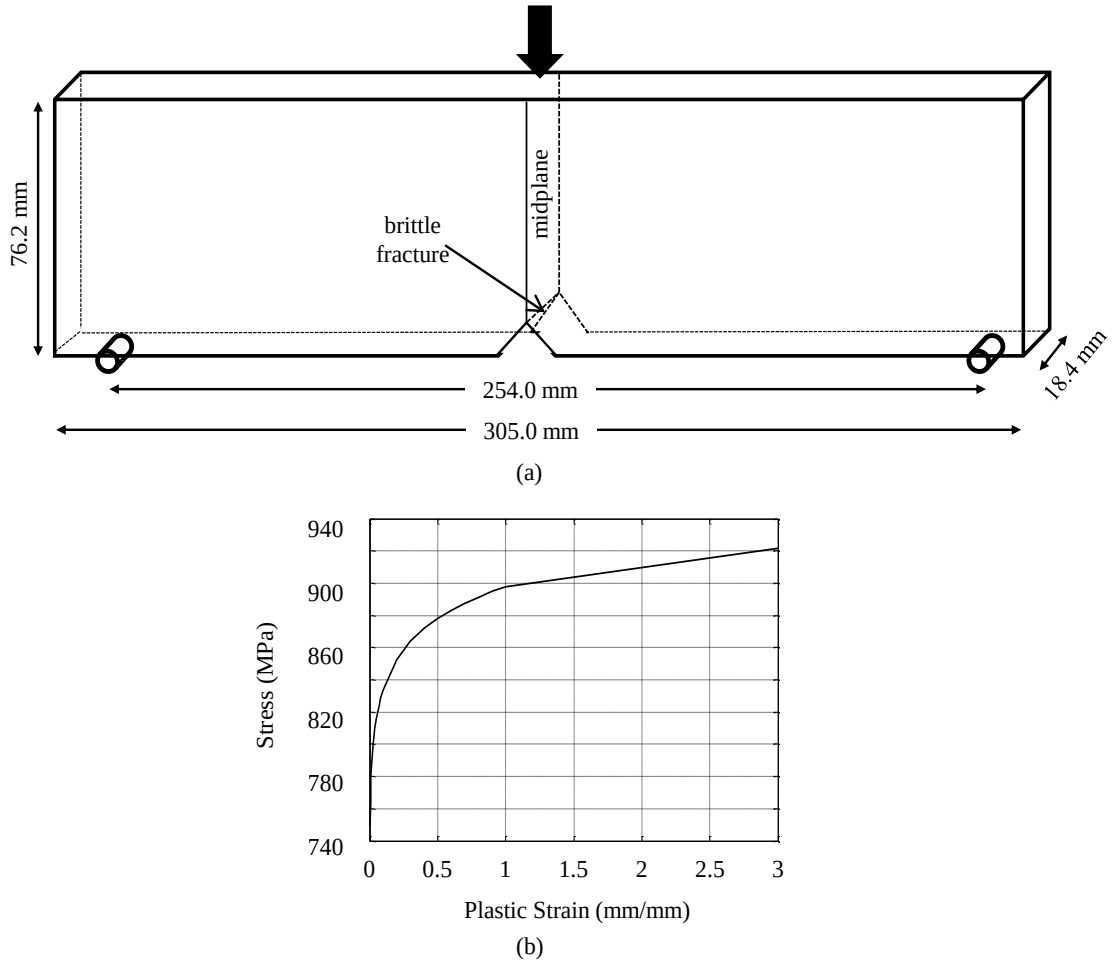

Figure 1.12: Battelle Drop-Weight Tear Test (BDWT) test specimen and simplified apparatus (a) and flow curve for rate sensitive Mises plasticity model (b).

The BDWT experimental results presented in Nonn and Kalwa [35] are used here to gauge the suitably of the PPR in describing the fracture behavior in X100 steel under dynamic loading. The analysis was dynamic with an implicit integration solution scheme. The finite element analyses were performed using Abaqus. By means of symmetry, only a fourth of the specimen was modeled. The support and hammer were modeled as analytical rigid bodies, the specimen with 8-noded linear bricks with reduced integration and hourglass control (C3D8R), and the crack path with 0.414 mm-length 8-noded PPR UELs. The X100 steel was modeled by a rate-sensitive Mises plasticity model with the flow curve given in Figure 1.12(b) and elastic properties E = 210 GPa and ν = 0.30. The flow curve was formulated from experimental data and is valid until the onset of uniform elongation; thereafter, the extension of the curve is represented by the power law function, $\sigma = K\epsilon_p^n$. Strength coefficient K = 897.8 MPa and strain hardening exponent n = 0.0321 were adjusted to the experimental stress-strain data. The strain rate dependence of the material was accounted for in the plasticity model by defining the yield strength values as a function of different strain rate levels.

The PPR model was employed to capture experimentally observed behavior. The parameters were estimated based on the literature recommendations in Negre *et al*. [39], Roy and Dodds [40], and Scheider *et al*. [41] (e.g. cohesive strength should lie in the range 2.0-3.0 x yield stress, ~700 MPa, and the fracture energy corresponds approximately to the J-integral value at initiation, 240 N/mm). Cohesive elements along the entire length of the midplane were assigned $\lambda_n = \lambda_t = 0.002$. Three sets of PPR parameters were considered in the present study. A visualization of the deformed configuration, PPR parameters, and a load-time plot with simulation and experimental results are given in Figure 1.13.

Two of the simulations employed PPR parameters indicative of X100, but considered different softening behaviors. The third used a substantially smaller

cohesive strength and higher fracture energy to better replicate post-peak behavior, particularly for time > 4 ms. Here, cohesive strength dictates the maximum load-bearing capacity of the beam while the fracture energy dictates to what extent this load can be carried— the higher the fracture energy, the longer the beam can sustain the hammer's impact.

Ductile softening behavior (i.e. plateau-type) most accurately captured peak, but did a relatively poor job capturing decay. Brittle softening, on the other hand, caused more rapid decay behavior while only underestimating the experimental peak by approximately 5%, (0.5ms before the experimental peak). Physically realistic PPR parameters (ϕ = 240 N/mm, σ = 2000 MPa, $\alpha = \beta = 6$) for X100 roughly replicated decay behavior, but underpredicted the decay for time > 4 ms. For the simulation with a relatively high fracture energy, the decay for time > 4 ms was more accurately characterized.

1.3.5 Intergranular Fracture

Intergranular fracture, commonly referred to as grain boundary decohesion, is a highly complex fracture phenomenon governed by many microstructural characteristics including grain size, shape, and orientation. One of the first studies investigating intergranular fracture was conducted in two-dimensions by Raj and Ashby [42]. With the advent of microstructure generation toolsets, robust surface and volumetric meshing routines, massively parallelized finite element drivers and accompanying HPC solutions, and the PPR model, it is now possible to model three-dimensional grain boundary decohesion and avoid numerical difficulties such as locking.

A polycrystal discretized along the grain boundaries with cohesive elements is an ideal medium by which to explain locking. Here, locking is defined as a numerical phenomenon marked by a nonlinear solver's inability to reach a converged solution because an insufficient number of load paths exist to accommodate additional

deformation. In a polycrystal, if a soft grain is pinned between stiffer grains, the cohesive elements surrounding the soft grain allow additional deformation insofar that they do not completely fail. If too many cohesive elements fail, the soft grain no longer has a release by which to unload accumulated deformation. Consequently, the model "locks" in place as the nonlinear solver is unable to reach a converged solution.

Iesulauro (2006) modeled grain boundary decohesion in synthetically generated microstructures with a three-dimensional adaptation of the Tvergaard and Hutchinson [7] coupled cohesive zone model. The model couples the normal and tangential tractions and displacements into coupled measures. Mode-mixity is considered through the interaction formula:

$$D = \sqrt{\left(\frac{\Delta_n}{\delta_n}\right)^2 + \left(\frac{\Delta_t}{\delta_t}\right)^2} \quad , \tag{1.14}$$

where the influence of normal and shear is proportional. When $D = 1$, the cohesive surface loses all ability to transmit traction.

Consider the scenario where a grain boundary is loaded normally so that it no longer has the capacity to transmit traction normally. If modeled with a coupled CZM, the interface has no capacity to transmit traction in either mode, a physically realistic behavior. If modeled with an uncoupled CZM without regard for energetically consistent boundary conditions, the interface will continue to transmit traction tangentially and yield physically unrealistic behavior. If modeled with the PPR, the interface will fail normally and still be able to transmit tangential tractions, as long as $\Delta_n < \bar{\delta}_n$. The PPR is preferred for this application not only because it replicates physically realistic behavior, but also, in the presence of mode-I, II, or III failure, preserves the cohesive interactions of the un-failed modes according to the final crack opening and conjugate final crack opening widths.

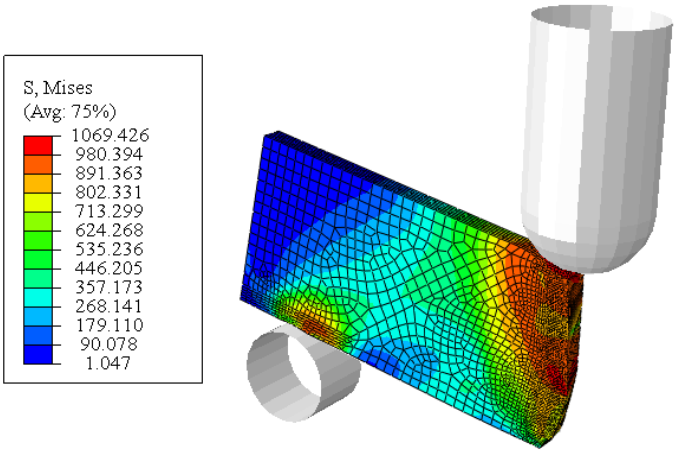

(a)

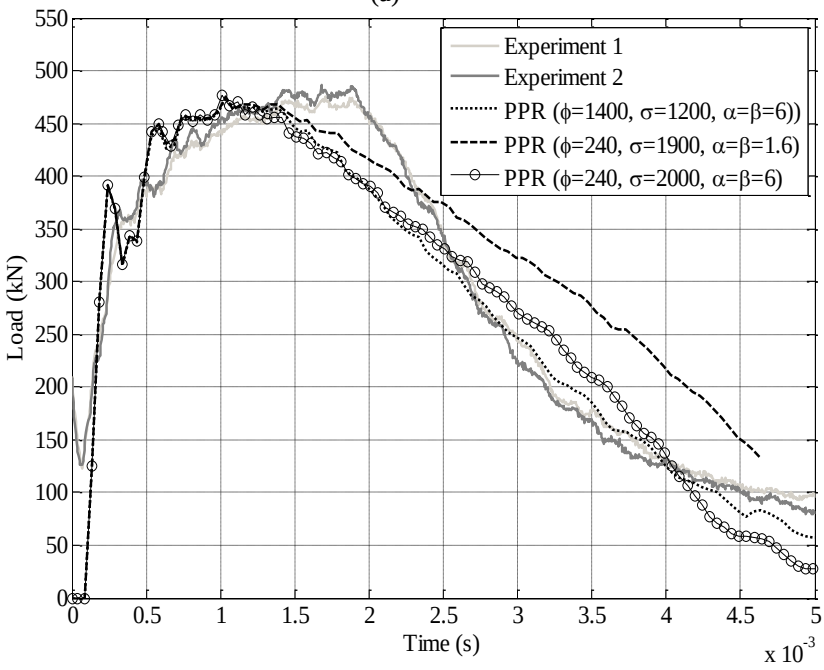

(b)

Figure 1.13: BDWT test deformed configuration at time = 2.8ms with Von Mises stress (MPa) overlaid (a) and comparison of the specimen's load bearing capacity versus time, experimental and numerical (b).

To demonstrate the PPR model's ability to model intergranular fracture, a synthetic polycrystal generated with a Voronoi tessellation technique was considered. The microstructure was volumetrically meshed with tetrahedra, cohesive elements were inserted along the grain boundaries, and the model was loaded statically in simple tension with a 3% applied strain, Figure 1.14. One analysis was performed with the

PPR model describing the constitutive response of the grain boundaries; a second analysis was performed with the Tvergaard and Hutchinson coupled CZM.

The cohesive parameters used in the analyses are given in Table 1.2 and Table 1.3. Note that the parameters were chosen to yield nearly identical cohesive behavior. For example, cohesive strengths, final crack opening widths, and softening behavior were matched, rendering discrepancies in numerical metrics like solver convergence solely the product of the coupled / uncoupled nature of the models. The bulk material was assigned linear elastic, isotropic behavior with E = 75GPa and ν = 0.33.

Table 1.2: PPR model parameters.

σ_{max}, τ_{max}	ϕ_n, ϕ_t	λ_n, λ_t	α, β
450 MPa	1136 N/mm	0.005	2

Table 1.3: Coupled CZM parameters.

$T_{max\ coupled}$	k_o	δ_n, δ_t
450 MPa	50 * $T_{max\ coupled}$	0.005 mm

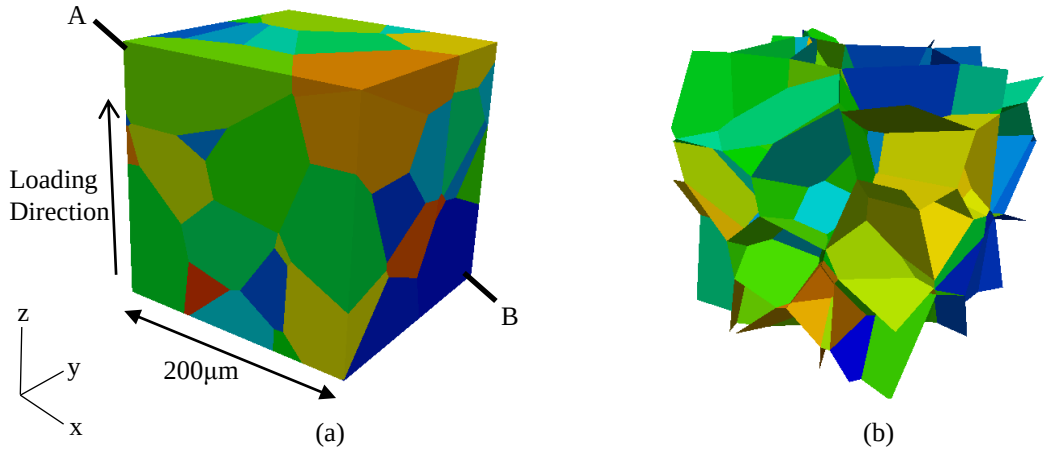

Figure 1.14: Cubic polycrystal model (a) and corresponding cohesive grain boundary surfaces (b).

FEAWD was used to formulate and solve the nonlinear system, employing a trust region nonlinear solver, a conjugate gradient Krylov subspace method, and a Jacobi preconditioner as implemented in PETSc. The default linear and nonlinear solver

tolerances were used. Converged function norms for the analyses are given in Figure 1.15. Here, convergence is reached once the l^2-norm of the residual is less than or equal to the product of the l^2-norm of the residual evaluated at the initial guess and a user-specified relative tolerance (1e-4 in this study). It is apparent that once an appreciable amount of cohesive softening was initiated in the polycrystal, the nonlinear solver in the coupled CZM analysis struggled to converge to pre-softening levels, raising doubts about the accuracy of the resulting output. The nonlinear solver in the PPR analysis, on the other hand, had some difficulty reaching pre-softening levels of convergence for the intermediate load steps; however, unlike the coupled analysis, the solver fully recovered for the final 300 load steps.

Locking can be blamed for the convergence trend of the coupled CZM analysis. Referring to Figure 1.16, a plot of stress in the loading direction at 2.4% strain across line A-B in Figure 1.14(a), it is apparent that the models converged to different answers. While both models developed a through crack at the same location, the stresses in Figure 1.16 indicate an abnormality in the center of the coupled model. It is apparent that the PPR model has nearly completely unloaded; however, the coupled model has obviously retained a significant capacity to resist complete decohesion. Given the unrealistic nature of this result, particularly a small segment of a grain boundary being able to resist complete decohesion, and the nonlinear solver's poor performance discussed previously, it is apparent that the coupled CZM model's solution is unrealistic while the PPR model is physically acceptable.

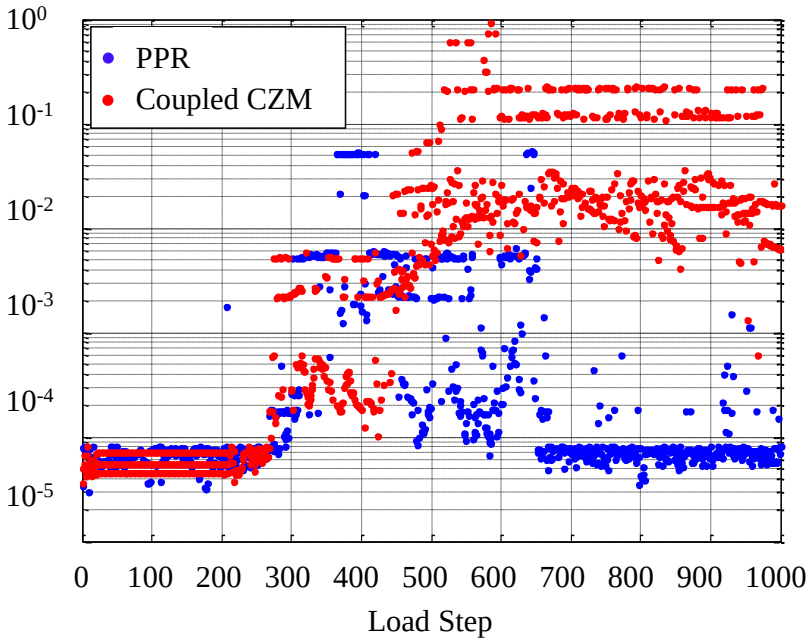

Figure 1.15: Nonlinear function norms for polycrystal analysis.

The PPR model's application in a polycrystalline finite element analysis is discussed here. DREAM.3D [43,44] was used to create a statistically representative 240-grain microstructure of a nickel-based superalloy with an annealed twin in the center; the geometry was volume meshed, with cohesive elements along the grain boundaries, loaded in simple tension, and analyzed in FEAWD, Figure 1.17(a). A grain-size-sensitive crystal plasticity model was employed to model bulk behavior while the PPR model accounted for grain boundary decohesion. A model with perfectly bonded grains and another with PPR cohesive grain boundaries were considered.

The mesh with cohesive grain boundaries had 12.6-million degrees-of-freedom (DOFs) and 272,636 quadratic, triangular cohesive elements. The simulation ran on 512 processors on the Texas Advanced Computing Center's Sun Constellation Linux cluster Ranger for approximately twelve hours before slip began to accumulate on the slip systems. The sum of the accumulated irreversible slip on the six cubical and twelve octahedral slips systems, $\sum_{\alpha=1}^{18}\gamma^{\alpha}$, was considered throughout both polycrystals, mapped to a line extending from A to B in Figure 1.17(a) as shown in Figure 1.17(b).

Grain boundary decohesion altered the slip state in the microstructure, in some grains facilitating slip while in others impeding it.

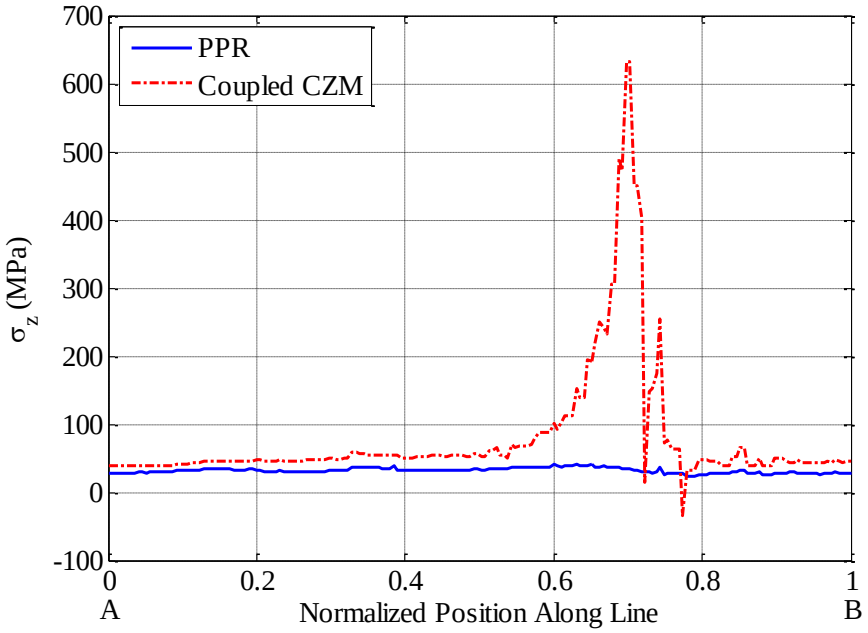

Figure 1.16: Plot of σ_z along line A-B shown in Figure 1.15(a) at 2.4% strain.

Intergranular fracture is a complex microstructural deformation mechanism, and the investigations presented herein are included simply to motivate further study and establish the PPR model as an adequate means to address this phenomenon in a HPC FE framework. Obviously, to model this mechanism accurately, cohesive parameters would need to be calibrated, and there is no guarantee that a single set of parameters would be appropriate for every grain boundary in the microstructure. For example, special consideration would need to be paid to triple junctions and twin boundaries.

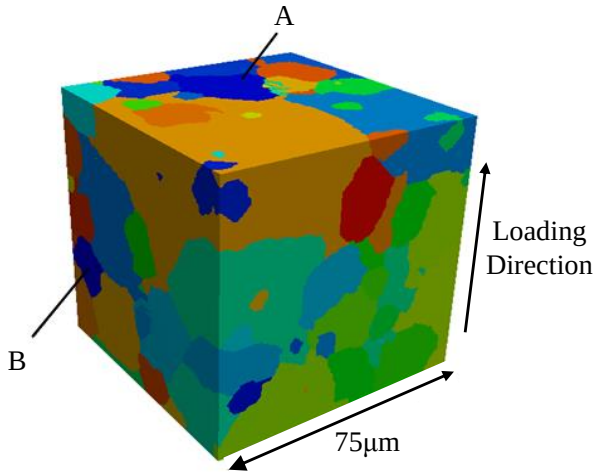

(a)

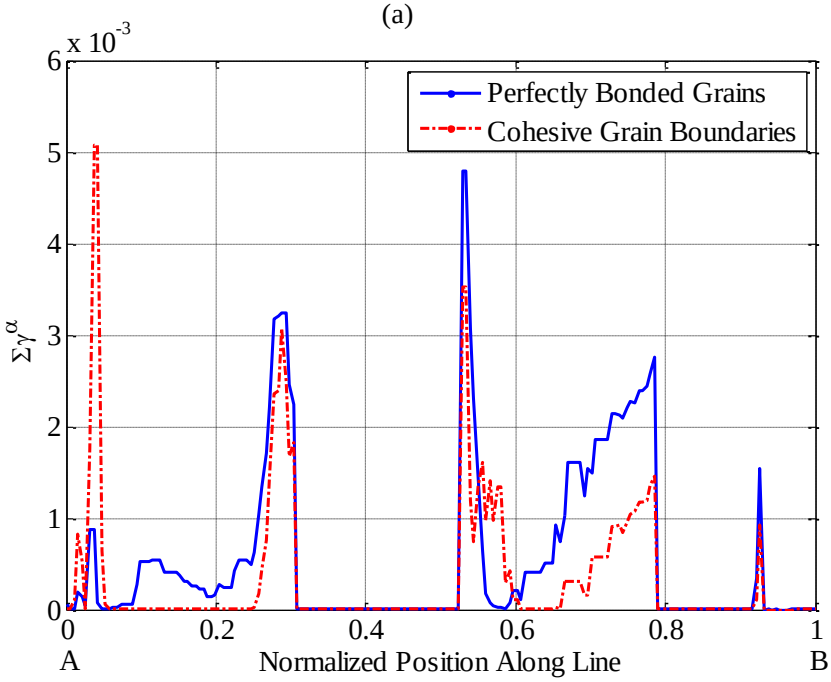

(b)

Figure 1.17: DREAM.3D-generated cubic polycrystal (a) and sum of slips on FCC octahedral and cubical slip systems throughout polycrystal at 0.30% strain, with and without PPR CZM on grain boundaries (b).

1.4 Conclusions and Extensions

This paper has detailed the PPR model's extension to three-dimensions and demonstrated its efficacy in modeling mixed-mode fracture in single-core and HPC applications across a variety of applications. A description of the PPR model in relation

to the prevailing cohesive zone modeling methodologies, its formulation in three-dimensions, and its implementation in a three-dimensional finite element framework were given. The appendix contains a formulation of the material tangent stiffness matrix and provisions for unloading / reloading and contact.

The T-peel joint (mode I), MMB (modes I and II), and ECT (modes II and III) specimens were modeled to verify the three-dimensional PPR implementation. The T-peel PPR simulations yielded experimentally-consistent Mode I behavior. The MMB PPR simulation reproduced accurately the analytically-predicted results. The ECT simulations, with both Mode II and III components, yielded experimentally-consistent load-displacement data for different crack lengths. The Battelle Drop Weight Tear test was modeled to demonstrate the PPR model's capability for dynamic loading and gauge its ability to model the high rate of crack propagation inherent to the experiment. Here, the PPR model was shown to capture adequately experimental load-bearing behavior. Finally, the case of intergranular fracture was considered to demonstrate the PPR model's performance under severe mode-mixity in a HPC environment. It was shown that the PPR model outperforms a coupled CZM in modeling intergranular fracture, not only because it is energetically consistent, but also because it does not present the nonlinear solver a computationally intractable problem to solve. The PPR model, therefore, could be extended to many applications where the crack path is not known *a priori* and the loading is such that a high degree of mode-mixity exists in the continuum.

Such extensions could use the PPR model (as described in this paper) as the basic platform in which additional physics could be inserted. These extensions include anisotropic sliding behavior (as pointed out in Section 1.2.3), rate dependency in the traction-separation relationship, healing effect (relevant for asphalt and other polymer-based composites), and functionally graded cohesive behavior to account for interphase

changes (in this case the cohesive properties are functions and not constants anymore). Some of these issues are currently being pursued by the authors.

1.5 Acknowledgements

This research was funded by the Air Force Office of Scientific Research under grant number FA9550-10-1-0213, supervised by Dr. David Stargel. This work used the Extreme Science and Engineering Discovery Environment (XSEDE), which is supported by National Science Foundation grant number OCI-1053575. Support from the Donald B. and Elizabeth M. Willett endowment at the University of Illinois at Urbana-Champaign (UIUC) is gratefully acknowledged, as is support from the Ross-Tetelman Fellowship at Cornell University. The authors would also like to acknowledge Dr. Gerd Heber of the HDF Group for assistance with FEAWD and Dr. Joe Tucker of Carnegie Mellon University's Department of Materials Science and Engineering for generating the 240-grain microstructure considered in the intergranular fracture case study. Any opinion, finding, conclusions or recommendations expressed here are those of the authors and do not necessarily reflect the views of the sponsors.

CHAPTER 2

A USE CASE FOR DIGITAL TWIN

The use case presented herein has two functions. First, it clarifies and motivates Digital Twin, a new paradigm that promises unprecedented fleet management capabilities. Second, it underscores the importance of retaining as much fidelity in the numerical model as possible and highlights the adverse consequences of making seemingly valid simplifications and trivial oversights.

With regards to the first function, the use case illustrates the consequence and benefit of including as-manufactured component geometry, a corner stone of Digital Twin, in a modeling framework. Specifically, the "component" is a non-standardized material test specimen. Thirteen of these specimens were manufactured with a relatively tight machine tolerance from the same plate and subjected to identical loading conditions. A fleet manager, for example, would expect these specimens to behave identically throughout their service life; however, each failed along one of two likely failure paths. The result of small deviations in geometry (on the order of tenths of a millimeter), this crack path ambiguity suggests that the specimen does not have a single representative geometry.

To resolve this crack path ambiguity, a continuum plasticity damage model is coupled with as-machined, digital twin geometries of the specimens. For the most part, the continuum model retains enough fidelity to resolve accurately the crack path of each specimen; however, in configurations with pertinent geometric features only a few grain sizes away from the bifurcation, it fails. This does not suggest that the continuum plasticity damage model is flawed in any way, just that it lacks the fidelity necessary to handle some of the more sensitive configurations accurately. Specifically, a drop in length scale might be required.

At the bifurcation, it is possible that microstructural features (i.e. grain boundary character, grain sizes and orientations, etc.) dictate the nucleation of microcracks and their propagation into one of the two observed crack paths at the macroscale. For example, a nucleated microcrack in the microstructurally small regime will interrogate grains based on local microstructural character. The crack will only begin to propagate independently of the microstructure when it is microstructurally large (~100 μm); however, by this time, it could have propagated in the direction of one of the two observed crack paths to actually trigger that failure path in the specimen. To account for this phenomenon, a microstructure-based framework is needed. To this end, the framework discussed in Chapter 3 of this dissertation could be used to account for microcrack nucleation. The PPR cohesive zone model, in turn, as demonstrated in Chapter 1, could be used to model microstructurally small propagation along grain boundaries.

2.1 Introduction

Current structural life-management approaches consider a variety of sources of uncertainty in producing reliability estimates. Typically, an empirically based worst-case scenario is considered for design and scheduling inspections. However, relying on the worst-case scenario seen during testing assumes that in-service loading conditions are well understood, the tails of distributions of material behavior are accurately modeled, and all damage modes that lead to reduced life are accounted for during testing. During service, decisions regarding the capability of a structure to endure a mission are based on these uncertainty and reliability estimates, along with relatively basic information of initial design specifications, usage history, and nondestructive evaluation (NDE) and maintenance records. Unfortunately, without a detailed record of vehicle-specific usage, variability in vehicle usage across a fleet only adds to the uncertainty in the state of a particular vehicle. Furthermore, this assumption of representative, worst-case conditions leads to costly inspection or replacement of parts which likely contain acceptable damage [45].

By Bayesian inference, it is possible to combine new usage data with existing predictions to improve continually reliability estimates throughout the service life of a vehicle. However, such a trend can only occur if vehicle-specific initial (and updated) state, usage history, and NDE findings are recorded throughout the service life, and subsequently used for updated prognoses. This is because no two structural components within a fleet are equivalent in as-built geometry or material microstructure, and no two vehicles experience equivalent usage or environment during their lifetime.

Digital Twin [46,47] is an emerging management and certification method designed to address these existing issues. In addition to being a more accurate and efficient management approach, Digital Twin will also enable new paradigms in certification and design. For NASA, the concept vehicles that will enable future missions must be

designed for conditions which might not be repeatable in the lab, and will likely experience loads and environments that were not foreseen during the design phase. These demands preclude current approaches and raise three specific issues to be addressed: (1) Certification verification - by test - might not be possible under the current methods. (2) Unexpected and individually experienced loads and environments modify the expected life, necessitating a management method in which the limit loads decrease accordingly throughout each vehicle's service life. (3) Heuristics do not exist for the multifunctional next-generation materials that will be required on future vehicles. Therefore, current design approaches, which rely heavily on heuristic-based safety factors, should be replaced.

The Digital Twin concept is early in its development, hence there are many requisite portions yet to be studied and assembled. This paper does not detail Digital Twin in its entirety— topics such as multi-scale and multi-physics modeling, model integration, and computational demands are beyond the scope of this work. This paper focuses on the efficacy of modeling and simulating the as-built geometry of each individual component in a fleet, a cornerstone of Digital Twin, and aims to both motivate and better define Digital Twin with a straight-forward use case.

The presented use case, ductile fracture in a non-standardized material test specimen, dispels the notion that modeling damage in a component can be done with nothing but a representative geometry, a seemingly well-calibrated constitutive model, and sound engineering judgment. A degree of personalization is required. Specifically, the non-standardized geometry was observed to fail along one of two crack paths. A result of deviations in geometry on the order of tenths of a millimeter, this crack path ambiguity suggests that the specimen does not have a single representative geometry and motivates modeling the as-machined components. Thereby, the effectiveness of considering these digital twin specimens in resolving the crack path ambiguity is demonstrated.

This paper is divided into three parts. In the first, Section 2.2, to contextualize the research presented herein, the general operation of Digital Twin is discussed. In the second, Sections 0, 2.4, and 2.5, digital twin specimens are implemented in an over-the-counter computational model for resolving crack path ambiguity in a geometry designed for the 2012 Sandia Fracture Challenge [48]. This computational model is refined during the course of the study, thereby mimicking some of the data acquisition / contextualization and updating procedures within Digital Twin. In the third part, Section 2.6, the model is scrutinized for its effectiveness and adherence to the cornerstones of Digital Twin, namely Verification, Validation, and Uncertainty Quantification (VVUQ) and personalization. Hereafter, *Digital Twin* refers to the paradigm and *digital twin* refers to an instantiation.

2.2 Operation of Digital Twin

This section gives an overview of the Digital Twin concept to provide context for the subsequent discussion on modeling as-manufactured components. Additionally, it is intended to summarize the current state of the art which has been the result of collaborators in a working group[1] interested in the development of Digital Twin. The diagram in Figure 2.1 depicts an overview of Digital Twin, which is a multi-level concept where many of the elements shown are not fully developed. One element of the Digital Twin concept that is not considered here is sensor-based measurement of usage (load and environment) as tests in the present case were completed in lab conditions with predefined loading. A second element that is not considered in depth is the Bayesian updating of the digital twin throughout the components' lives. Nonetheless, it is shown that with the consideration of as-built geometry in predicting individual component behavior, significant improvements over using a single representative model are realized.

[1] the community collaboration website is located at http://adt.larc.nasa.gov/

In its fully realized state, Digital Twin will incorporate aerothermodynamics, structural mechanics, materials science, sensing, statistics, and uncertainty methods. It will utilize modeling and simulation of the as-built vehicle state, as-experienced loads and environments, and other vehicle-specific history to enable high-fidelity modeling of individual vehicles throughout their service lives. Under this method, each as-manufactured aircraft (and their life-critical components) will be digitally replicated, then managed based on the data gathered from on-board sensors and damage progression simulations. Therefore, Digital Twin is an evolutionary evidence- and prognosis-based management strategy providing information regarding the specific components in a fleet that should be inspected closely or replaced. With the advent of high performance and high fidelity computational modeling, improved experimental methods, and integrated data management systems, both aleatoric and epistemic uncertainty in these systems could be reduced [49,50] and lead to more efficient designs and proactive maintenance.

A digital twin rests on three highly interconnected pillars each of which represents collections of databases, models, and hierarchical and parallel information flows and processing, Figure 2.1. The tapered shape is to suggest massive parallel processing of large amounts of homogeneous, noisy data in the lower parts giving way to drastically reduced, heterogeneous, abstracted information near the top. The digital twin's behavior, the input/output relationship, is shaped by its internal state and its purpose or intent, which together give it a persona or identity (iDT). At this level, digital twins become comparable, can be related and organized in social network-like structures or aggregate digital twins that in turn could be used to capture population-level patterns and behaviors.

The identity of a digital twin is formulated through a cyclic, complex series of events beginning with data acquisition from the physical twin. Sensors, for example, can

measure a myriad of data including acceleration, pressure, and temperature. Prioritization proceeds wherein quantities of interest (QOIs) are identified and models are selected. Factors such as fidelity and scale are considered in the context of acceptable levels of uncertainty and available computational resources in choosing appropriate models. These models are then analyzed. Afterwards, the models' outputs are integrated, differential diagnosis is performed, and the internal state of the digital twin is updated, which includes updates from other twins. An inspection or repair regimen is formulated for each diagnosis in the second half of the cycle. Herein, decisions to execute an action are made. Based on this go/no-go decision, the diagnosis is either neglected or acted upon. If acted upon, a plan is developed to address the diagnosis and a prognosis, which forecasts the likely course of the plan, is subsequently formulated from an additional round of modeling. For example, a plan could be replacement of a component and its prognosis could be that the structure becomes more damage tolerant. If simulation results indicate that the strategy is ineffective, a new plan might be formulated or action might be abandoned altogether. If effective, the plan is administered to the physical twin. Thereafter, the physical twin is monitored. Data are then reacquired by the digital twin and the cycle repeats.

2.3 The 2012 Sandia Fracture Challenge

2.3.1 Overview

The Sandia Fracture Challenge (SFC) was issued by Sandia National Laboratories in partnership with the National Science Foundation (NSF) and Naval Surface Warfare Center Carderock Division in 2012 to predict crack initiation and propagation in a novel geometry, the "challenge specimen" hereafter. For details regarding the experiments and the round robin predictions made by the thirteen participants, the reader is directed to the SFC lead article [48]. This section serves as a brief summary of the experimental

setup, the challenge requirements, relevant experimental outcomes, and the participants' approaches.

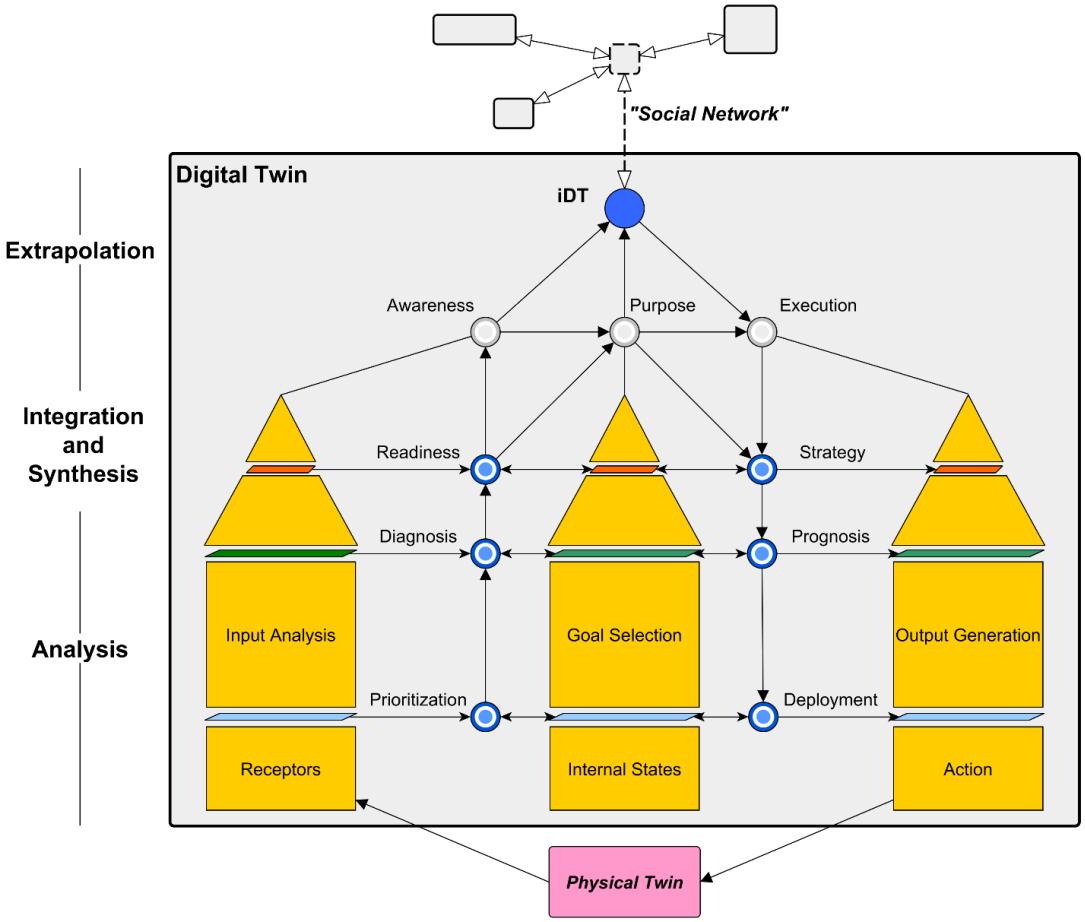

Figure 2.1: Notional Diagram of Digital Twin. Inspired by Kent [51].

2.3.2 Experimental Setup

The material of interest was an off-the-shelf alloy, 15-5 PH: a precipitation hardened stainless steel. Thirteen challenge specimens as well as tensile and fracture toughness test specimens were machined from the same plate. It is noteworthy that the challenge specimens were machined with a 0.0508 mm tolerance on all dimensions; however, not all of the specimens were machined to specifications, making for the peculiar experimental results detailed in Section 2.3.4. The nominal dimensions of the challenge specimen are given in Figure 2.2.

The challenge specimen has several similarities with a standard CT fracture toughness specimen but has three holes beyond the blunt notch. Following Figure 2.2, a labeling convention is used to identify pertinent features of the specimen: blunt notch (A); 3.05 mm-diameter hole (D); 1.78 mm-diameter hole beyond blunt notch (C); 1.78 mm-diameter hole above holes C and D (B); and the midpoint of the far-right edge (E). Each specimen was loaded at the pin holes at a rate of 0.0127 mm/s. All tests were conducted at lab ambient temperature.

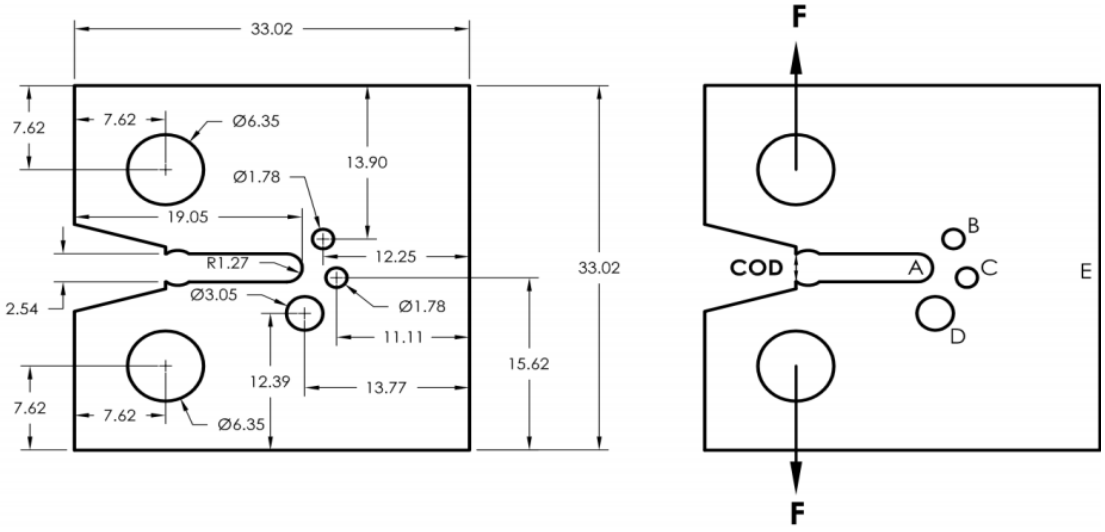

Figure 2.2: Nominal dimensions of challenge specimen with 3.18 mm nominal thickness. All dimensions in millimeters. Figure adapted from the SFC lead article [48].

2.3.3 Quantities of Interest

Each team was required to predict six quantities of interest (QOIs) identified by Sandia. They were:

1. crack path
2. load vs. crack opening displacement (COD), Figure 2.2
3. load when a crack first initiated
4. COD when a crack first initiated
5. load when a crack later reinitiated from a second feature (i.e. holes B or C)
6. COD when a crack later reinitiated from a second feature (i.e. holes B or C)

2.3.4 Experimental Outcomes: Crack Path Ambiguity

Two crack paths were observed in the challenge specimens: A-C-E and A-D-C-E. Of the thirteen specimens, ten cracked along the path defined by A-D-C-E (D2, S1, S2, S3, S4, S5, S6, S7, S8, and S11) while three cracked along A-C-E (D1, S9, and S10). It is noteworthy that only one of the specimens was machined to specifications and its crack path was A-C-E; the others exhibited deviations beyond the 0.0508 mm machine tolerance ranging from microns to twice the tolerance. After extensive analysis, Boyce *et al*. [48] determined that these deviations from the nominal dimensions were to be blamed for the ambiguity in crack path.

In particular, the location of hole C in relation to hole D was decisive. Specimens with holes C and D separated by 2.381 mm or less (measured here as the vertical distance between the tops of holes C and D) consistently cracked along A-D-C-E. Conversely, specimens whose crack path was A-C-E exhibited distances between holes C and D of 2.401 mm, 2.393 mm, and 2.397 mm. An outlier specimen, S11, had holes C and D separated by a distance of 2.398 mm, but cracked along A-D-C-E. To rationalize this outlier, Boyce *et al*. [48] considered the ratio of the vertical distance between the blunt notch (A) and hole D to the horizontal distance between the blunt notch (A) and hole C and determined that this ratio for the S11 specimen, along with the other specimens' ratios which cracked along A-D-C-E, were greater than machine tolerance.

The load vs. COD profiles for the thirteen specimens are given in Figure 2.3. Perhaps most obvious from the profiles is that specimens that cracked along A-C-E had a considerably longer delay in the first load drop than specimens that cracked along A-D-C-E. The overall load drop from A to C for all specimens was roughly 3 kN, but the change in total COD for specimens that cracked along A-D-C-E during this reduction was greater than that of specimens that cracked along A-C-E.

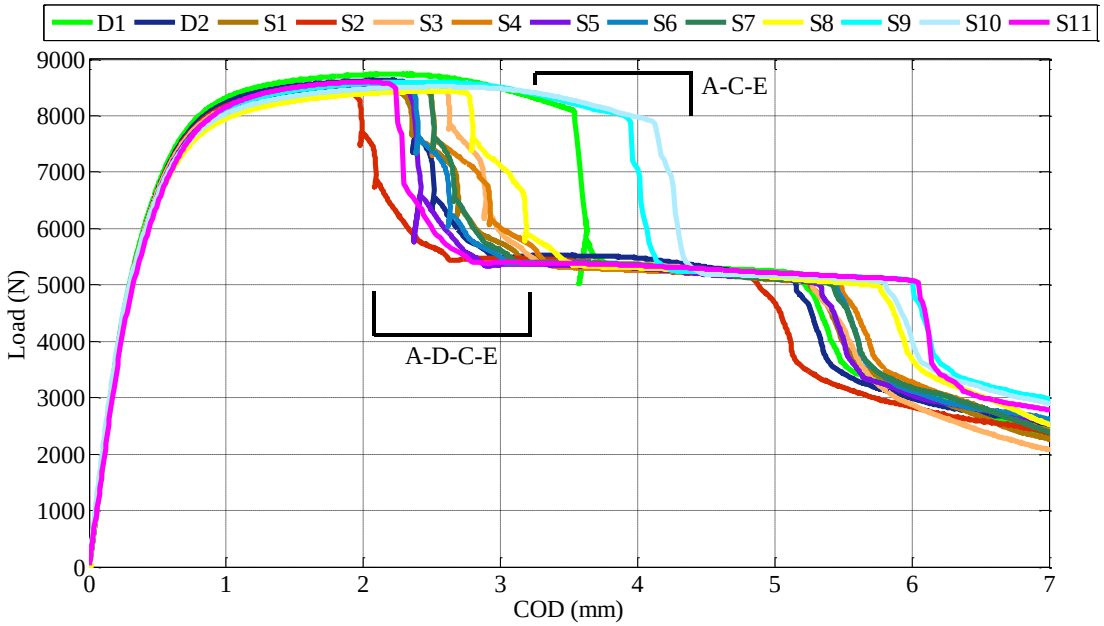

Figure 2.3: Load vs. COD measurements for thirteen challenge specimens [48,52].

2.3.5 Survey of Participants' Predictive Capabilities

An extensive array of capabilities was employed to predict the six QOIs. Several teams used porous metal plasticity (void growth) models [53]. Others employed von Mises plasticity supplemented by a fracture model (i.e. Mohr-Coulomb [54] and Johnson-Cook [52]). The extended finite element method (XFEM) [55], material point method, peridynamic theory, and cohesive zones were also employed. Some of these methods outperformed others in determining some of the QOIs, but perhaps most startling is that no single model sufficiently and definitively addressed all of the QOIs. The following section details one of these models: a commercially available, porous metal plasticity-based approach.

2.4 Computational Model

2.4.1 Material Model and Calibration

The porous metal plasticity model implemented in Abaqus/Explicit [56] is a void-growth plasticity model given by Gurson [57]. Both the elastic response and hardening behavior are isotropic. The yield condition is given by:

$$\Phi = \frac{\sigma_e^2}{\sigma_M^2} + 2f\cosh\left(\frac{\sigma_k^k}{2\sigma_M}\right) - (1 + f^2) = 0\ , \tag{2.1}$$

where f is void volume fraction, σ_e the effective Mises stress, σ_M the yield stress of the fully dense matrix, and σ_k^k three-times the macroscopic mean stress. Tvergaard [58] modified Equation 2.1 to include yield surface parameters q_1, q_2, and q_3:

$$\Phi = \frac{\sigma_e^2}{\sigma_M^2} + 2fq_1\cosh\left(\frac{q_2\sigma_k^k}{2\sigma_M}\right) - (1 + q_3f^2) = 0\ , \tag{2.2}$$

where Gurson's yield condition is recovered for $q_1 = q_2 = q_3 = 1$. Damage is introduced into the model by way of void coalescence. Two user-defined parameters control this process: critical void volume fraction, f_c, and void volume fraction at total failure, f_f. If the void volume fraction exceeds f_f, a material point loses all capacity to carry stress. Moreover, if all of an element's material points fail, the element is removed from the discretization. If a material point's void volume fraction falls between f_c and f_f, f in Equation 2.2 is replaced by the expression

$$f_\mathrm{c} + \frac{\dfrac{q_1 + \sqrt{q_1^2 - q_3}}{q_3} - f_\mathrm{c}}{f_\mathrm{f} - f_\mathrm{c}}(f - f_\mathrm{c}) \tag{2.3}$$

The Gurson model with Tvergaard's modification was calibrated against both the 15-5 PH tensile and fracture toughness test data detailed in the SFC lead article [48]. The test geometries were generated in Abaqus/CAE and meshed with 200 μm-sized quadratic tetrahedral elements. The calibration was conducted in two stages. In the first, several candidate sets of parameters were identified that reproduced the experimental stress-strain tensile data. Thereafter, the candidates that did not accurately reproduce the reduction in cross-sectional area observed during the tensile tests were discarded. In the second stage, the fracture toughness test was simulated with the remaining candidates, and the set that most accurately reproduced the measured force vs. COD was retained for the production-level challenge specimen simulations. This set is given in Table 2.1 and Table 2.2.

Table 2.1: Calibrated porous metal plasticity parameters.

Parameter	Value	Parameter	Value
Mass Density	7.8 g/mm^3	ε_N	0.09 mm/mm
E	235.4 GPa	s_N	0.001 mm/mm
ν	0.272	f_N	0.01
r	0.99	f_f	0.18
q_1, q_2, q_3	1, 1, 1	f_c	0.10

Table 2.2: Parameters for tabular hardening curve.

Plastic Strain (mm/mm)	Yield Stress (MPa)	Plastic Strain (mm/mm)	Yield Stress (MPa)	Plastic Strain (mm/mm)	Yield Stress (MPa)
0.0	1092.5	0.05111	1181.7	0.12	1250.0
0.01649	1127.6	0.06852	1198.5	0.16	1320.0
0.03404	1156.7	0.07429	1200.0	1.0	1350.0

2.4.2 Mesh Refinement and Sensitivity

It is well established that solutions from porous metal plasticity models are mesh sensitive. Mesh refinement studies were conducted on the challenge specimen with nominal dimensions. Nominal dimension were used initially since no as-manufactured geometry was provided. 200 μm-sized tetrahedral elements were placed beyond the blunt notch (A) and around the holes B, C, and D because this element size was used during calibration. As shown in Figure 2.4, depending on the extent of these 200 μm-sized elements beyond the holes, the crack was predicted to propagate along one of two paths, A-C-E or A-D-C-E. In cases where the mesh was coarsened to the back edge, E, the predicted crack path was A-D-C-E; however, in cases where the 200 μm-sized elements were retained out to E, the predicted crack path was A-C-E. The latter result is in agreement with experimentation— the one specimen machined to specifications (i.e. within 0.0508 mm of nominal) cracked along A-C-E. Consequently, for all production-level simulations with the challenge specimen, the 200 μm-sized tetrahedral elements were retained up to E.

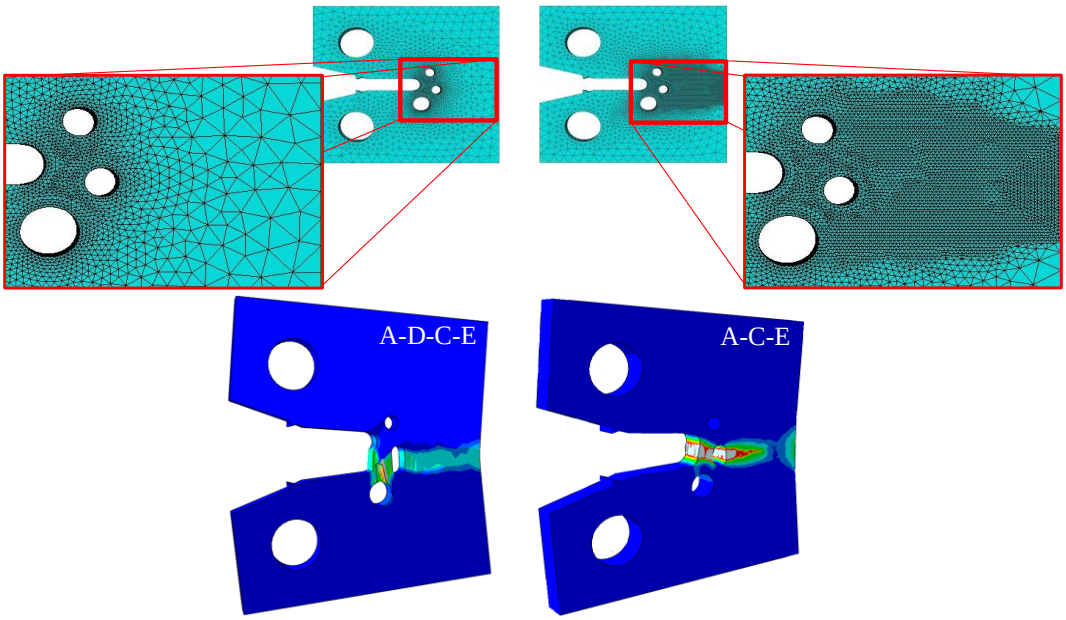

Figure 2.4: Influence of mesh refinement on predicted crack path.

2.4.3 Challenge Specimen's Boundary Conditions and Computational Demands

The loading pins' action on the specimen was modeled with kinematic coupling constraints. The loading pin closest to hole B was held stationary while the other was gradually displaced downwards 7.5 mm. A kinematic boundary condition was assigned to a single node near E to restrict rigid body rotation.

All production-level runs had approximately 5.5 million degrees of freedom. Simulations were conducted on a 3.40 GHz, 4th generation Intel Core i7 processor. Abaqus/Explicit's shared memory parallelization on four threads with a targeted time increment of 1e-6 seconds resulted in approximately a 4-day wall-clock run time. However, explicit integration of a finite element model scales well since the global stiffness matrix is not formed (and therefore, also not inverted) and the mass matrix can be diagonalized, resulting in a system of uncoupled equations. Therefore, it is expected that the simulation time could be significantly reduced for codes where the number of employed CPUs at runtime is not limited by the number of available software licenses.

2.5 Numerical Simulations and Results

2.5.1 Overview

The computational model was initially employed to predict fracture in the challenge specimen. Since no as-manufactured geometries were provided initially, the prediction was conditioned on a single (nominal) geometry, Section 2.5.2. After the blind prediction had been made, as-manufactured configurations were considered for probing the model's ability to resolve the ambiguity in crack path, Sections 2.5.2-2.5.4. Finally, based upon experimental results, the model was updated with new porous metal plasticity model parameters to improve its predictive capabilities, Section 2.5.5.

2.5.2 Modeling the Challenge Specimen with Nominal Dimensions

The challenge specimen with the nominal dimensions given in Figure 2.2 was modeled for determining a baseline simulated crack path and load vs. COD profile. The predicted crack path was A-C-E, Figure 2.5, an expected result considering the only specimen manufactured within machining tolerances, D1, cracked along A-C-E. The predicted peak load and magnitude of the first load drop agreed with D1's profile; however, the predicted 0.8 mm change in total COD during the first load drop was far greater than that of any of the thirteen specimens.

As with the nominal specimen, the simulation of the D1 digital twin specimen predicted an A-C-E crack path, matching the experiment, Figure 2.6. The predicted peak load was only 2.2% lower than that measured during the experiment. Moreover, the simulation predicted the magnitude of the first load drop relatively accurately; however, the predicted 1.0 mm change in total COD during the first load drop was far greater than that observed. The crack's initiation from hole C was not captured in the simulation; due to excessive element deformation, a converged solution could not be reached and the simulation subsequently terminated. This was not the result of physical phenomena, rather the violation of the Courant-Friedrichs-Lewy (CFL) condition [59].

Moreover, due to limitations with Abaqus/Explicit, new elements could not be adaptively inserted into the discretization to circumvent this issue.

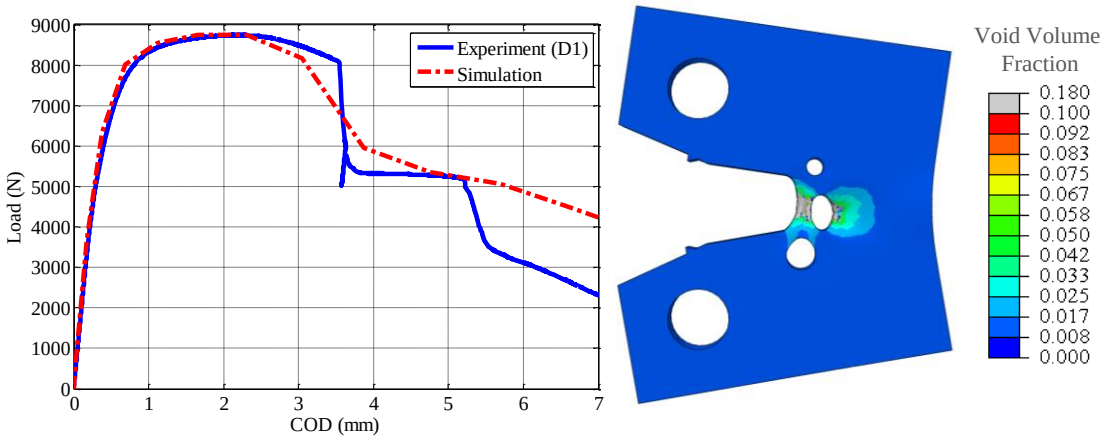

Figure 2.5: Experimental load vs. COD profiles for D1 specimen and simulated load vs. COD profile for nominal specimen, left. The contour of void volume fraction, showing void accumulation along ligament A-C, taken at load = 4,471 N, right.

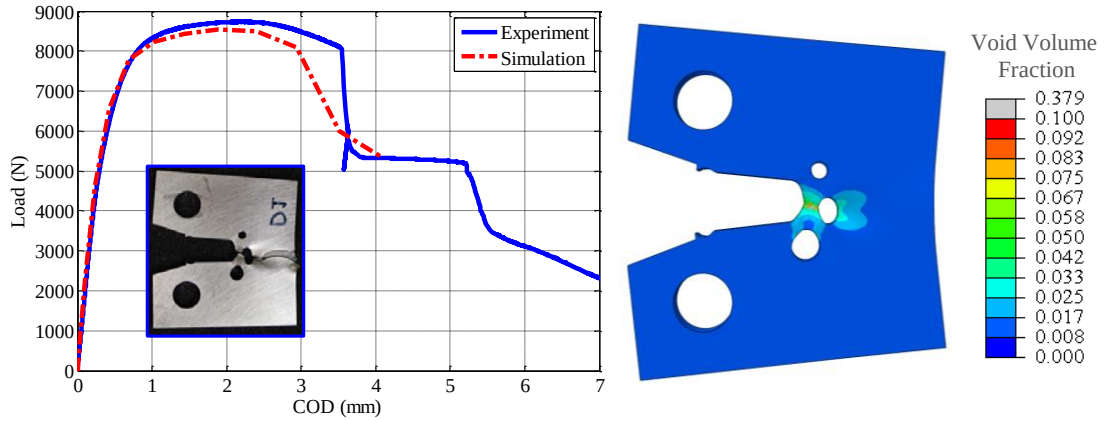

Figure 2.6: Experimental and simulated load vs. COD profiles for D1 specimen, left. The contour of void volume fraction, showing void accumulation along ligament A-C, taken at load = 5,333 N, right.

2.5.3 Modeling the S5 (out of specifications) Specimen

The S5 specimen, one exhibiting some of the largest deviations from specifications, was one of ten in which the crack propagated along the A-D-C-E path. With regards to the aforementioned ratio of the vertical distance between the blunt notch (A) and hole D to

the horizontal distance between the blunt notch (A) and hole C, the S5 specimen exhibited the largest deviation from nominal.

The simulation of the S5 digital twin specimen reproduced the A-D-C-E crack path, Figure 2.7. The predicted peak load was virtually identical to the experimental peak. As with the D1 specimen, the magnitudes of the simulated and experimental load drops were nearly indistinguishable; however, the predicted 1.7 mm change in total COD during the first load drop was far greater than the observed 0.5 mm.

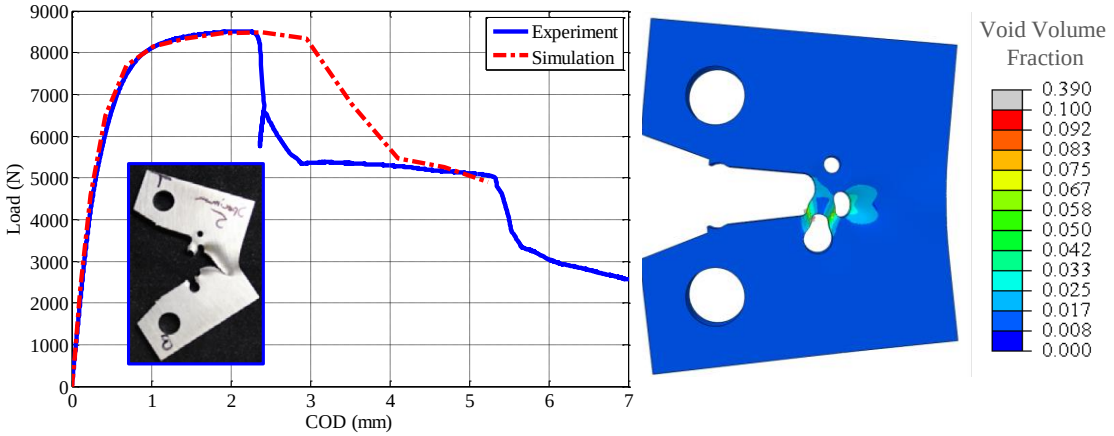

Figure 2.7: Experimental and simulated load vs. COD profiles for S5 specimen, left. The contour of void volume fraction, showing void accumulation along ligaments A-D and D-C, taken at load = 5,474 N, right.

2.5.4 Modeling the S11 (slightly out of specifications) Specimen

The S11 specimen, one exhibiting slight deviations from specifications, was one of ten that cracked along A-D-C-E. This result was somewhat peculiar because the spacing between holes C and D in the S11 specimen was characteristic of specimens which cracked along A-C-E. As mentioned earlier, its ratio of the vertical distance between A and D to the horizontal distance between A and C was greater than machine tolerance (a characteristic of all specimens failing A-D-C-E), and this is perhaps the best, and only, geometric-based explanation as to why the S11 specimen cracked along A-D-C-E.

The simulation of the S11 digital twin specimen did not reproduce the A-D-C-E crack path, Figure 2.8. As with the simulations discussed previously, the peak load was accurately predicted and the simulated change in total COD during the first load drop was significantly higher than the measured peak load. To shed light on the inaccurate prediction of crack path, additional analyses were conducted. Hole C was shifted incrementally closer to hole D until the A-D-C-E crack path was predicted. A 50 μm downward vertical translation of hole C was not enough to yield an A-D-C-E path; however, as shown in Figure 2.8, compared to the simulation of the S11 specimen, the void volume fraction between the blunt notch A and hole C significantly declined while it increased between the blunt notch A and hole D, indicating a stronger propensity for crack growth into hole D. A subsequent 10 μm translation (making for a total translation of 60 μm) resulted in the A-D-C-E crack path.

With regards to the predicted load vs. COD profiles, the two simulations showing A-C-E had relatively similar curves. A smaller COD was required to initiate first load drop in the S11 specimen compared to D1 and S5— an expected result as a significant amount of COD went into plastically deforming the ligaments A-D and A-C in the other model. The simulation with the 60 μm translation had problems converging due to excessive element deformation as the ligament A-D was beginning to fail, again the result of violating the CFL condition.

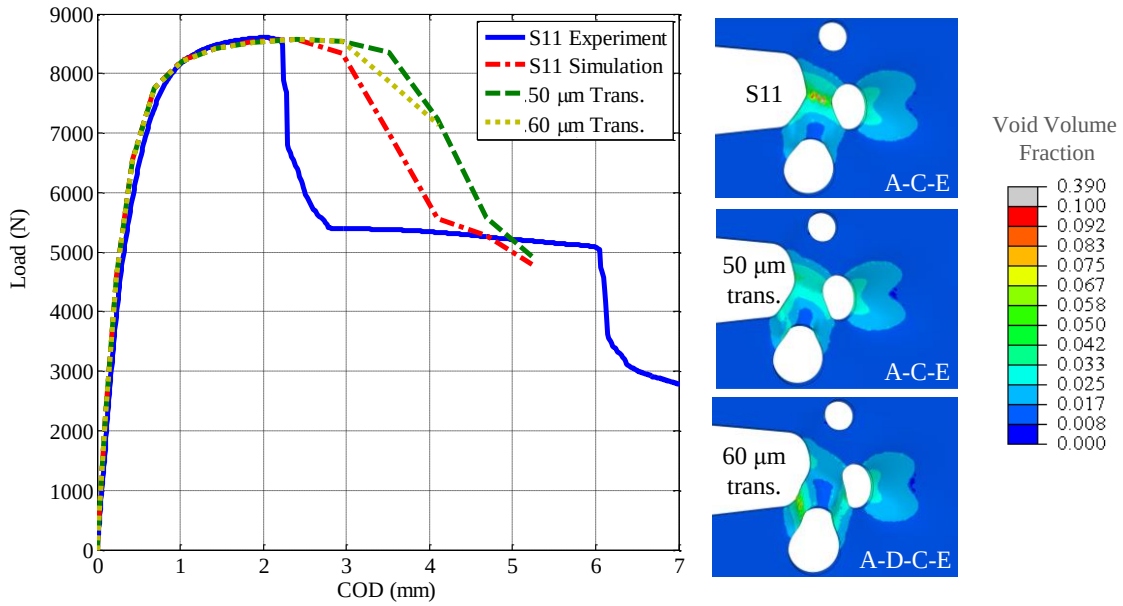

Figure 2.8: Experimental S11 load vs. COD profile, simulated S11 load vs. COD profile, simulated S11 with hole C translated down 50 µm load vs. COD profile, and simulated S11 with hole C translated down 60 µm load vs. COD profile, left. The contours of void volume fraction were taken at load = 5,528 N, 7,239 N, and 7,140 N for S11, S11 w/ 50 µm translation, and S11 w/ 60 µm translation, respectively, right.

2.5.5 Updating the Computational Model

When comparing experimental and numerical results in Sections 2.5.2-2.5.4, the first iteration of the framework did a poor job of capturing the immediacy of the first load drop. This is most evident for the S5 and S11 digital twin specimens which failed along A-D-C-E. Material points along the critical ligaments simply did not fail soon enough nor at a fast enough rate. It is well known that the Gurson model performs poorly in shear-dominated regimes. Specifically, it under-predicts damage under conditions of low stress triaxiality. Note that stress triaxiality is the ratio between hydrostatic and von Mises stresses. Nahshon *et al.* [60] proposed a modification to Gurson's model to compensate for the aforementioned limitation; specifically, they consider a two-term void evolution law wherein f is increased under shear deformation through the intercession of J_3, the third invariant or determinant of the deviatoric stress tensor.

Nahshon *et al*. [53] employed this modification to model fracture in the S5 specimen, and their prediction was considerably more accurate as a result.

Here, a more invasive approach was taken to compensate for the Gurson model's inability to evolve damage under low stress triaxiality. A user subroutine was employed to track stress triaxiality in real-time. When a material point had stress triaxiality greater than or equal to some value *t*, its yield surface parameters were set to q_1 = 1.5, q_2 = 1.0, and $q_3 = q_1^2 = 2.25$ (values commonly applied to steel in the literature). If a material point had a stress triaxiality lower than *t*, its q_2 was set to 2.0 to increase the second term in the yield condition given in Equation 2.2 (effectively inducing damage). This methodology was adopted from Chabanet *et al*. [61] who used it to model crack growth in aluminum sheets.

This scheme was implemented for the S5 digital twin specimen. The improvements made over the previous iteration's predictions were significant, suggesting that stress triaxiality should not be ignored when modeling challenge specimens that failed A-D-C-E. First, the damage rate in ligament A-D was accelerated. This caused a more immediate first load drop. Second, the first load drop was predicted to initiate at a much lower COD, in more agreement with measurements. Two load vs. COD profiles from this methodology are given in Figure 2.9. The shape of the predicted profiles beyond the first load drop was a marked improvement over the first iteration's; however, the ligament D-C still failed prematurely. This methodology is insufficient. In one regard, damage needs to be induced in order for the Gurson model to predict accurately the first load drop, but damage should not be allowed to evolve as quickly (with respect to load application) in ligament D-C as it did in this scheme. This motivates the use of a shear-modified Gurson model where damage is not induced as invasively as in this methodology.

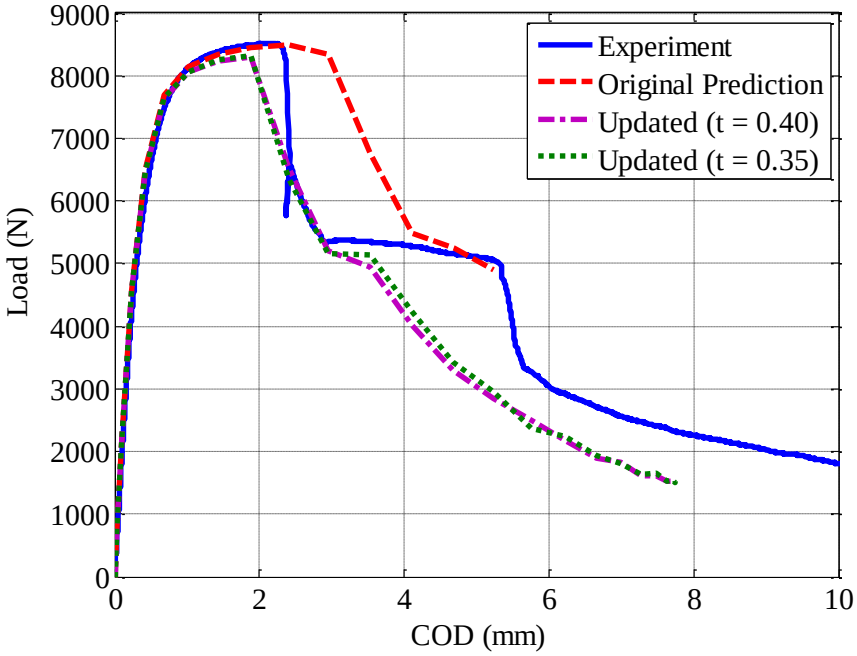

Figure 2.9: S5 Load vs. COD profiles from experiment and simulations with varying stress triaxiality thresholds, t.

2.6 Discussion

2.6.1 Overview

The modeling effort was divided into two phases. During the first phase, the computational model was created, verified, and used to make the aforementioned blind predictions. During the second phase, as-machined digital twin specimens were considered to resolve the crack-path ambiguity. Additionally, the model was updated to eliminate some prediction-related inaccuracies and a model discrepancy (an inherent, irreconcilable limitation of the model) was identified and bounded. The activities conducted during both phases, summarized in the spiral development model in Figure 2.10, mimic several of the procedures within Digital Twin, Figure 2.1. Note that cross-references to Figure 2.10 are made via braces, {}, hereafter.

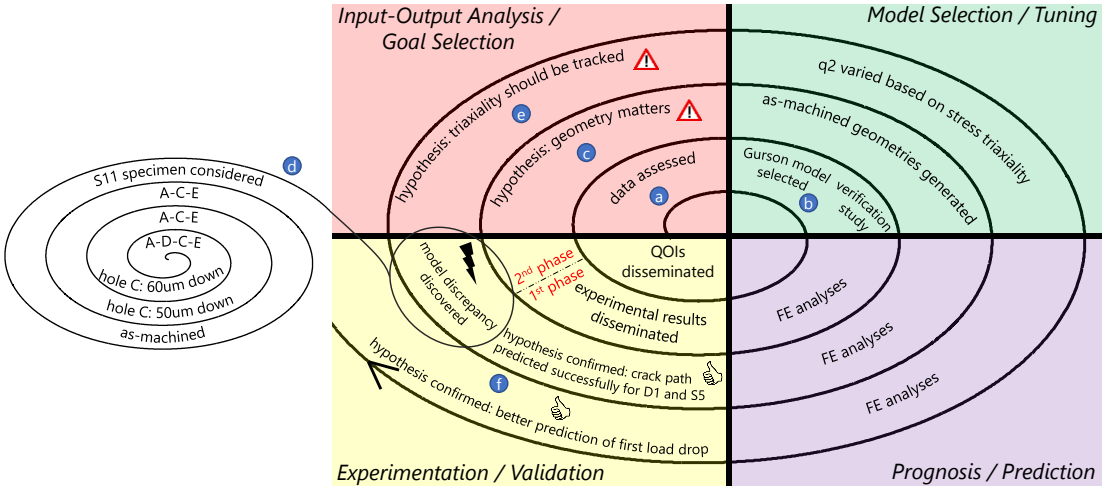

Figure 2.10: Spiral Development of Digital Twin Computational Model.

As discussed in Section 2.1, the two cornerstones of Digital Twin are VVUQ and personalization. Personalization featured prominently during the study— the consideration of as-machined challenge specimens was pivotal in resolving the crack path ambiguity. On the other hand, VVUQ-related procedures featured far less. In the next two sections, the modeling-related activities of the SFC presented herein are reconsidered in light of these procedures and Digital Twin as a whole.

2.6.2 VVUQ and the SFC

VVUQ is a set of procedures for determining the overall quality of a simulation activity [62]. The purpose of exercising the requisite procedures of VVUQ is to establish some control over the magnitude of uncertainty in the problem domain [47]. In the first phase of the SFC, only a few of the activities within VVUQ were performed to establish the framework detailed in Section 2.4 for the purpose of predicting fracture in the challenge specimen with nominal dimensions. In the second phase, the period after dissemination of the experimental results, more of the requisite procedures of VVUQ were performed to predict fracture in as-machined specimens. Given that VVUQ is an integral part of Digital Twin, it is illustrative to consider the activities of the first and second phases against the backdrop of VVUQ.

2.6.2.1 Modeling

At the onset of the first phase, two methodologies to predict fracture in the challenge specimen were considered. One was a microstructure-based modeling approach; however, due to lack of grain size, shape, and orientation distribution data, it was not pursued. The other was a Gurson model because there seemed to be a sufficient amount of data (i.e. uniaxial tension and fracture toughness) available for its calibration {a}. Also, the Gurson model was identified to have featured prominently in previous ductile fracture studies [63,64]. Moreover, given the time constraints of the challenge, the Gurson model, already implemented in Abaqus/Explicit, offered a relatively quick and simple means to estimate Sandia's QOIs. In hindsight, the decision to use the Gurson model {b} might have been premature as the model's shortcomings were never evaluated. It is well known that the Gurson model performs poorly for shear-dominated regimes unless modified [60]; however, no modifications were made. Additionally, some anisotropy was observed in the reported uniaxial tension test results, but the implementation in Abaqus/Explicit only accommodates linear isotropic elasticity, and thus anisotropy was ignored.

Having adopted the Gurson model, a geometric model of the challenge specimen was created based on the reported nominal dimensions. The geometry was meshed, the material calibrated, and loads were applied per Sandia's description. The loading was idealized as kinematic boundary conditions. Frictionless kinematic coupling constraints were assigned at the pin holes.

There were several sources of uncertainty in the model that should have been considered during the first phase. These included:

- Geometry: An engineering drawing of the challenge specimen with nominal tolerances was provided by Sandia. These tolerances were ignored as the framework was conditioned on a single nonrandom (nominal) geometry.

However, modeling a distribution of specimen geometries within the specified tolerance would not have been informative and the predicted crack path would have always been A-C-E. In other words, without modeling the as-manufactured geometry, accurate predictions could not have been made, further motivating the need for the Digital Twin framework.

- Loading Conditions: Sandia purposefully reported relatively vague information about loading conditions to mimic real world engineering problems. Clearly, this is a source of uncertainty, but no effort was made to characterize this uncertainty.
- Material Parameters: Sandia provided limited standardized experimental data on which to calibrate the Gurson model. Some of the model's parameters were able to be calibrated with these data; however, some could not be calibrated and thus were asserted.
- Physical QOIs: Physical QOIs were available only in the second phase, hampering validation efforts in the first phase. Even in the second phase, the physical QOIs were not uncertainty quantified.

At the beginning of the second phase, the issue of crack path ambiguity had finally come to the fore. This prompted the consideration of as-machined geometries {c}. Two results came from this exercise. First, the D1 and S5 crack paths were predicted accurately, but the predicted load vs. COD profiles exhibited considerable deviations from measurements. This was hypothesized to be the result of the Gurson model's limitations in shear-dominant regimes. Consequently, it was hypothesized that tracking stress triaxiality and inducing damage via the q_2 parameter {e} would produce more accurate predictions of the first load drop, and this indeed was the case {f}. Second, a model discrepancy was uncovered while analyzing the S11 specimen, and work was done to bound this discrepancy {d}. See Section 2.6.2.4 for more details on this topic.

2.6.2.2 Verification and Validation

A mesh refinement study was conducted to determine a characteristic element length (~200 μm) such that the crack path was insensitive to the discretization and subsequent refinement yielded negligible change in the solution.

As part of the computational model validation, a calibration of the Gurson model parameters was also conducted against tensile test and sharp-crack Mode-I fracture data provided by Sandia. There are four issues to consider with this validation activity. First, neither the tensile nor fracture toughness specimens had shear-mode damage. Consequently, shear failure was ignored during calibration. In hindsight, regardless of whether shear failure was initially hypothesized to occur or not, this omission handicapped calibration efforts. Second, only some of the Gurson model's parameters were able to be calibrated with the provided data. For example, yield surface parameters q_1 , q_2, and q_3 were all specified to be unity in the first phase as no data at the time were available to suggest otherwise. In the second phase, more appropriate values for 15-5 PH used in previous ductile-fracture-related studies [58,63] were considered, and the prediction of the first load drop was markedly better. Third, the variability in the calibration data provided was not quantified. Finally, the validation was incomplete in the first phase due to the lack of a physical QOI or a response metric for the challenge specimen.

2.6.2.3 Reduction in Uncertainty

There are two categories of uncertainty: epistemic and aleatoric. Epistemic uncertainty arises from sources where precise values could be incorporated if more accurate measurements could be made, but are generally not, in practice. Aleatoric uncertainty arises from unknown sources, which cannot be suppressed by more accurate measurement. Incorporating as-built geometry into the prognosis effort significantly reduced epistemic uncertainty. Moreover, updating the material model with additional

capability to predict damage more accurately for the initially unknown damage mode of the A-D-C-E crack path effectively reduced aleatoric uncertainty. An ultimate goal of Digital Twin should be to mitigate sources of epistemic uncertainty both before the vehicle is put into service, and during its life, while aleatoric uncertainty is reduced continually throughout the service life by accounting for phenomena that were not initially foreseen.

2.6.2.4 Prediction Accuracy and Model Discrepancy

Prior to being updated in the second phase, the computational model predicted peak load accurately but could not capture the immediacy of the first load drop in specimens that failed A-D-C-E. Material points along the critical ligaments simply did not fail soon enough nor at fast enough rates. To address this issue, the model was updated to induce damage at material points with low stress triaxiality, thereby compensating for the Gurson model's poor performance in shear-dominated regimes. The result was a markedly better prediction of the S5 specimen's first load drop.

The model was able to predict accurately crack paths for specimens machined to specifications and those exhibiting the highest deviations from specifications, but faltered for the S11 specimen which exhibited the subtlest deviations from specifications. This specimen closely resembled geometries that failed A-C-E, but cracked along A-D-C-E. The model predicted A-C-E— a model discrepancy that was later bounded to be only 60 μm in one specified dimension.

2.6.3 The SFC and Digital Twin

The SFC is a cautionary tale to the notion that modeling ductile fracture accurately in a non-standardized geometry can be done with nothing but a representative geometry, a seemingly well-calibrated constitutive model, and sound engineering judgment. The authors thought this was sufficient, but once the issue of crack path ambiguity came to the fore, it was evident that addressing Sandia's QOIs accurately would necessitate a

more detailed consideration of both the specimens' geometry and modes of failure. By applying Digital Twin concepts, the crack-path ambiguity diagnosis signaled a need to consider as-machined specimens. As-machined digital twin specimens were consequently implemented, predictions were made, and a second round of modeling was conducted to test the effectiveness of the computational model at determining the physical QOIs. Inaccurate predictions were somewhat remedied by compensating for the Gurson model's limitations under shear loading and a model discrepancy was unearthed and probed to determine its extent. Therefore, the second phase rested on the cornerstones of Digital Twin— more of the requisite activities of VVUQ were enacted and each specimen was personalized or modeled as-machined. The result was a significant reduction in both epistemic and aleatoric uncertainty and a markedly improved prediction of failure in the challenge specimens.

In the spirit of Digital Twin, the challenge specimen can be interpreted as a component. A fleet manager who procured several of these challenge specimen components, in this case Sandia National Labs, expected them to behave similarly to one another; however, when subjected to identical loading conditions, they clearly did not. Most exhibited an A-D-C-E crack path while others failed A-C-E. Those showing the same crack path exhibited a significant spread in their load vs. COD profiles. The term challenge specimen, therefore, is a misnomer. It connotes uniformity, but deviations in geometry resulting in disparate behavior clearly invalidate this suggestion. Consequently, the need to consider each challenge specimen as a part endowed with its own behavioral characteristics was essential in the SFC. Within the Digital Twin paradigm, components are not commoditized, they are personalized. This practice might seem excessive; however, as demonstrated in this paper, it is a necessary and feasible activity of Digital Twin.

2.7 Conclusions

Digital Twin is an admittedly immature paradigm that could potentially supplant current structural life maintenance and prediction practices. In its complete form, Digital Twin will require advanced high performance computing and unprecedented data management capabilities, but the over-the-counter computational framework employed herein demonstrates that even with limited time and computational resources, Digital Twin concepts can be relevant and effective.

The following can be concluded from the 2012 Sandia Fracture Challenge and the associated computational effort presented herein:

- The challenge specimen did not have a single representative geometry. Depending on the relative locations of the holes beyond the blunt notch, the challenge specimen was likely to fail along one of two possible paths.
- The computational model used during the first phase of the challenge was predicated on the challenge specimen with nominal dimensions (a geometry that never existed and one that was characteristic of only one failure path). Consequently, this model lacked the fidelity to resolve the crack path ambiguity.
- During the second phase of the challenge, as-machined, digital twin challenge specimens were considered, and the crack path ambiguity was able to be resolved for most configurations. Inaccurate predictions for specimens that failed A-D-C-E were the result of some inherent model discrepancy (bounded to be only 60 μm) and the Gurson model's limitations in shear-dominant regimes. The latter was partially remedied by inducing damage at material points with low stress triaxiality, an indication that shear failure was prevalent in specimens failing A-D-C-E.

These outcomes motivate the adoption of Digital Twin. Current structural life-management approaches lack the ability to forecast accurately structural health when

unexpected events occur. Moreover, they do not have the ability to function when heuristics are unavailable. As demonstrated in this paper, these limitations do not apply to Digital Twin. The unexpected issue of crack path ambiguity, for example, was addressed by generating digital replications of the as-machined specimens. Should this have proven inadequate, digital replications of microstructures could have been incorporated into the framework to compensate for the Gurson model's lack of fidelity. In fact, the 60 μm model discrepancy is strong evidence that microstructural-related fracture processes, which cannot be resolved by the Gurson model, are dominating at the bifurcation. For example, a nucleated microcrack at the blunt notch will first propagate at a rate and direction dictated by its local microstructural environment. Only when this crack becomes microstructurally large does its dependence on the microstructure wane; however, by this time, it could have propagated in the direction of one of the two observed crack paths to actually trigger it. This only further motivates the adoption of Digital Twin as current methods lack a comprehensive microstructural backbone.

2.8 Acknowledgements

The authors would like to acknowledge Dr. Brad Boyce of Sandia National Labs for spearheading the 2012 Sandia Fracture Challenge as well as all of its participants. Andrew Gross and Professor Ravi-Chandar of the University of Texas at Austin are also acknowledged for providing the experimental data of the S11 specimen that appear in this paper. Finally, Dr. Aida Nonn of Salzgitter Mannesmann Forschung GmbH is recognized for her assistance with the porous metal plasticity model.

Jacob Hochhalter would like to acknowledge support from the NASA Aeronautics Research Institute Seedling Fund which provided the necessary resources to complete the simulation work presented.

This research was made possible by support from the Ross-Tetelman Fellowship at Cornell University.

CHAPTER 3

DIGITAL TWIN AT THE MICROSCALE: IMPLEMENTATION AND VERIFICATION OF A MICROSTRUCTURE-BASED CAPABILITY FOR MODELING MICROCRACK NUCLEATION IN LSHR AT ROOM TEMPERATURE

If, when, and where a crack nucleates in a structure is largely dependent on the underlying microstructure— grain size, shape, and boundary character all dictate to some extent the nucleation of microcracks and their potential to propagate into life-limiting flaws. Structures are evaluated primarily on continuum plasticity, but its applicability ends at the microscale. For example, in Chapter 2 of this dissertation, a continuum plasticity damage model was shown to have a model discrepancy of approximately 100 μm or a few grain sizes. Some might argue that stochastics could be used to decrease this discrepancy; however, a probabilistic-based approach can only work if exhaustive work has been conducted down at the microscale to inform the probabilities up at the macroscale.

This type of work, which gives an indication of what Digital Twin might look like at the microscale, is carried out herein. Specifically, a microstructure-based capability for the purpose of forecasting microcrack nucleation in LSHR is proposed, implemented, verified, and partially validated. Gradient crystal plasticity is applied to Digital Twin (as-processed) finite element models of the experimentally measured, 3D microstructure wherein a microcrack is known to have nucleated along a coherent Σ3 boundary. The framework is used to analyze this particular nucleation event and conduct an extensive grain boundary analysis study, the results of which underpin the importance elastic anisotropy and coherency have in effecting the localization of irreversible plastic slip. In particular, grain boundary misorientation, type (i.e. Σ3 vs

non-Σ3), length, and inclination with respect to the loading axis are determined to be linked directly to the localization event. This framework could be coupled with the cohesive zone model detailed in Chapter 1 to account for both the microcrack nucleation mechanism in addition to microstructurally small propagation along grain boundaries.

3.1 Introduction

Nickel-based superalloys are known for their exceptional refractory properties, specifically high tensile strength and resistance to corrosion. Their use in gas turbines dates to the early 1940s with the Nimonic series of superalloys. Today, the Inconel family of superalloys and General Electric's damage tolerant superalloys like René88DT [65] feature prominently in this application. Recently, work has been conducted to understand and quantify these superalloys' microstructural failure mechanisms. For example, Mazur *et al*. [66] determined that microcracks in a turbine blade made of Inconel 738LC with 24,000 hours of service were correlated strongly to grain boundary brittleness and γ′ degradation. Findley and Saxena [67] determined that René88DT has two microcrack nucleation mechanisms when subjected to low-cycle fatigue (LCF) conditions at 650^{o}C. The first, cracking due to damage accumulation in persistent slip bands (PSBs), is prevalent at higher strain ranges and larger grain sizes. The second, cracking at subsurface clusters of inclusions, is prevalent in lower strain ranges and smaller grain sizes. Miao *et al*. [68], who also investigated René88DT, determined that under high-cycle fatigue (HCF) conditions (~20 kHz) at 593^{o}C, subsurface fatigue cracks initiate close to coherent twin boundaries in grains 3-5 times the average grain size with high Schmid factors.

It is obvious that grain boundaries, specifically twin boundaries, and γ′ play a central role in the nucleation of microcracks in nickel-based superalloys. Herein, the contribution of the former is considered in detail. Twin boundaries, coincidence site lattice (CSL) boundaries that are high angle, are referred to as strengtheners in the microstructure as they tend to prevent the transmission of dislocations [69]. Heavily twinned microstructures do not necessarily exhibit the classic Hall-Petch strengthening relation, and work has been done to quantify the twins' influence on the grain-size effect. Konopka and Wyrzykowski [70] developed a relation for yield stress based on the

frequency of twin (Σ3) boundaries that strongly or weakly oppose dislocation movement and those that act as dislocation sources. Pande *et al.* [71] modified the Hall-Petch relation by assuming all twin boundaries act as barriers to dislocation motion (in slight opposition to Li's [72] grain boundary strengthening arguments in which boundaries are assumed to emit dislocations) and incorporating an effective grain size term accounting for the presence of twin boundaries. Regardless of whether dislocations are prevented from transmitting across twin boundaries or are emitted from them, there is no question that dislocation pileup at twin boundaries poses severe consequences for the material's ability to resist microcrack nucleation.

It has been established that microcracks tend to nucleate at the twin boundaries of certain FCC materials such as copper [73,74] and nickel alloys [68,75]. Why are twin boundaries favorable sites for fatigue crack formation? Heinz and Neumann [76] argued that elastic anisotropy and coherency are decisive. First, high stress concentrations develop at the twin boundaries due to elastic anisotropy from the lattice mismatch. These high stresses, in turn, which can be estimated using the closed-form solution of Neumann [77], facilitate glide at the boundaries. It is noteworthy that these high incompatibility stresses do not produce additional shear stress on the boundary plane. Rather, a logarithmic stress singularity develops where the free surface and twin boundary trace meet. Second, alignment of the twin boundary and a slip plane (as with a coherent twin boundary) allows for dislocations to travel relatively long distances unhindered, causing high strains under such high incompatibility stresses. Several studies have been conducted which support these claims. Miao *et al.* [68], for example, observing René88DT under high cycle fatigue loading, found that microcracks tended to initiate close to coherent twin boundaries in large, high-Schmid factor (soft) grains. Stein *et al.* [75], investigating LSHR, also found that microcracks nucleated at coherent

Σ3 boundaries with larger than average chord lengths at the surface, but even in the absence of multiple, parallel twin-related lamellae.

The work presented herein is a follow-up to Stein *et al.*'s [78] investigation of microcrack nucleation and slip localization in the powder metallurgy disk alloy LSHR (low-solvus high-refractory). Therein, a microcrack was identified in a 3D orientation map of LSHR's microstructure that happened to nucleate and propagate along a coherent Σ3 boundary. This dataset from near-field high energy X-ray diffraction microscopy (nf-HEDM) measurements was analyzed with a fast Fourier transform-based method, the results of which indicate that both slip line length and resolved shear stress are correlated strongly with crack formation. Herein, the crystal-plastic finite-element method (CP-FEM) is used to shed more light on these results. This paper is divided into three parts. In the first, Section 3.2, the Digital Twin geometric model is established—the aforementioned dataset wherein a microcrack is known to have nucleated along a coherent Σ3 boundary. Additionally, LSHR's mechanical and microstructural properties are considered in detail. In the second part, Section 3.3, a gradient crystal plasticity model is proposed and calibrated to model LSHR's constitutive behavior. Finally, in Section 3.4, idealized models and reconstructions (both single- and multi-scale) are considered to verify and partially validate the framework's ability to accommodate a high degree of dislocation motion at Σ3 boundaries (especially coherent Σ3 boundaries). A grain boundary analysis study is also conducted to establish a correlation between grain boundary character and microcrack nucleation.

3.2 The Digital Twin Geometric Model: LSHR

3.2.1 Composition

The powder metallurgy disk alloy LSHR is a nickel-based superalloy noted for its exceptional tensile strength and creep resistance at high temperatures and versatile processing characteristics thanks to its low γ′ solvus. This face-centered cubic metal

was developed by NASA at Glenn Research Center and is used in the hot zones of gas turbine engines. Its composition is given in Table 3.1. For a detailed discussion on LSHR's thermal and mechanical properties, the reader is directed to Gabb *et al*. [79].

Table 3.1: Weight percent of LSHR's constituents (Ni balance). Adapted from [79].

Wt %	Al	B	C	Co	Cr	Fe	Mo	Nb	Ta	Ti	W	Zr
LSHR Comp.	3.46	0.028	0.029	20.7	12.52	0.07	2.73	1.45	1.6	3.5	4.33	0.049
γ phase	1.16	0.019	--	30.34	23.34	0.095	4.24	0.38	0.19	0.56	4.99	0.002
γ′ phase	5.48	--	--	12.27	1.99	0.02	1.1	2.49	3.02	6.36	3.59	0.094

3.2.2 Mechanical and Microstructural Properties

3.2.2.1 Constant-Displacement-Rate Tension Test

The Air Force Research Laboratory conducted a constant-displacement-rate tension test on a dog-bone specimen of LSHR, Figure 3.1, at ambient temperature [80]. Strain gages were applied to both fine and coarse grain regions as shown in Figure 3.1. With regards to the present work, the coarse grain region is of primary importance because the microcrack located in the nf-HEDM reconstruction occurred in a coarse grain zone with grain sizes on the order of 20 μm.

The stress vs. strain profile from the test is given in Figure 3.2. It is noteworthy that the yield stress of the fine grain region is approximately 10% higher than that in the coarse grain region. Moreover, neither curve exhibits classic three-stage hardening indicative of materials like LSHR with low stacking fault energies. One could argue that the small linear hardening observed is simply Stage I, but this behavior is typically seen in hexagonal close-packed lattices and not in FCC materials. Moreover, given the high frequency of high-angle (i.e. Σ3) boundaries in the microstructure, one would expect to see some spike in work-hardening rate, but again, this is not the case. It is apparent that multiple, competing strengthening mechanisms obfuscate the macroscopic response of LSHR.

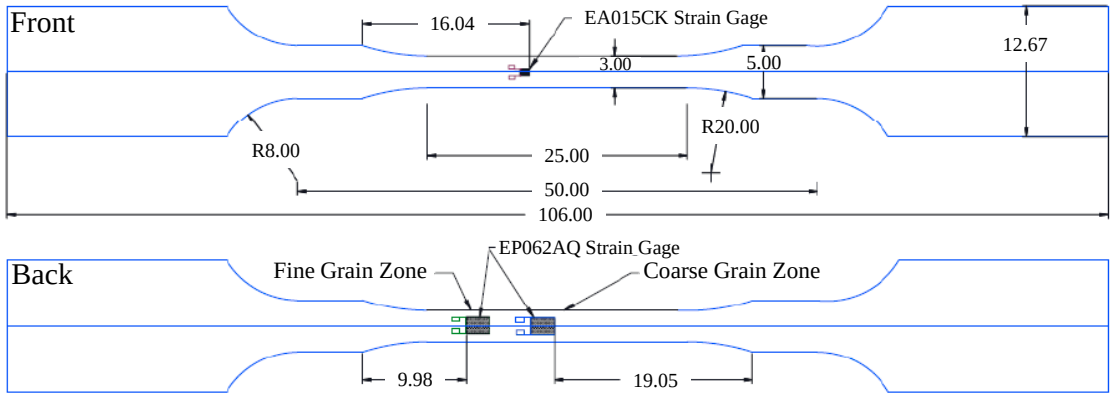

Figure 3.1: Dog-bone tension specimen of LSHR subjected to a constant-displacement-rate test. Figure adapted from [80]. Dimensions in millimeters.

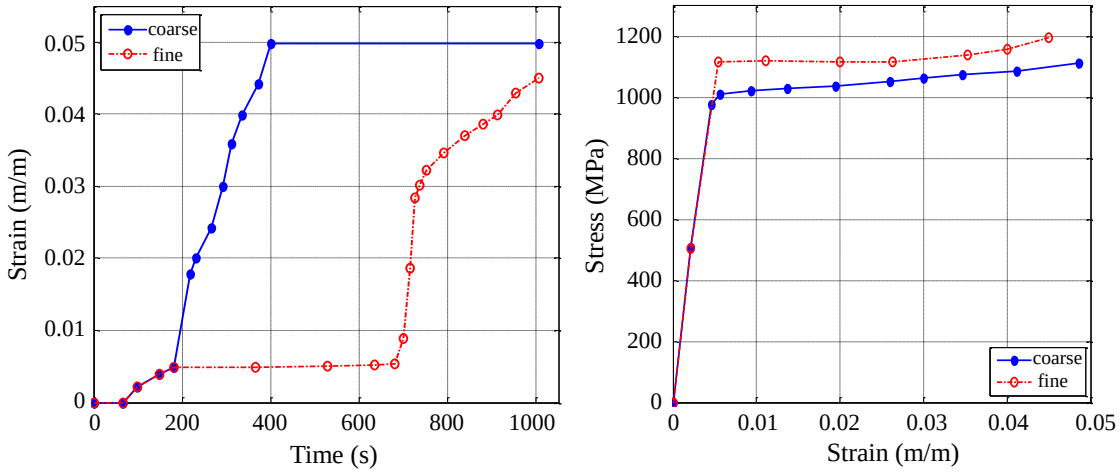

Figure 3.2: Strain vs. time profile (left) and stress vs. strain profile (right) from tension test for coarse and fine grain regions [80]. Note that strain did not evolve concurrently in the regions.

3.2.2.2 3D Nondestructive Orientation Mapping (nf-HEDM)

Researchers at Carnegie Mellon University conducted nf-HEDM measurements of LSHR at the Advanced Photon Source (APS) at Argonne National Laboratory. nf-HEDM is a rotating crystal method used to measure three-dimensional regions of polycrystals of millimeter dimensions with high-energy synchrotron sources. The product of this method is a nondestructive 3D orientation and spatial mapping of the microstructure. The following is a brief description of the collection and reconstruction process at sector 1 of the APS, but the reader is directed to Poulsen *et al*. [81] and Suter

et al. [82] for a more thorough discussion. First, a sample is loaded on a stage situated between a high-energy X-ray beam line focus source and a scintillator in front of a CCD camera lens used to capture diffraction from individual grains. The X-ray beam illuminates a complete cross-section of the sample as the stage rotates about the axis perpendicular to the incident beam. For each rotation, diffraction images are collected. The cross-sectional geometry is then later ascertained from the measured Bragg spots of each rotation. To determine the crystallographic orientations of the grains, an iterative forward modeling reconstruction procedure [83] is employed wherein the diffraction is simulated until a suitable fit is found between experimental and simulated scattering.

The effort is summarized in Figure 3.3 and detailed in Stein *et al*. [75]. First, a dog-bone tension specimen of LSHR was subjected to low cycle fatigue loading (σ_{max} = 1050 MPa, R = 0.05, N = 37,500, μ = 10 Hz) at room temperature. Next, replicas were made in the coarse-grain (~20 μm grain size) region of the specimen. Four microcracks were identified. Next, a portion of the specimen containing one of these microcracks (pictured in the SEM micrograph in Figure 3.3) was sectioned out with wire EDM and measured at the APS with nf-HEDM. Subsequently, the microstructure surrounding the microcrack was registered and reconstructed into a three-dimensional volume.

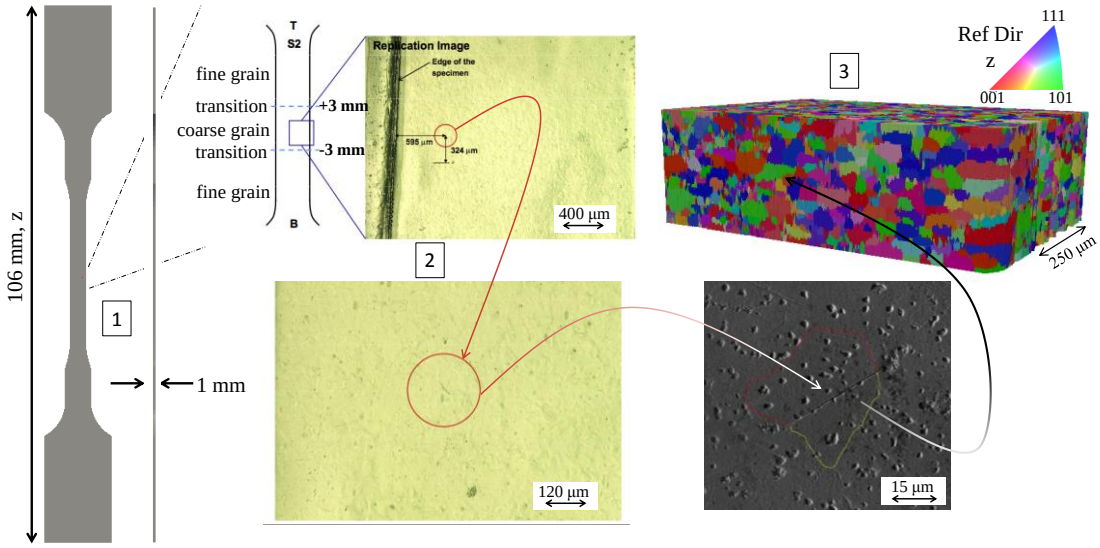

Figure 3.3: Overview of characterization effort. (1) A dog-bone tension specimen subjected to LCF loading at room temperature. (2) Replicas made in the coarse-grain region of the specimen. (3) Reconstruction from nf-HEDM containing microcrack identified in (2).

3.2.3 Microstructure

3.2.3.1 Overview

The reconstructed volume, Figure 3.4, has dimensions 525 x 760 x 240 µm and contains 20,756 grains. It was reconstructed with a resolution of 0.923 µm, 0.923 µm, and 4.0 µm in the x, y, and z, respectively. Its mean, minimum, and maximum grain size (measured as sphere-equivalent diameter) are 15.74 µm, 1.87 µm, and 67.05 µm, respectively. Although the grain size distribution exhibits deviations from lognormal in the upper tail, the parameters $\mu = 2.53$ µm and $\sigma = 0.74$ µm represent a lognormal best-fit. 90% of the grains have volumes less than 12,000 μm^3 and 50% have Schmid factors of 0.46 or higher.

Grain boundary character distribution (GBCD), an empirical distribution of the relative area of an interface with a given lattice misorientation and normal, is considered here to gauge the prevalence of coherent Σ3 boundaries in the reconstruction. Figure 3.5 gives a stereographic projection of the GBCD of the reconstruction against a 60^o

misorientation angle about a [1 1 1] rotation axis. It shows intensity centered at the [1 1 1] location which tapers off around it. This indicates that the microstructure has a relatively high frequency of coherent Σ3 boundaries, an expected result.

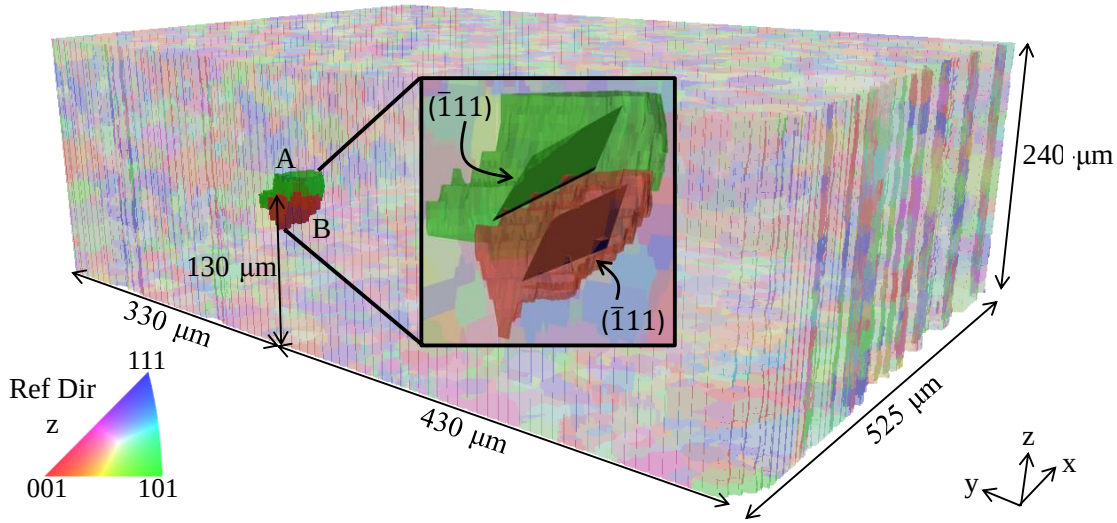

Figure 3.4: LSHR reconstruction with microcrack-participating grains A and B and their coherent (1̄11) planes. Loading was along the z-axis.

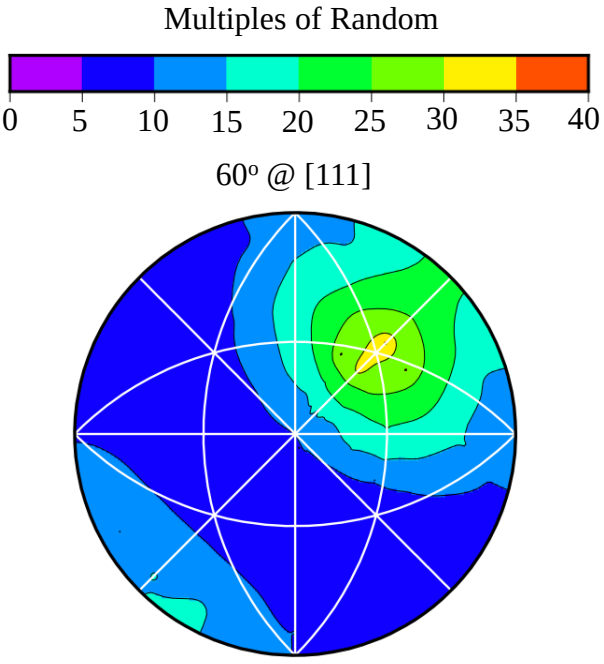

Figure 3.5: Stereographic projection of GBCD of the 20,756-grain nf-HEDM reconstruction.

3.2.3.2 Microcrack's Local Environment

The microcrack is located on the min-x surface of the reconstruction, lying along a coherent Σ3 boundary with a 59.27° disorientation about a [0.57 0.57 0.59] rotation axis, Figure 3.6. The coherent planes in both grains are $(\bar{1}11)$. The sphere-equivalent diameter, volume, Ω3 (a moment invariant measure of grain shape [84]), and Schmid factor of both grains and their nearest-neighbors are summarized in Table 3.2. It is noteworthy that compared to their nearest-neighbors, the microcrack-participating grains are considerably larger and softer.

Miao *et al*. [85], in their investigation of the nickel-based superalloy René88DT at room temperature under ultrasonic fatigue loading, determined that microcracks tended to initiate in surface grains that were (1) more than three-times the average grain size, (2) favorably oriented for slip localization, and (3) participated in Σ3 boundaries inclined to the loading axis. The smaller of the two microcrack-participating grains (denoted 'B' in Figure 3.4 and Figure 3.6) has sphere-equivalent diameter and volume that are 1.9-times and 2.6-times the average values of its ten nearest-neighbors, respectively. Moreover, this grain has a diameter and volume that are 1.9-times and 3.1-times higher than the average values of the total reconstruction, respectively. With regards to Miao *et al*.'s second and third criteria, the microcrack initiated approximately 100 nm away from a coherent Σ3 boundary with a surface trace inclined 68° to the loading axis. All three criteria are approximately met at the reconstruction's microcrack initiation site.

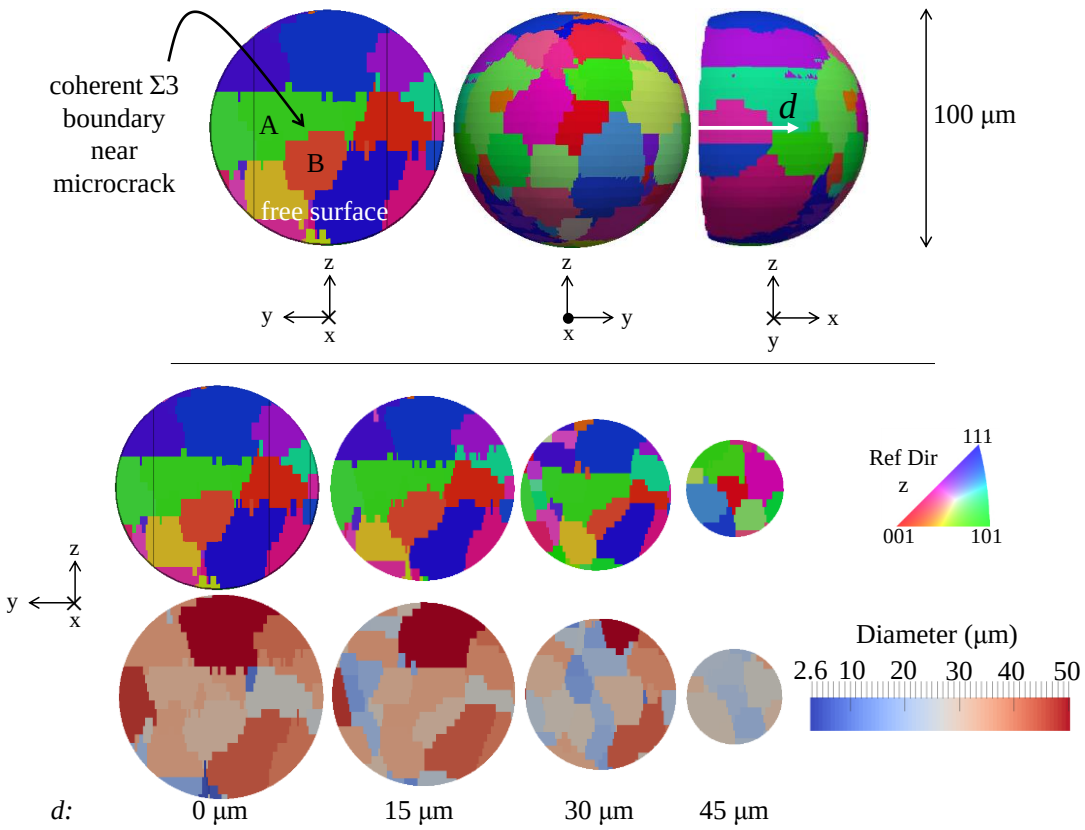

Figure 3.6: Nearest-neighbors of microcrack-participating grains within a 50 µm radius of Grain B's centroid.

Table 3.2: Diameter, volume, Ω3, and Schmid factor of microcrack-participating grains, nearest-neighbors, and total reconstruction.

Quantity of Interest	Grain A	Grain B	10 Nearest-Neighbors	25 Nearest-Neighbors	50 Nearest-Neighbors	Total Recon.
Diameter (µm)						
Value/Mean	34.7	30.4	15.8	17.0	15.9	15.7
Minimum	--	--	2.4	2.4	2.4	1.9
Maximum	--	--	34.7	43.7	50.2	67.1
Volume (µm^3)						
Value/Mean	21,90	14,600	5,530	6,610	6,510	4,690
Minimum	0	--	6.8	6.82	6.82	3.41
Maximum	--	--	21,900	43,800	66,400	158,000
	--					
Ω3						
Value/Mean	0.626	0.624	0.680	0.708	0.648	0.661
Minimum	--	--	0.0260	0.0260	0.0260	0.000850
Maximum	--	--	1	1	1	1
Schmid Factor						
Value/Mean	0.469	0.488	0.461	0.451	0.449	0.451
Minimum	--	--	0.354	0.343	0.313	0.275
Maximum	--	--	0.493	0.500	0.500	0.500

3.3 The Constitutive Model

3.3.1 Crystal Plasticity Model Formulation

The elasto-viscoplastic crystal plasticity model follows the formulation given by Matouš and Maniatty [86]. It is implemented for FCC with twelve octahedral, {1 1 1}, and six cubic, {1 1 0}, slip systems.

The elastic regime is governed by cubic elasticity. Let $\widehat{\boldsymbol{C}}$ denote the fourth order elasticity tensor in the relaxed configuration. The three elastic constants μ, λ, and η are given by:

$$\mu = C_{44} \tag{3.1}$$

$$\lambda = C_{12} \tag{3.2}$$

$$\eta = \frac{2C_{44} + C_{12} - C_{11}}{2} \tag{3.3}$$

The Green elastic strain in the relaxed configuration, $\widehat{\boldsymbol{E}^e}$, is given by:

$$\widehat{\boldsymbol{E}^e} = \frac{1}{2}\left(\boldsymbol{F}^{eT}\boldsymbol{F}^e - \boldsymbol{I}\right), \tag{3.4}$$

where $\boldsymbol{F}^e$ is the elastic deformation gradient and $\boldsymbol{I}$ is the second order identity tensor. The 2nd Piola-Kirchhoff Stress in the relaxed configuration, $\widehat{\boldsymbol{S}}$, in turn, is given by:

$$\widehat{\boldsymbol{S}} = 2\mu\widehat{\boldsymbol{E}^e} + \lambda\,\mathrm{tr}\left(\widehat{\boldsymbol{E}^e}\right)\boldsymbol{I} - 2\eta\boldsymbol{\epsilon}_{\widehat{\boldsymbol{ijkl}}}\colon\widehat{\boldsymbol{E}^e}\,, \tag{3.5}$$

where $\boldsymbol{\epsilon}_{\widehat{\boldsymbol{ijkl}}}$ evaluates to unity if $\hat{\imath} = \hat{\jmath} = \hat{k} = \hat{l}$ and zero otherwise. The resolved shear stress τ on slip system α is given by:

$$\tau^\alpha = \left(\boldsymbol{F}^{\boldsymbol{eT}}\boldsymbol{F}^{\boldsymbol{e}}\widehat{\boldsymbol{S}}\right)\colon\boldsymbol{P}^{\boldsymbol{\alpha}}\,, \tag{3.6}$$

where $\boldsymbol{P}^\alpha$ denotes the Schmid tensor. The slip rate along the slip systems is given by:

$$\dot{\gamma^\alpha} = \dot{\gamma_o}\frac{\tau^\alpha}{g^\alpha}\left|\frac{\tau^\alpha}{g^\alpha}\right|^{\frac{1}{m}-1}\,, \tag{3.7}$$

where $\dot{\gamma^\alpha}$ and $\dot{\gamma_o}$ are the shear and reference shear rates, respectively, m is a shear rate sensitivity parameter, and g the hardness. Hardness (resistance to slip) evolves according to a grain-size sensitivity term given by Beaudoin *et al*. [87] and a Voce-Kocks [88,89] relation, the first and second terms in Equation 3.8, respectively:

$$\dot{g^{\alpha}} = H_o \frac{\beta^2 \mu^2 b}{2(g^{\alpha} - g_o^{\alpha})} \sum_{\kappa=1}^{N_{ss}} \sqrt{\Delta_{iJ} n_{p_j} \Delta_{kL} n_{p_L}} |\dot{\gamma^{\kappa}}| + G_o \left(\frac{g_s^{\alpha} - g^{\alpha}}{g_s^{\alpha} - g_o^{\alpha}} \right) \sum_{\kappa=1}^{N_{ss}} |\dot{\gamma^{\kappa}}| \quad , \qquad (3.8)$$

H_o and G_o in Equation 3.8 are hardening coefficients, $\beta = 1/3$, b is the Burgers vector, $\boldsymbol{n_p}$ is the slip plane normal, and g_o and g_s are initial and saturation resolved shear strengths, respectively. The Δ variable in the first term of the hardness evolution is effectively a measure of dislocation density and is a function of the plastic deformation gradient:

$$\Delta_{iJ} = \epsilon_{JKL} F^p_{iL,K} \quad . \qquad (3.9)$$

GNDs localize to accommodate the heterogeneities that develop in plastic deformation [90]. The Δ term effectively accounts for this phenomenon by considering the gradient of the plastic deformation gradient, accommodating the evolution of slip close to these boundaries. It is noteworthy that the Voce-Kocks relation in Equation 3.8 is a slight departure from that given in the original formulation of the crystal plasticity model [86]. Here, latent and self-hardening effects are not assumed equal; consequently, the slip systems do not harden at the same rate. This is to allow the preference for slip on the twin-parallel systems discussed earlier.

3.3.2 Calibration

The gradient crystal plasticity model was calibrated for coarse-grain LSHR at room temperature. Both elastic and plastic regimes were considered in the calibration.

3.3.2.1 Stiffness Constants

To calculate the stiffness constants C_{11}, C_{12}, and C_{44} of LSHR, the rule of mixtures was employed to consider both the stiffness of pure nickel and Ni_3Al, Table 3.3. A γ' volume fraction of 0.40 was assumed.

Table 3.3: Stiffness constants of single crystal nickel [91], Ni_3Al [92], and LSHR at room temperature.

	C_{11} (GPa)	C_{12} (GPa)	C_{44} (GPa)
Pure Nickel	250.8	150.0	123.5
Ni_3Al	220.1	146.0	123.6
LSHR	238.5	148.4	123.5

The crystal plasticity model's elastic parameters are $\lambda = C_{12}$, $\mu = C_{44}$, η, and K. η proceeds from:

$$\eta = \frac{2C_{44} + C_{12} - C_{11}}{2} = 78.5 \text{ GPa} . \tag{3.10}$$

The bulk modulus, K, in turn, is given by:

$$K = C_{12} + \frac{2}{3} C_{44} = 231 \text{ GPa} . \tag{3.11}$$

3.3.2.2 Yield Strength

The yield strength of LSHR was determined by considering the yield strength of pure nickel and the following strengthening mechanisms: solid solution hardening of γ matrix, dislocation pinning, grain boundary strengthening, and particle strengthening.

The yield strength of pure nickel, σ_o, at room temperature is approximately 70 MPa [93]. The strengthening effect due to non-nickel constituents in the γ matrix, $\Delta\sigma_\gamma$, was determined using the following expression based on a model proposed by Gypen and Deruyttere [94]:

$$\Delta\sigma_\gamma = \left(\sum_i k_i^{\frac{1}{n}} c_i \right)^n \quad , \tag{3.12}$$

where c_i is the concentration of constituent *i*, k_i is the strengthening constant for constituent *i*, and *n* is taken to be 0.5 on the recommendation of Roth *et al*. [93]. Using solid-solution strengthening constants for alloying additions to the γ matrix in nickel [93] and the composition of γ given in Table 3.1, $\Delta\sigma_\gamma$ was calculated to be 361 MPa.

The strengthening increment due to the pinning of dislocations, $\Delta\sigma_d$, is given by:

$$\Delta\sigma_d = \alpha M \mu b \sqrt{\rho} \quad , \tag{3.13}$$

where α is a proportionality factor taken to be 0.2 for FCC metals, *M* the polycrystalline Taylor factor (=3 for FCC), μ the shear modulus, *b* the Burgers vector, and ρ dislocation density. Here, the Burgers vector of nickel was considered (352.4 pm). ρ, in turn, was assumed to be moderate at 10^{11} m^{-2}. Substituting values, $\Delta\sigma_d$ was calculated to be 5.85 MPa.

The strengthening increment due to grain boundary strengthening, $\Delta\sigma_{gb}$, was calculated using the Hall-Petch relation $k/\sqrt{d}$. *d*, the average grain size, was taken to be 15.7 μm from Table 3.2. *k*, the Hall-Petch constant, was assumed to be 750 MPa$\sqrt{\mu m}$ based on Kozar *et al.*'s [95] suggestion for IN100. Using these values, $\Delta\sigma_{gb}$ was calculated to be 189.3 MPa. Typically, strengthening due to grain-size hardening of the γ and γ′ phases are considered independently; however, because reliable Hall-Petch constants for both phases were unavailable, the grain-size strengthening contribution from each phase was integrated into a single measure.

The strengthening increment due to Orowan bowing, $\Delta\sigma_{OB}$, is given by:

$$\Delta\sigma_{OB} = \frac{\mu b}{L} \quad , \tag{3.14}$$

where *L is* the average spacing between γ′ particles, assumed to be 0.25 μm or approximately two-times the radius of the γ′ [79]. Substituting, $\Delta\sigma_{OB}$ was calculated to be 123.3 MPa. Reed states that the Orowan mechanism at room temperature is not the major contributor to strengthening in nickel alloys [96], and this calculation is consistent with this assertion.

The strengthening increment due to cutting of precipitates, $\Delta\sigma_c$, is estimated using the following equation given by Gleiter and Hornbogen [97] and detailed in Soboyejo [98]:

$$\Delta\sigma_c = \frac{0.28{\Gamma_{APB}}^{\frac{3}{2}} f^{\frac{1}{3}}}{b^2} \left(\frac{r}{\mu}\right)^{\frac{1}{2}} \quad , \tag{3.15}$$

where Γ_{APB} is the anti-phase boundary energy, r the particle radius, and f the particle volume fraction. For nickel-based superalloys, Baither *et al*. [99] suggests a Γ_{APB} in the range 230-270 mJ/m^2. Parthasarathy [100] used a Γ_{APB} of 260 mJ/m^2 to predict the yield strength of IN100 and René88DT with a spreadsheet model and established reasonable agreement with experiments. Consequently, this value was used. The particle radius and volume fraction were taken to be 0.10 μm [79] and 0.40, respectively. Substituting, $\Delta\sigma_c$ was calculated to be 235.4 MPa.

Schänzer and Nembach [101] considered the following superposition law in determining a yield strength for the nickel-based superalloy Nimonic 105:

$$\sigma_y^k = \sum_i \Delta\sigma_i^k \quad , \tag{3.16}$$

where k is a constant and i denotes the ith strengthening mechanism. They determined that k is dependent on γ′ volume fraction and age. For peak-aged and under-aged γ′, k = 1.13 and 1.19 produced best-fits with experimental data, respectively. Expanding and solving for σ_y:

$$\sigma_y = \left(\sigma_o^k + \Delta\sigma_\gamma^k + \Delta\sigma_d^k + \Delta\sigma_{gb}^k + \Delta\sigma_{OB}^k + \Delta\sigma_c^k\right)^{\frac{1}{k}}. \tag{3.17}$$

Substituting, σ_y = 830.0 MPa for k = 1.13 and σ_y = 777.8 MPa for k = 1.19.

Kozar *et al*. [95] assumed k = 1.0 primarily because evidence of strong superposition effects was lacking in IN100, their material of interest, but also because k > 1.0 tended to underestimate the yield strength. Assuming k = 1.0, σ_y = 984.9 MPa.

Comparing the computed critical resolved shear stress ($g_o = \sigma_y/M$) values, Table 3.4, LSHR's true g_o likely lies somewhere between 276.7 MPa (from k = 1.13) and 328.3 MPa (from k = 1.0); however, due to a lack of evidence suggesting strong superposition effects, g_o was taken to be 328.3-MPa in this study. According to Figure 3.2, coarse-grain LSHR yields at approximately 1,000 MPa. Dividing this value by M

yields a g_o of 333.3 MPa. This "back-of-the-envelope" calculation suggests that k = 1.0 is an appropriate choice.

Table 3.4: Predicted yield strength and critical resolved shear stress for range of k.

k	σ_y (MPa)	g_o (MPa)
1.00	984.9	328.3
1.13	830.0	276.7
1.19	777.8	259.3

3.3.2.3 Calibration Simulations

Crystal plasticity hardening parameters were tuned to yield a best-fit macroscopic response with the experimental data given in Section 3.2.2.1 The calibration model was a subset of the reconstruction and is considered in greater detail in Section 3.4.4. The model was cropped from around the cracked Σ3 boundary as shown in Figure 3.7(a). The model retained 169 Σ3 boundaries, some of which were coherent, Figure 3.7(b).

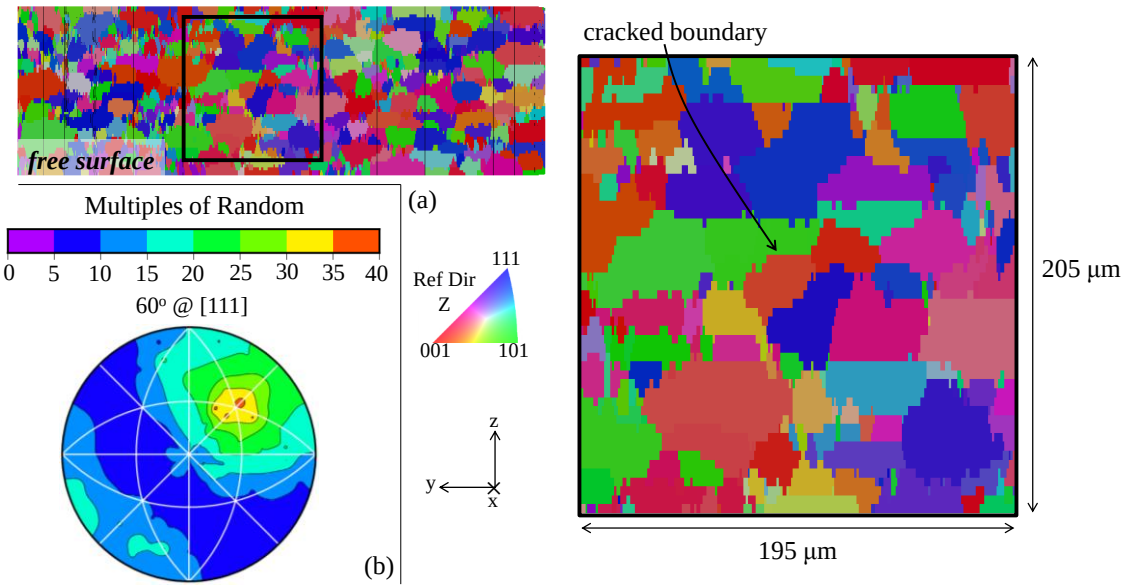

Figure 3.7: (a) Free surface of cropped model in context of uncropped free surface. The inverse pole figure colors given with respect to the z-axis reference direction. Cracked Σ3 boundary circled. (b) Stereographic projection of GBCD of the calibration model.

As discussed in Section 3.2.2.1, coarse-grain LSHR does not exhibit a high degree of work hardening. Given that LSHR has a relatively low stacking fault energy and high frequency of Σ3 boundaries, one would expect to observe the three stages of work hardening; however, this is not the case. It appears that multiple, competing hardening mechanisms are at play, namely dislocation annihilation and dislocation storage (i.e. GNDs). Typically, one can make sound judgments about which sets are physically viable; however, in this case, the competing mechanisms obfuscate the calibration process. Consequently, two sets of parameters are proposed for LSHR.

In the first set, dislocations are assumed to annihilate (Stage III) at some parts of the microstructure while at others (i.e. near high-angle boundaries) their motion is impeded resulting in an increase in dislocation density. The Voce-Kocks term with a relatively low saturation strength, g_s, effectively accounts for the annihilation of dislocations. The gradient term, in turn, "compensates" for Voce-Kock's decreasing work-hardening rate by inducing hardening in regions of high dislocation density. The net effect is a macroscopic response with small linear hardening. In the second set, the annihilation of dislocations is assumed to feature less prominently. The gradient term, in turn, is reduced significantly to prevent the microstructure from hardening excessively. See Table 3.5 for both sets' hardening parameters. The macroscopic response from both sets is given in Figure 3.8. The differences between the two stress-strain curves are minimal; however, at high strains, Set 1's curve shows an overall negative hardening rate while Set 2's shows positive (which is desirable for this application). Moreover, Set 2 replicates LSHR's rather immediate transition from elastic to Stage I hardening more accurately than Set 1.

Table 3.5: Calibrated crystal plasticity hardening parameters for LSHR at room temperature.

Set	m	$\dot{\gamma}_o$ (s^{-1})	G_o (MPa)	H_o (MPa)	g_o (MPa)	g_s (MPa)
1	0.034	1	591,800	400	328.3	340.0
2	0.048	1	400	400	328.3	380.5

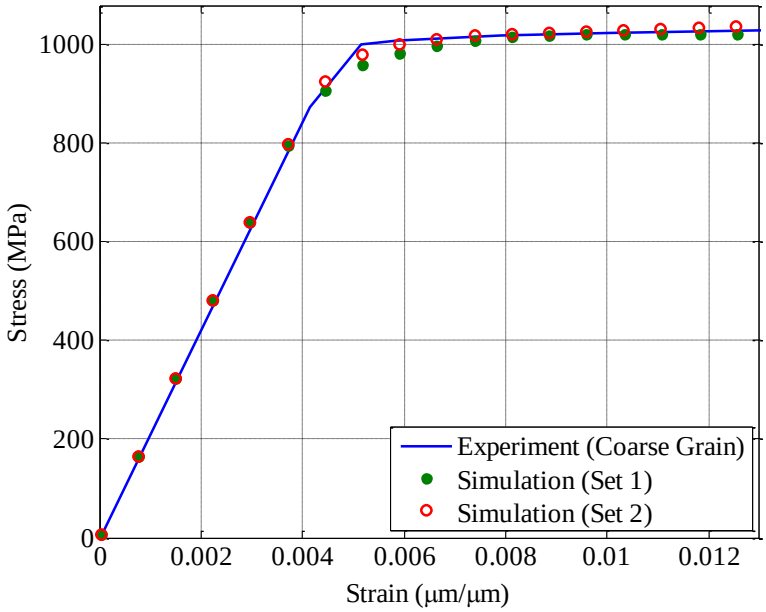

Figure 3.8: Experimental and simulated stress-strain curves of coarse-grain LSHR.

3.4 CP-FEM Simulations and Results

3.4.1 Microcrack Nucleation Metrics

Several metrics are considered for probing the likelihood of microcrack nucleation in LSHR, Table 3.6. The metrics considered here should not be viewed as definitive, indisputable indications of microcrack nucleation; in some cases, they contradict each other. Their ultimate utility is a probabilistic measure each accounting for geometric and/or physical factor(s) that affect crack initiation. In the context of this paper, they are used in a more local sense to parameterize LSHR's predominant microcrack nucleation mechanism. Thirteen metrics are considered: D_1-D_6 are slip-based, S_1-S_4 are stress-based, and metrics designated with an 'F' gauge the likelihood of slip transmission across grain boundaries.

D_1-D_3 are measures of accumulated slip on the most active slip system, the most active slip plane, and on all slip systems, respectively. D_4 is an energy-based measure which accounts for the energy dissipated due to slip on the most active slip plane. D_5 is the Fatemi-Socie parameter [102]— an augmentation of D_2 in which shear straining on the most active slip plane is scaled by the influence of normal stress on that plane, σ_n. The normal stress on the most active slip plane has been shown to play a key role in the nucleation of dislocations. For example, Tschopp and McDowell [103], investigating the nucleation of partial dislocations in single crystal copper, determined that nucleation was strongly correlated to large resolved normal stresses. D_6, finally, is a measure of dislocation density and proceeds from the gradient term in the hardness evolution, Equation 3.8.

Four stress-based metrics are considered. S_1 and S_2 are the maximum resolved shear stress on a single system and normal stress on the slip plane corresponding to S_1, respectively. S3, an augmentation of S_1 accounting for slip line length, is proposed by the authors as a means to inject grain size and coplanarity of slip planes with boundary planes into a single metric. If one considers that shear stress is the force driving microcrack nucleation, an admittedly gross simplification, then slip line length can be thought of as the distance over which this driving force can render its influence. Consequently, slip systems unimpeded by grain boundaries are favored whereas slip systems which are misaligned with boundary planes or are in relatively small grains are penalized. S_4, finally, can be thought of as the stress-based equivalent of the Fatemi-Socie parameter. It was proposed initially by Kirane and Ghosh [104] and is based on the notion of an effective traction used commonly in coupled cohesive zone models [105]. This metric is an effective stress on the most active slip system, the product of both shearing and tensile stresses.

Table 3.6: Microcrack Nucleation Metrics.

Metric	Description	Equation
D_1	The maximum accumulated slip on a single slip system.	$\max_{\alpha}\left(\int_0^t \lvert\dot{\gamma}^{\alpha}\rvert dt\right)$
D_2	The maximum accumulated slip on a single slip plane.	$\max_{p}\left(\sum_{\alpha=1}^{3}\left[\int_0^t \lvert\dot{\gamma}^{\alpha}\rvert dt\right]_p\right)$
D_3	The total accumulated slip.	$\sum_{\alpha=1}^{N_{SS}}\int_0^t \lvert\dot{\gamma}^{\alpha}\rvert dt$
D_4	Maximum energy dissipated due to slip on slip planes.	$\max_{p}\left(\int_0^t \sum_{\alpha=1}^{3}\lvert\dot{\gamma_p}^{\alpha}\tau_p^{\alpha}\rvert\, dt\right)$
D_5	The Fatemi-Socie parameter [102]. k is a fitting parameter taken to be 0.5. $\langle\cdot\rangle$ denotes the Macualay bracket.	$\max_{p}\left(\int_0^t \sum_{\alpha=1}^{3}\lvert\dot{\gamma_p}^{\alpha}\rvert\left(1+k\frac{\langle\sigma_n^p\rangle}{g_o}\right)dt\right)$
D_6	An indication of dislocation density.	$\sum_{\alpha=1}^{N_{SS}}\sqrt{\Delta_{iJ}m_j\Delta_{kL}m_L}\lvert\dot{\gamma}^{\alpha}\rvert$
S_1	The maximum resolved shear stress on a single slip system.	$\max_{\alpha}(\tau^{\alpha})$
S_2	The normal stress on plane of maximum shear stress.	$\langle\sigma_n^{\hat{\alpha}}\rangle$ where $\exists\,!\ \hat{\alpha}\ \max_{\alpha}(\tau^{\alpha})=\tau^{\hat{\alpha}}$
S_3	The maximum resolved shear stress on a single slip system multiplied by its associated slip-line length.	$\max_{\alpha}(\tau^{\alpha})\,L_{\hat{\alpha}}$ where $\exists\,!\ \hat{\alpha}\ \max_{\alpha}(\tau^{\alpha})=\tau^{\hat{\alpha}}$
S_4	The effective traction on the slip plane corresponding to the plane on which $\max_{\alpha}(\boldsymbol{\tau}^{\boldsymbol{\alpha}})$ acts. Adapted from Ruiz *et al*. [105].	$\sqrt{\langle\sigma_n^{\hat{\alpha}}\rangle^2+k\left[\max_{\alpha}(\tau^{\alpha})\right]^2}$ where $\exists\,!\ \hat{\alpha}\ \max_{\alpha}(\tau^{\alpha})=\tau^{\hat{\alpha}}$
F_1	A metric proposed by Simkin *et al*. [106] accounting for shear accommodation at the boundary.	$\max_{SS_1}\left(m_{SS_1}\lvert\boldsymbol{b}_{SS_1}\cdot\boldsymbol{t}\rvert\sum_{SS_2=1}^{N_{SS}}\lvert\boldsymbol{b}_{SS_1}\cdot\boldsymbol{b}_{SS_2}\rvert\right)$
$F_{complete}$	An augmentation of F1 proposed by Simkin *et al*. [106] that accounts for the alignment between the grain boundary with the shearing and loading directions.	$\max_{SS_1}\left(m_{SS_1}\lvert\boldsymbol{b}_{SS_1}\cdot\boldsymbol{n_{GB}}\rvert\lvert\boldsymbol{t}\cdot\boldsymbol{n_{GB}}\rvert\sum_{SS_2=1}^{N_{SS}}\lvert\boldsymbol{b}_{SS_1}\cdot\boldsymbol{b}_{SS_2}\rvert\right)$
F_{1spt}	An augmentation of F_1 proposed by Kumar *et al*. [107] that accounts for the coplanarity of the boundary plane with slip planes.	$\max_{SS_1}\left(m_{SS_1}\lvert\boldsymbol{b}_{SS_1}\cdot\boldsymbol{t}\rvert\sum_{SS_2=1}^{N_{SS}}\lvert\boldsymbol{b}_{SS_1}\cdot\boldsymbol{b}_{SS_2}\rvert\sum_{SS_2=1}^{N_{SP}}\lvert\boldsymbol{n}_{GB}\cdot\boldsymbol{n}_{SS_2}\rvert\right)$

Three slip-transmission metrics are considered. All three are measured at the interface between two grains (labeled 1 and 2 here). The first, F_1, is an adaptation from Simkin *et al*. [106]— a physically-based multiplicative expression including Schmid factor, relative magnitude of opening force acting on the boundary, and the relative accommodation of shear across the boundary. Specifically, $\left|\boldsymbol{b}_{SS_1} \cdot \boldsymbol{t}\right|$ is a measure of the alignment between the strain direction in grain 1, $\boldsymbol{b}_{SS_1}$, and the tensile direction, $\boldsymbol{t}$. $\sum_{SS_2=1}^{N_{SS}} \left|\boldsymbol{b}_{SS_1} \cdot \boldsymbol{b}_{SS_2}\right|$, in turn, is an indication of the alignment of shearing planes across the grain boundary; Simkin *et al*. [106] found that high amounts of shear accommodation across twin boundaries (where the summation is large) were often associated with a microcrack nucleation event. Of course, the F_1 metric does not consider the orientation of the boundary plane itself. Enter the $F_{complete}$ and F_{1spt} metrics. $F_{complete}$ is an augmentation of F_1 that accounts for the alignment between the grain boundary with the shearing and loading directions. F_{1spt}, proposed by Kumar *et al*. [107], is also an augmentation of F_1 that accounts for the coplanarity of a grain's slip planes with the boundary plane. This accommodation is made by summing the absolute values of the scalar products of the grain boundary normal, $\boldsymbol{n}_{\boldsymbol{GB}}$, and slip plane normal.

3.4.2 Verification: Baseline Model

A relatively simple, idealized finite element model of a twin lamella and its containing grain was generated for the purpose of probing the crystal plasticity model's ability to accommodate slip on twin-parallel systems. The twin and its containing grain were surrounded by a cubical grain for load-transfer purposes, Figure 3.9.

Finite Element All-Wheel Drive (FEAWD) [22] was used to drive the crystal-plastic finite-element simulations in this section and the sections proceeding. FEAWD is built on MPI, FemLib (a library of constitutive models and finite elements), Boost, the BLAS and LAPACK, PETSc, ParMETIS, and HDF5. Raw finite element output was converted into XDMF data structures for visualization in ParaView.

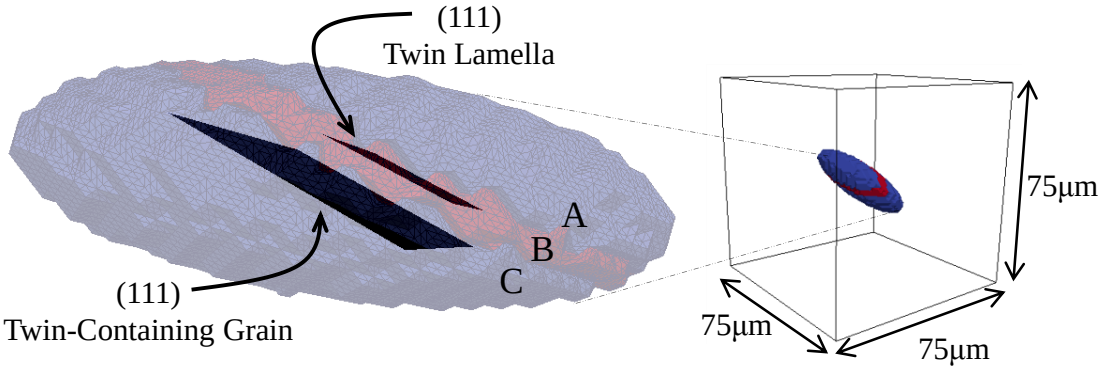

Figure 3.9: The baseline model showing alignment of the (111) slip planes of the twin lamella and twin-containing grain with the twin boundaries, rendering coherent twin boundaries.

A baseline model with coherent twin boundaries was considered first, Figure 3.10(a). It is apparent that slip evolved from the lamella's edges inward. Moreover, approximately 80% of total slip on the twelve octahedral slip systems was on the twin-parallel systems. A baseline model without the twin lamella was considered next to gauge the crystal plasticity model's ability to accommodate slip on twin-parallel systems without long, slender twin morphologies. Here, the twin lamella, labeled B in Figure 3.9, was merged into half of the twin-containing grain, region C, leaving a coherent Σ3 boundary between grains BC and A. Figure 3.10(b) shows the evolution of slip in grain A. Approximately 75% of total slip on the octahedral slip systems was on the boundary-parallel systems. For these simulations, it is noteworthy that the highest localizations of slip occurred at the coherent boundaries. One could extend this observation to the idea of hotspots and the identification of potential microcrack nucleation sites [108].

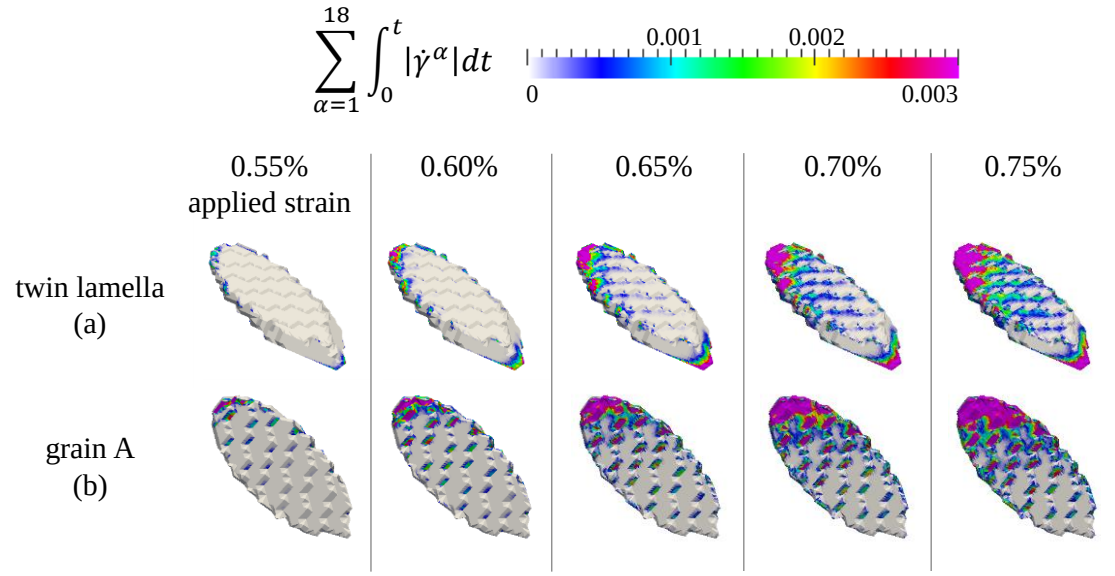

Figure 3.10: Evolution of slip along coherent Σ3 boundary in baseline model with twin lamella (a) and without (b). Metric D_3 considered here.

Next, incoherent Σ3 boundaries were considered. To establish the incoherent boundaries, Table 3.7, once-coherent (111) planes on either side of the boundary were rotated progressively out-of-phase with the boundary plane (with angle θ) while preserving the Σ3 condition. Results are summarized in Figure 3.11. In general, as the once-coherent planes became increasingly misaligned with the boundary plane, the extent and magnitude of total slip on the boundary decreased. It is noteworthy that slip along the boundary was primarily exclusive to the $(111)[0\bar{1}1]$ slip system in both the coherent and 1.4°-incoherency models. Obviously, as the (111) planes became increasingly misaligned with the boundary plane, slip began to accumulate on $(\bar{1}11)$, $(1\bar{1}1)$, and $(11\bar{1})$ planes. For example, in the 20.8°-incoherency model, the majority of slip accumulated on $(\bar{1}11)$ and $(1\bar{1}1)$ planes. As shown in Table 3.7, all of the boundaries considered had at least one slip plane that was moderately coplanar with the boundary plane.

Table 3.7: Details of Σ3 boundaries considered in baseline study.

Grain A (ϕ_1, Φ, ϕ_2) **(deg)**	**Grain BC** (ϕ_1, Φ, ϕ_2) **(deg)**	θ **(deg)**	$\max_{SS_1}(\lvert n_{GB} \cdot n_{SS_A} \rvert)$	$\sum_{SS_1=1}^{N_{SP}} \lvert n_{GB} \cdot n_{SS_A} \rvert$
25.3, 23.7, 347.2	229.2, 25.7, 103.7	---	0.94	1.91
33.1, 29.6, 343.2	235.8, 19.5, 101.4	1.4	0.93	1.91
229.9, 37.0, 108.6	197.4, 77.6, 90.8	11.4	0.88	1.92
142.1, 119.6, 51.4	94.0, 101.2, 356.6	20.8	0.85	1.88

Intuitively, these results are expected— the amount of accumulated slip at small strains is largely dependent on the degree of misalignment of slip planes with the boundary plane. What these results do not suggest, however, is how slip accumulates along incoherent Σ3 boundaries at high strains. This motivates the consideration of the gradient term in Equation 3.8. The gradient term, a function of the plastic deformation gradient, is effectively a measure of dislocation density. When this gradient is high (i.e. at high strains along high-angle boundaries), the term induces hardening and increased resolved shear stresses. This invariably leads to increased slip rates, Equation 3.7, and higher accumulations of slip.

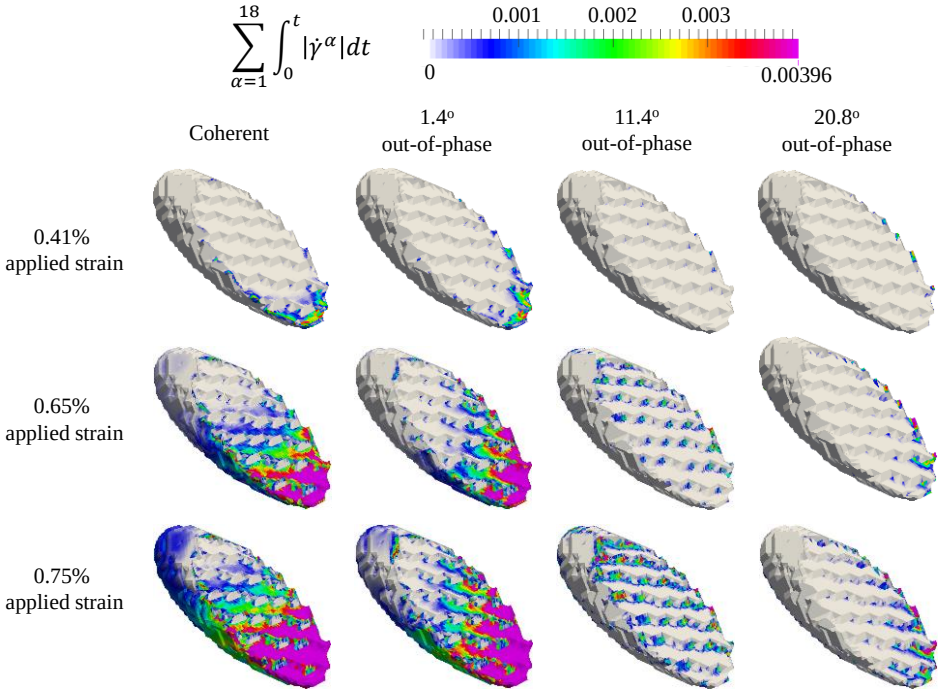

Figure 3.11: Evolution of slip along Σ3 boundary in baseline model without twin lamella for varying degrees of incoherency. Viewing boundary on side of Grain BC. Metric D_3 considered.

The influence of this term was investigated in the baseline model with the D_6 metric, the product of dislocation density and slip rate, Figure 3.12. Intuitively, one would expect this term to feature more prominently along incoherent boundaries as slip planes incident along the boundary plane would produce higher dislocation densities than boundary-parallel planes, and this indeed was the case. The gradient hardening term, therefore, has the unique ability in the framework to accentuate hotspots at incoherent Σ3 boundaries.

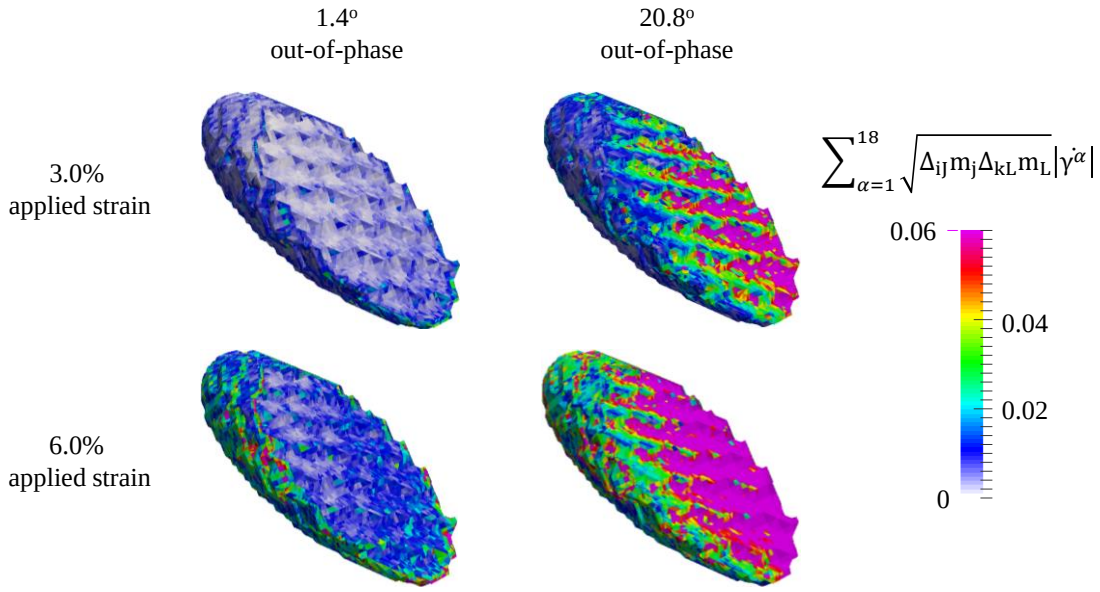

Figure 3.12: Indication of dislocation density along Σ3 boundary. Viewing boundary on side of Grain BC. Metric D6 considered here.

3.4.3 Validation: Proof-of-Concept Multiscale Model

3.4.3.1 Assembling the Model

The nf-HEDM reconstruction was initially in the form of point-cloud data with an orientation assigned to each point. DREAM.3D was used to geometrize the reconstruction. The 20,756-grain measured dataset's native 0.923 x 0.923 x 4 μm resolution was modified to 6 x 6 x 6 μm, effectively stripping away voxels that would otherwise make for a computationally intractable discretization. Next, any grain that was not composed of at least 20 voxels was merged into its neighbors. The resulting

model consisted of 2,478 grains, contained a relatively high frequency of coherent Σ3 boundaries, and was positioned into a geometrically-exact representation of the tensile specimen, Figure 3.13.

The tensile specimen's geometry, Figure 3.1, was created in Abaqus/CAE [56]. Conformity between the tensile specimen and microstructure was achieved by transitioning the non-uniform microstructural surface mesh to a structured arrangement of triangular faces with VTK's Delaunay triangulation implementation. A surface mesh of the tensile specimen was then merged with this arrangement and subsequently volume meshed with Abaqus/CAE's tetrahedral mesh generator. The Parallelized Polycrystal Mesher [109] was used to volume mesh each grain with tetrahedral elements. This software is built on a meshing algorithm given by Cavalcante *et al*. [110,111] as well as Abaqus/CAE's tetrahedral meshing capabilities. The volume meshes of both the microstructure and tensile specimen were then merged into a single volume mesh.

The tensile specimen was modeled with a von Mises plasticity model with linear kinematic hardening. The grains were modeled as crystal plastic with the model developed in Section 3.3. The tensile specimen was loaded monotonically with kinematic boundary conditions at the ends to mimic the loading conditions of the actual test.

3.4.3.2 Results and Observations

The slip transmission metrics calculated on the free surface are shown in Figure 3.14. It is noteworthy that only one of the metrics, $F_{complete}$, is particularly high at the cracked boundary. Recall that $F_{complete}$ is a multiplicative expression accounting for the alignment between the grain boundary with the shearing and loading directions. F_{1spt} is high at only portions of the boundary aligned with the coherent $(\bar{1}11)$ slip planes on either side. F_1, in turn, suggests that a considerable amount of shear accommodation is

being made at the cracked boundary, but also at others in the immediate vicinity. Consequently, further analysis is needed to explain why a microcrack nucleated at this particular boundary.

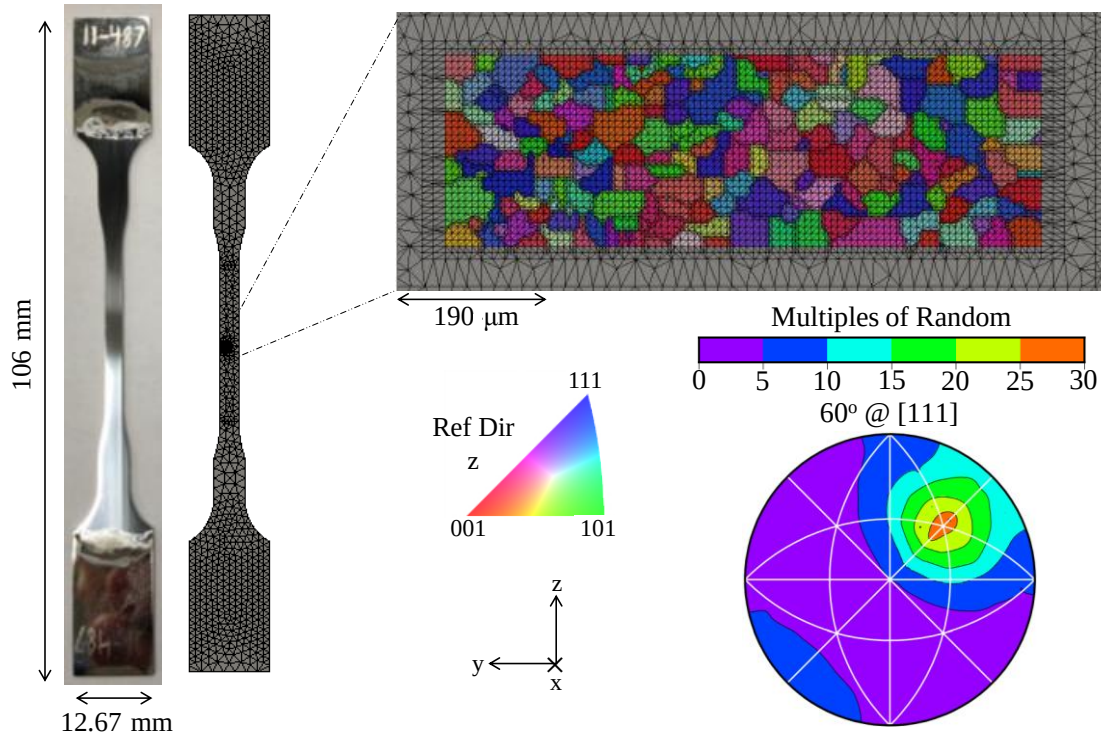

Figure 3.13: RVE of reconstruction merged into mesh of tensile specimen. A high frequency of coherent Σ3 boundaries were maintained in the RVE as conveyed by the stereographic projection of GBCD.

The tensile specimen (with embedded microstructure) was simulated up to 1.0% applied strain. At 0.15% strain, irreversible plastic slip began to accumulate on the free surface. Interestingly, this localization occurred exclusively in the grain dubbed "Grain B" in Section 3.2.2.2 along the cracked coherent Σ3 boundary. By 0.20% strain, the free surface was saturated with accumulated slip, but the highest localization was maintained in Grain B, Figure 3.15. It is noteworthy that 90% of the slip near the coherent Σ3 boundary in Grain B accumulated on the coherent planes, behavior seen in the baseline study discussed (Section 3.4.2) and observed by Miao *et al.* [68] in René88DT. The two largest hotspots on the free surface occurred approximately 50 µm

away from each other. They localized along high-angle grain boundaries in soft (low-Taylor, high-Schmid) grains, Figure 3.16. At the low strains considered here, it is obvious that these hotspots were primarily the product of elastic anisotropy and secondarily the product of dislocation storage; however, the relatively high dislocation density at these hotspots suggests that at higher strains, gradient plasticity will accentuate them.

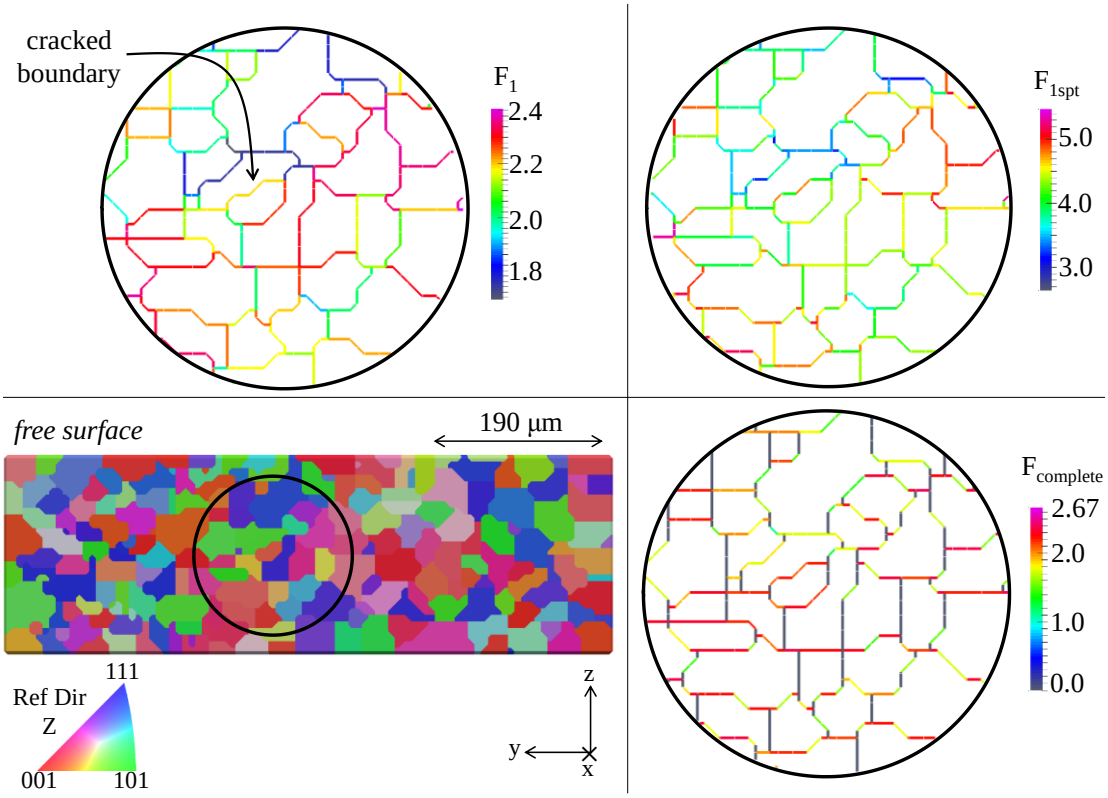

Figure 3.14: Slip-transmission metrics on the free surface of the proof-of-concept model.

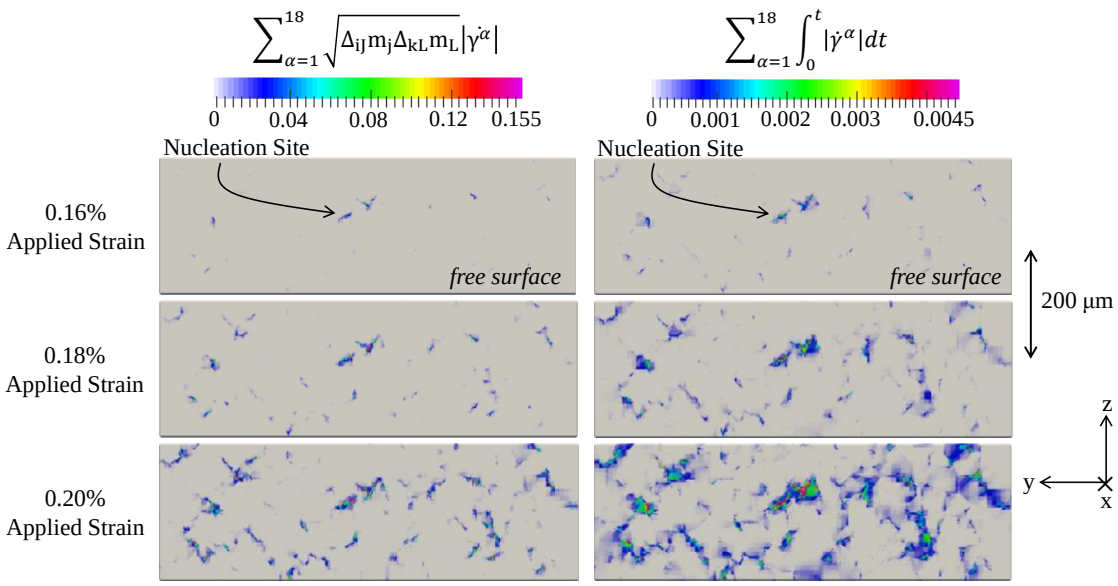

Figure 3.15: Evolution of dislocation density, D_6, left, and total accumulated slip, D_3, right, on the free surface of the proof-of-concept model. Note that the highest localization of slip occurs along the cracked coherent Σ3 boundary identified in Section 3.2.3.2.

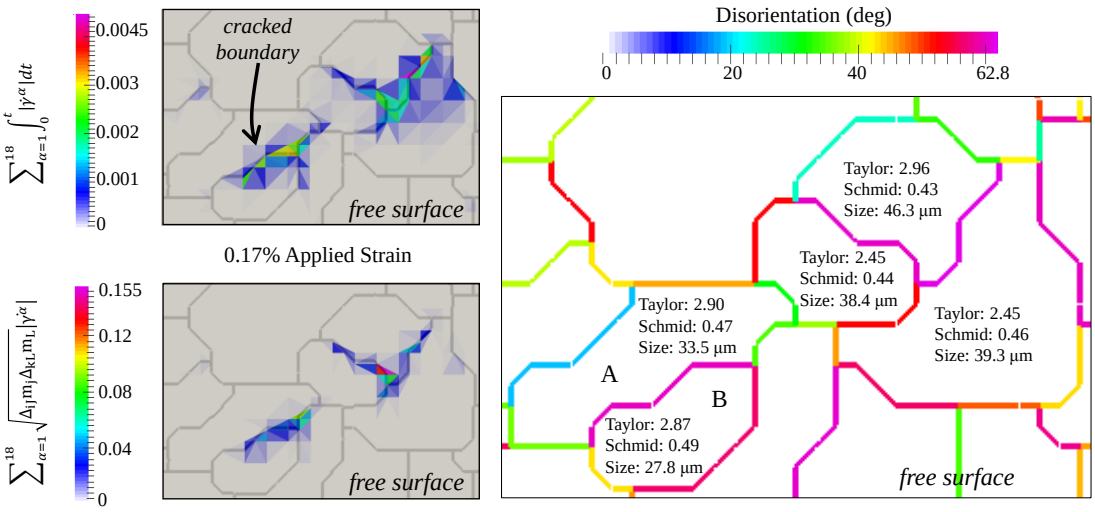

Figure 3.16: Total accumulated slip, D_3, and dislocation density, D_6, left, and disorientation, Taylor and Schmid factors, and grain size, right, around cracked coherent Σ3 boundary on the free surface of the proof-of-concept model. Note that the hotspots highlighted here are along high-angle grain boundaries in relatively soft grains.

Referring to Figure 3.17, contour plots of the stress- and slip-based metrics on the free surface of the proof-of-concept model at 0.21% applied strain, it is evident that D_1-D_6 are exceptionally high at the cracked boundary. The D_3 contour is virtually identical

to the D_2 contour which suggests that secondary slip is insignificant at this applied strain. The D_5 metric, in turn, is particularly high which indicates that the resolved normal stress (S_2) on the coherent planes is relatively high. The S_3 metric is not exceptionally high at the cracked boundary, but is well above the mean. It is noteworthy that the highest values of the S_3 metric are exclusive to large grains (regardless of coplanarity of their slip planes with their boundaries). The S_4 metric, finally, like the S_3 metric, is not particularly high at the cracked boundary. Given the S_4 metric's similarity to the Fatemi-Socie metric (S_5), and given that S_5 localized at the cracked boundary, it is fair to say that some of the stress-based metrics, at least in this case, fail to explain why a microcrack nucleated at the cracked boundary.

Aside from the hotspots identified in Figure 3.16, five more localizations of total accumulated slip were found in the microstructure at 0.17% strain, Table 3.8. Each of these localizations occurred close to highly disoriented boundaries (>20^o). Moreover, in all cases, hotspot-containing grains were found to have a {111} slip plane aligned with the boundary where the slip localized. Additionally, the hotspot-containing grains typically had grain sizes higher than the mean (39.8 μm). Finally, hotspot-containing grains were considerably soft based on their relatively high Schmid and low Taylor factors.

3.4.4 Grain Boundary Analysis: Cropped Reconstruction Model

3.4.4.1 Overview

The reconstruction was cropped around the cracked Σ3 boundary, Figure 3.7, and meshed into a 86 x 195 x 204 μm volume with 47 million degrees-of-freedom. It was generated in its native resolution without merging smaller grains into their larger neighbors, a departure from Section 3.4.3. Consequently, the measured grain morphologies are preserved in this model. It retains 936 grains and 4,492 grain boundaries (169 of which are Σ3 boundaries) from the uncropped reconstruction.

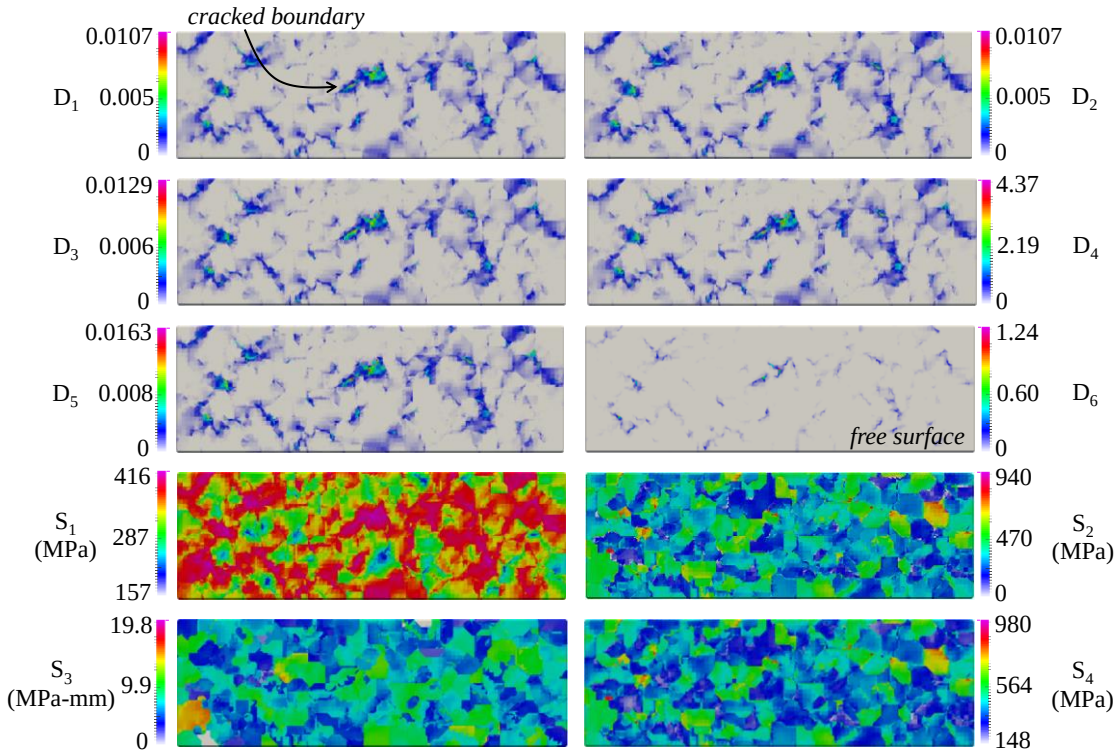

Figure 3.17: Slip and stress-based metrics on the free surface of the proof-of-concept model at 0.21% applied strain.

Save for the min-x face (the free surface), kinematic boundary conditions were applied to all faces of the cropped reconstruction: the max-x, min-y, max-y and min-z faces were constrained to in-plane motion and the max-z face was displaced in the positive-z direction. These boundary conditions mimic the loading on the proof-of-concept microstructure— simple tension with Poisson's effect constrained in two dimensions.

As shown in Figure 3.18, slip localized at the cracked boundary. As in the proof-of-concept microstructure, a significant localization of slip occurred only 50 μm away along a relatively long Σ3 boundary. In fact, some of the highest accumulations of slip on the free surface of the uncropped model localized along Σ3 boundaries. The same can be said for the maximum resolved shear stress on a single slip system (S_1). From Figure 3.18 alone, one could assume that in LSHR specifically, the general character of

a grain boundary dictates if slip has the potential to localize along its length; however, what specifically controls this process? It is already apparent that CSL boundaries dictate the localization phenomenon to some degree, but other factors ostensibly are present. This motivates a thorough grain boundary analysis of the reconstruction.

Conducting an accurate grain boundary study is contingent upon calculating accurately the normal of each boundary. This would be impossible without having LSHR's actual grain morphology, a benefit of this Digital Twin framework. To conduct this analysis, a topology-based data structure was created for each of the 4,492 grain boundaries in the cropped reconstruction. Next, Equation 3.18 was used to calculate the normal, $\boldsymbol{n}_{GB}$, of each boundary:

$$\boldsymbol{n}_{GB} = \frac{\sum_{f=1}^{N_{facets}} \boldsymbol{n}_f}{\left|\sum_{f=1}^{N_{facets}} \boldsymbol{n}_f\right|} \quad , \tag{3.18}$$

where $\boldsymbol{n}_f$ is the normal of facet *f*. Having an accurate grain boundary normal is critical to orienting the boundary in 3D space. Gauging slip plane coplanarity and the boundary's inclination with respect to the loading axis would be impossible without one.

Having oriented each grain boundary in 3D space, parameters thought to participate in slip localization were mapped to each boundary. Some of these parameters included misorientation, boundary type (i.e. Σ3 vs. non-Σ3), and the Schmid factors and grain sizes of the boundary's adjacent grains.

Table 3.8: Hardness and size of hotspot-participating grains. Coherent planes demarcated. Hotspot-containing grain transparent. Total accumulated slip, $\sum_{\alpha=1}^{N_{ss}} \int_0^t |\dot{\gamma}^\alpha| dt$, D_3, contours.

Hotspot Participating Grains	Schmid Factor	Taylor Factor	Diameter (μm)	Disorientation
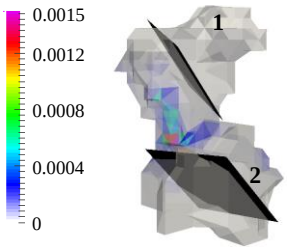	1: 0.45 2: 0.50	3.52 3.28	38.0 36.9	50.2°
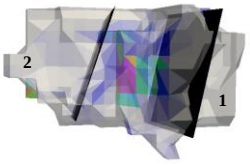	1: 0.40 2: 0.48	3.47 3.58	41.3 39.8	46.2°
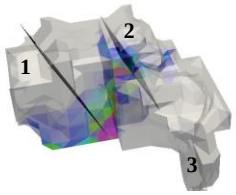	1: 0.42 2: 0.49 3: 48.4	2.93 3.24 3.15	44.1 40.8 34.6	1-2: 57.3° 1-3: 51.5° 2-3: 35.7°
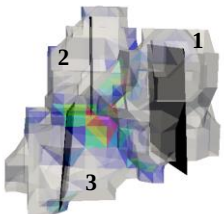	1: 0.46 2: 0.48 3: 0.44	3.64 3.32 3.61	44.2 37.9 38.2	1-2: 23.0° 1-3: 38.3° 2-3: 16.2°
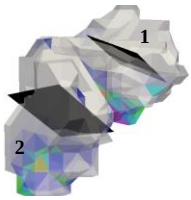	1: 0.49 2: 0.49	2.75 3.07	32.2 44.9	22.8°

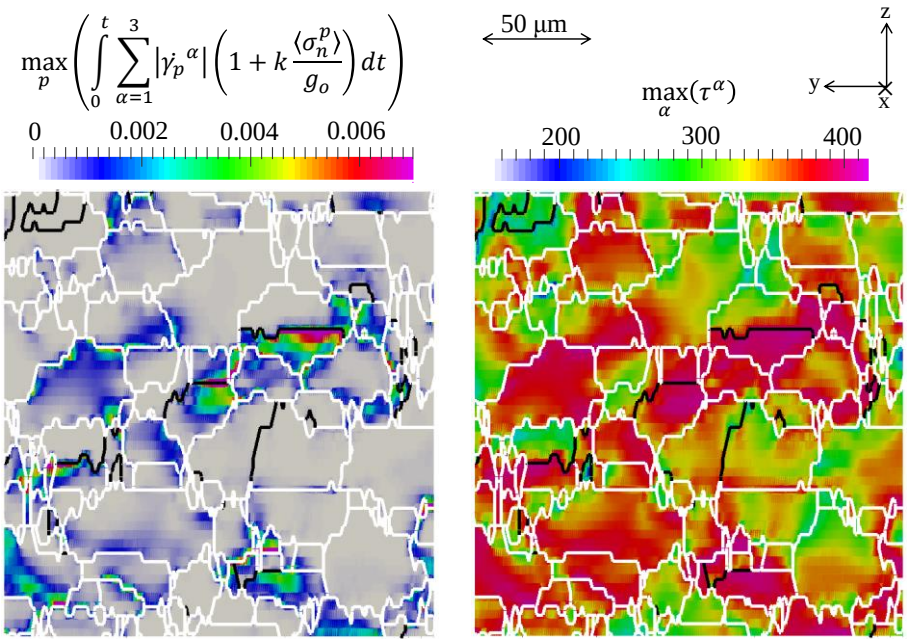

Figure 3.18: Fatemi-Socie parameter (D_5) and maximum resolved shear stress on a single slip system (S_1, MPa) on the free surface of the cropped reconstruction at 0.39% applied strain. Black and white grain boundaries demarcate the Σ3 and non-Σ3 conditions, respectively.

3.4.4.2 Establishing Correlations

The Fatemi-Socie parameter (D_5) and the maximum resolved shear stress on a single slip system (S_1) at 0.39% applied strain are considered in Figure 3.19, wherein these metrics are grouped by average grain size (an indication of grain boundary length), degree of inclination of the boundary with the loading axis, Schmid factor, stiffness ratio, misorientation, and boundary type.

With regards to grain size, taken here to be the average of the adjacent grains' sphere-equivalent diameters, both slip- and stress-based metrics increased for increasing grain size. It is noteworthy that even out to high grain sizes (> 25 μm), this effect does not saturate. One could draw parallels with this result and Miao *et al.*'s [68] observations that microcracks tend to nucleate in clusters of large grains. Moreover, it underpins the need to preserve and account for the effects of the largest (as-large-as, ALA) grains in the microstructure in the microstructure [112].

The inclination of the grain boundary with respect to the loading axis, measured here as the scalar product of the grain boundary normal and loading axis, does not seem to be correlated as strongly to the localization event as grain size. It appears that boundaries inclined to the loading axis are favored for slip activity, which is again consistent with Miao *et al.*'s [68] observations. For increasing inclination (increasing scalar product), incompatibility stresses should tend to zero, but these results indicate a preference for localization despite their absence. This does not suggest that incompatibility stresses are inconsequential, rather, their relevance with respect to microcrack nucleation decreases with increasing inclination.

The grain boundary analysis yielded no correlation between Schmid factor and slip localization. This was also the case for stiffness gradient (measured here as the ratio between the maximum and minimum Schmid factors associated with the boundary). These results are somewhat peculiar given that Schmid factor has long been correlated with microcrack nucleation in the literature. Of course, the analysis does not contradict these experimental observations, but suggests that Schmid factor alone is insufficient to gauge the propensity for microcrack nucleation in this case.

Misorientation was found to be strongly correlated to the localization event— both S_1 and D_5 increased for increasing misorientation angle. Moreover, Σ3 boundaries and non-Σ3, high-angle boundaries showed roughly the same propensity for localization, indicating that the microcrack nucleation event is not exclusive to twin boundaries. In Figure 3.20, two measures of slip plane coplanarity were considered for both types of boundaries: $\max\left(\left|\boldsymbol{n}_{GB}\cdot\boldsymbol{n}_p\right|\right)$, the scalar product of the grain boundary normal and the normal of the most aligned slip plane, and $\sum_p\left|\boldsymbol{n}_{GB}\cdot\boldsymbol{n}_p\right|$, the summation of scalar products of the grain boundary normal and slip plane normals. Note that the second measure appears in the calculation for F_{1stp}. For non-Σ3 boundaries, the analysis showed that S_1 and D_5 increased for increasing $\max\left(\left|\boldsymbol{n}_{GB}\cdot\boldsymbol{n}_p\right|\right)$ and decreased for increasing

$\sum_p |\boldsymbol{n}_{GB} \cdot \boldsymbol{n}_p|$. For Σ3 boundaries, on the other hand, no correlations could be made with these two coplanarity measures. This does not suggest that coplanarity is inconsequential at Σ3 boundaries. As discussed in Section 3.4.2, the slip localization's extent, and not necessarily its magnitude (which is considered in this study), is directly proportional to the degree of coplanarity at Σ3 boundaries.

3.4.4.3 Comparing Correlations

In Section 3.4.4.2, individual microstructural features were correlated to multiple microcrack nucleation metrics. In this section, the relative strength of these correlations is compared in chord diagrams, Figure 3.21. Each chord's thickness is predicated on the magnitude of the Pearson's correlation coefficient between the associated metric and feature— thicker chords indicate stronger correlations. The S1 metric was correlated most strongly to Schmid and Taylor factors, grain size, misorientation, and the first coplanarity measure. The D3 metric, in turn, was correlated the strongest to grain size, misorientation, and the first coplanarity measure. The same was true for the D5 metric. With regards to the first coplanarity measure, its strong correlation with all three metrics indicates the primacy of a single coherent slip plane in the localization event. It is noteworthy that grain boundary type is correlated weakly to the localization event, suggesting that slip does not localize exclusively along Σ3 boundaries. Moreover, grain boundary inclination with the loading axis is also weakly correlated to the localization event.

3.5 Conclusions and Future Work

A Digital Twin framework of the nickel-based superalloy LSHR was established to account for its predominant microcrack nucleation mechanism at room temperature. The crystal-plastic finite-element method was applied to a reconstruction of LSHR taken from nf-HEDM measurements. The following can be concluded from this effort:

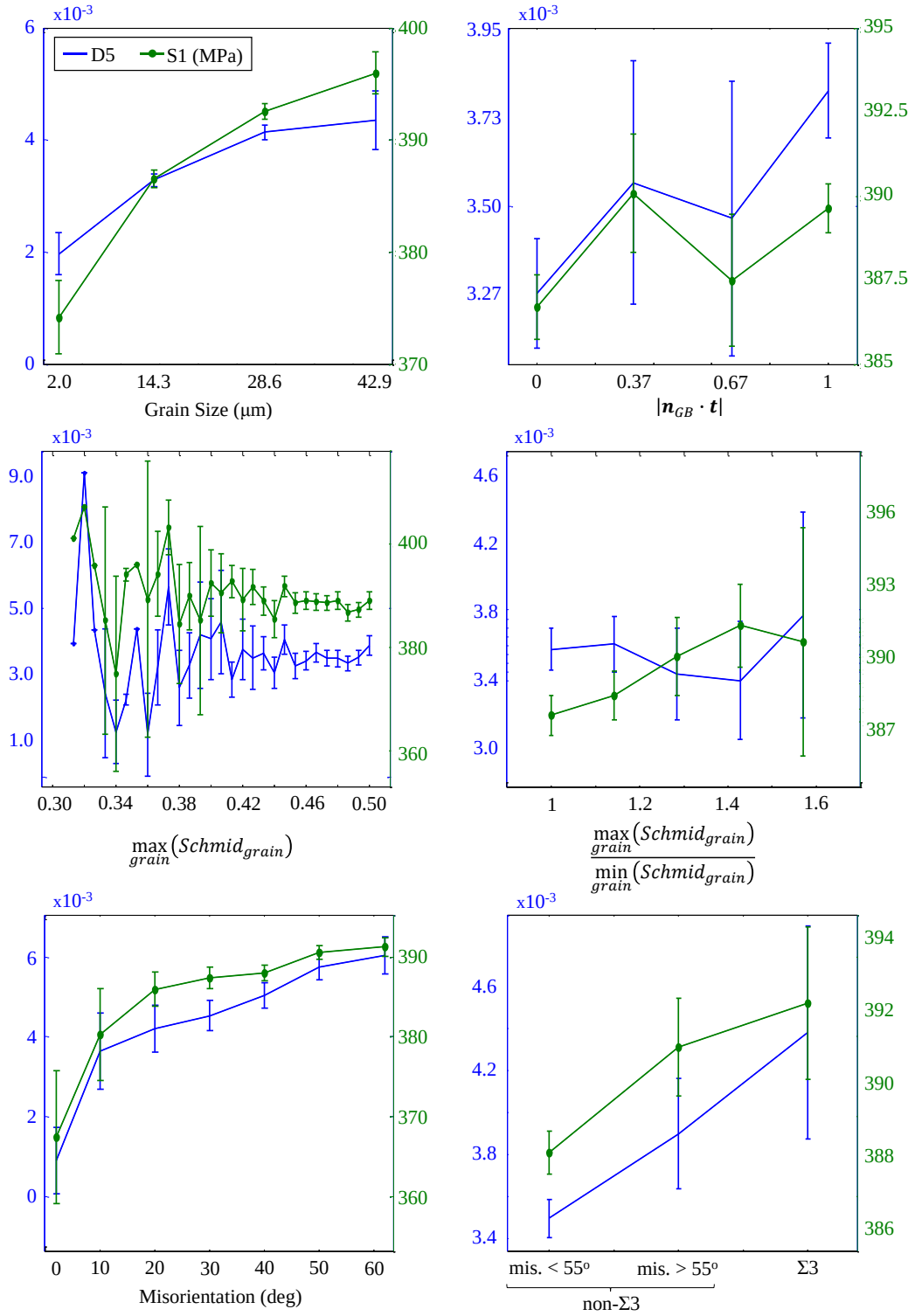

Figure 3.19: Mean Fatemi-Socie parameter (D_5) and maximum resolved shear stress on a single slip system (S_1) grouped by average grain size of adjacent grains (top-left), degree of inclination between grain boundary normal and loading direction (top-right), Schmid factor (middle-left), stiffness ratio (middle-right), misorientation (bottom-left), and boundary type (bottom-right) with 95% confidence intervals.

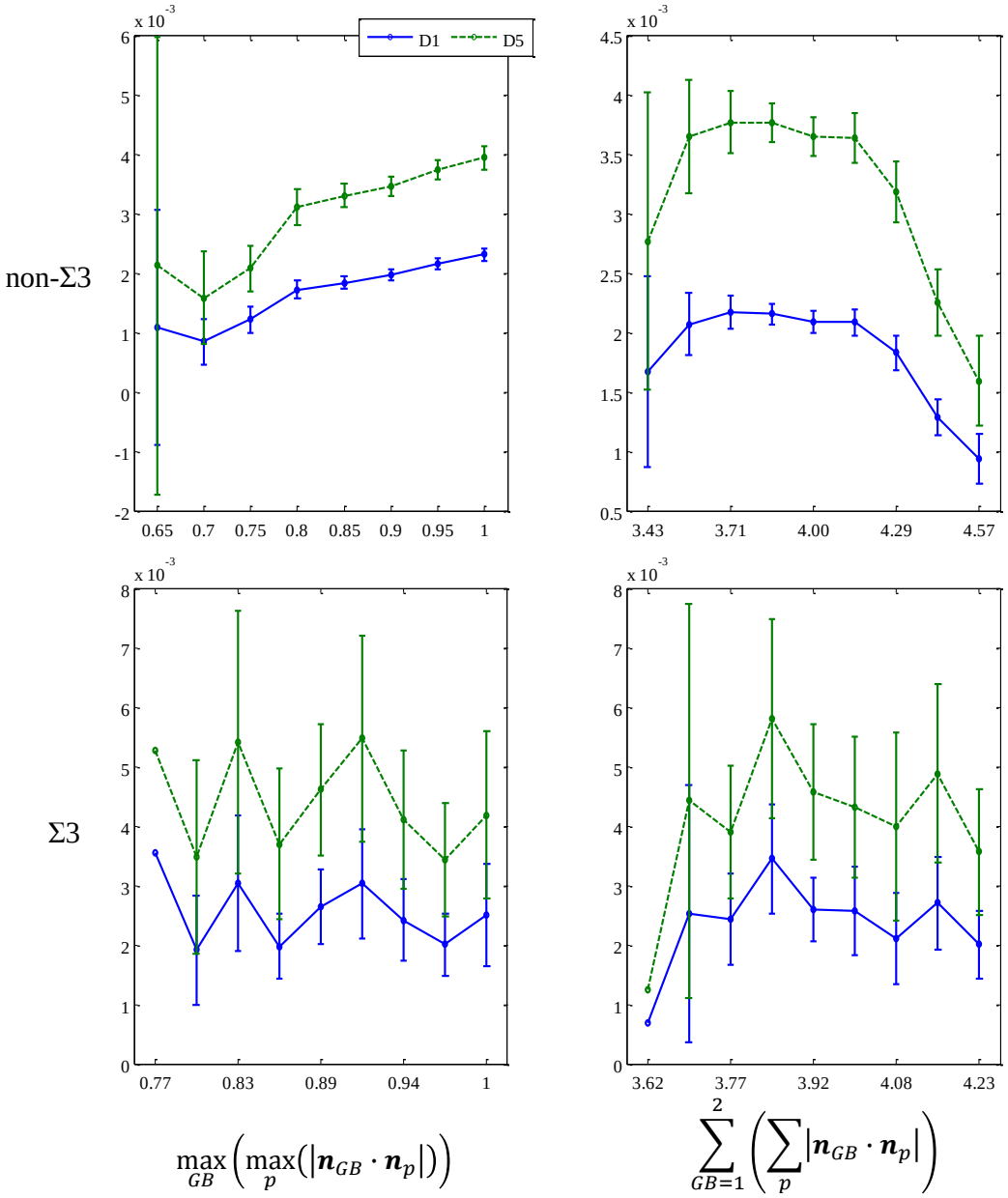

Figure 3.20: Mean maximum accumulated slip (D_1) and Fatemi-Socie parameter (D_5) for non-Σ3 boundaries (top) and Σ3 boundaries (bottom) grouped by two measures of slip plane coplanarity at the Σ3 boundaries with 95% confidence intervals.

- At low strains, the elastic anisotropy at high-angle grain boundaries is sufficient to evolve a slip hotspot. The extent and magnitude of this hotspot is dependent on the relative orientation of slip planes with the grain boundary— coherent boundaries, in general, are favored for slip accumulation. At non-Σ3 boundaries,

the magnitude of the slip localization is directly proportional to the degree of coplanarity. At Σ3 boundaries, the localization's extent (and not necessarily its magnitude) is directly proportional to the degree of coplanarity.

- Simulation results suggest that high elastic anisotropy and coplanarity of the boundary plane with a {111} slip plane were responsible for the accumulation of irreversible plastic slip and subsequently the microcrack nucleation event at the Σ3 boundary where a microcrack was known to nucleate.
- At high strains, the gradient term in the crystal plasticity model is necessary to accentuate hotspots along high-angle boundaries.

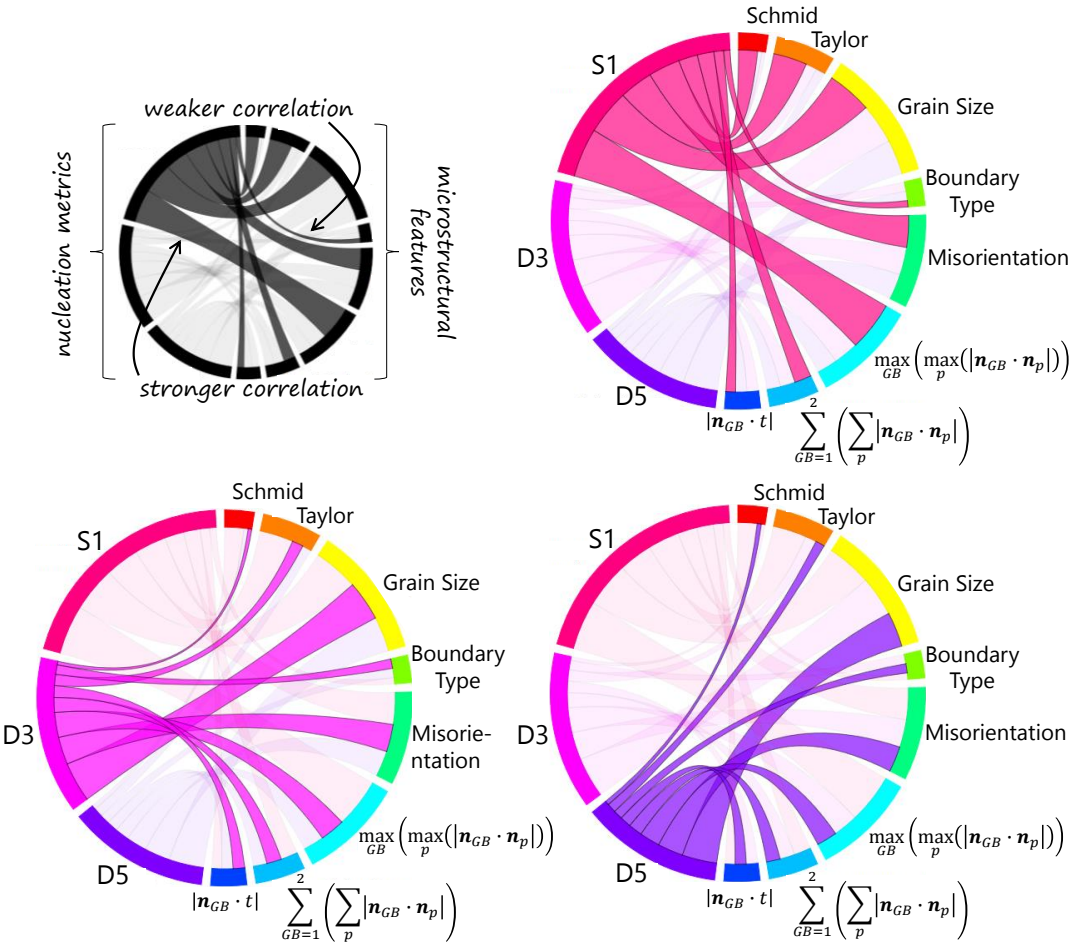

Figure 3.21: Chord diagrams correlating microcrack nucleation metrics to microstructural features. Diagrams generated with Data-Driven Documents (D3) [113].

- Slip accumulation at a grain boundary in LSHR is directly proportional to grain size, misorientation, and coplanarity of a single aligned slip plane with the boundary plane. Non-Σ3, high-angle boundaries show roughly the same propensity for slip localization as Σ3 boundaries.

The framework reproduces physically realistic behavior, but additional experimental observations of nucleated microcracks are needed to validate it completely. Furthermore, the framework neither considers explicitly the presence of γ′ nor its contribution to microcrack nucleation in LSHR. Rather than homogenize its influence through a careful consideration of crystal plasticity parameters, as was done herein, future efforts should attempt to incorporate γ′ into the CP-FEM with the highest fidelity possible.

3.6 Acknowledgements

This research was funded by the Air Force Office of Scientific Research under grant number FA9550-10-1-0213, supervised by Dr. David Stargel. All computations were conducted on Texas Advanced Computing Center's cluster Stampede on allocation TG-MSS110031 provided by the XSEDE Science Gateways program and supported by the National Science Foundation. This research was also made possible by support from the Ross-Tetelman Fellowship at Cornell University. Orientation maps in 3D were reconstructed using IceNine, a software implementation of [83] by S.F. Li. The authors acknowledge Professor Antoinette Maniatty and Dr. Devin Pyle of RPI for assistance with the crystal plasticity model. Finally, the authors thank GE Global Research (especially Dr. James Laflen and Dr. Adrian Loghin) for their collaboration and contributions to the development of the crystal plasticity model.

APPENDIX I

MATERIAL TANGENT MATRIX

1. Formulation

The material tangent stiffness matrix **D** is defined as follows:

$$D_{ij} = \frac{\partial T_i}{\partial \Delta_j} \tag{A.1}$$

$$\mathbf{D} = \begin{bmatrix} \dfrac{\partial T_{\mathrm{t}1}(\Delta_{\mathrm{n}}, \Delta_{\mathrm{t}1}, \Delta_{\mathrm{t}2})}{\partial \Delta_{\mathrm{t}1}} & \dfrac{\partial T_{\mathrm{t}1}(\Delta_{\mathrm{n}}, \Delta_{\mathrm{t}1}, \Delta_{\mathrm{t}2})}{\partial \Delta_{\mathrm{t}2}} & \dfrac{\partial T_{\mathrm{t}1}(\Delta_{\mathrm{n}}, \Delta_{\mathrm{t}1}, \Delta_{\mathrm{t}2})}{\partial \Delta_{\mathrm{n}}} \\ \dfrac{\partial T_{\mathrm{t}2}(\Delta_{\mathrm{n}}, \Delta_{\mathrm{t}1}, \Delta_{\mathrm{t}2})}{\partial \Delta_{\mathrm{t}1}} & \dfrac{\partial T_{\mathrm{t}2}(\Delta_{\mathrm{n}}, \Delta_{\mathrm{t}1}, \Delta_{\mathrm{t}2})}{\partial \Delta_{\mathrm{t}2}} & \dfrac{\partial T_{\mathrm{t}2}(\Delta_{\mathrm{n}}, \Delta_{\mathrm{t}1}, \Delta_{\mathrm{t}2})}{\partial \Delta_{\mathrm{n}}} \\ \dfrac{\partial T_{\mathrm{n}}(\Delta_{\mathrm{n}}, \Delta_{\mathrm{t}})}{\partial \Delta_{\mathrm{t}1}} & \dfrac{\partial T_{\mathrm{n}}(\Delta_{\mathrm{n}}, \Delta_{\mathrm{t}})}{\partial \Delta_{\mathrm{t}2}} & \dfrac{\partial T_{\mathrm{n}}(\Delta_{\mathrm{n}}, \Delta_{\mathrm{t}})}{\partial \Delta_{\mathrm{n}}} \end{bmatrix} \tag{A.2}$$

for i = 1, 2

$$\frac{\partial T_{\mathrm{t}i}}{\partial \Delta_{\mathrm{n}}} = \frac{\partial T_{\mathrm{n}}}{\partial \Delta_{\mathrm{t}i}} = \frac{\Gamma_{\mathrm{t}}\Gamma_{\mathrm{n}}\Delta_{\mathrm{t}i}}{\delta_{\mathrm{t}}\delta_{\mathrm{n}}\Delta_{\mathrm{t}}}\left[n\left(1-\frac{\Delta_{\mathrm{t}}}{\delta_{\mathrm{t}}}\right)^{\beta}\left(\frac{n}{\beta}+\frac{\Delta_{\mathrm{t}}}{\delta_{\mathrm{t}}}\right)^{n-1} - \beta\left(1-\frac{\Delta_{\mathrm{t}}}{\delta_{\mathrm{t}}}\right)^{\beta-1}\left(\frac{n}{\beta}+\frac{\Delta_{\mathrm{t}}}{\delta_{\mathrm{t}}}\right)^{n}\right]$$
$$\left(-\frac{\alpha\left(1-\frac{\Delta_{\mathrm{n}}}{\delta_{\mathrm{n}}}\right)^{\alpha}\left(\frac{m}{\alpha}+\frac{\Delta_{\mathrm{n}}}{\delta_{\mathrm{n}}}\right)^{m}}{1-\frac{\Delta_{\mathrm{n}}}{\delta_{\mathrm{n}}}} + \frac{m\left(1-\frac{\Delta_{\mathrm{n}}}{\delta_{\mathrm{n}}}\right)^{\alpha}\left(\frac{m}{\alpha}+\frac{\Delta_{\mathrm{n}}}{\delta_{\mathrm{n}}}\right)^{m}}{\left(\frac{m}{\alpha}-\frac{\Delta_{\mathrm{n}}}{\delta_{\mathrm{n}}}\right)} \right) \tag{A.3}$$

for i = 1, 2

$$\frac{\partial T_{ti}}{\partial \Delta_{ti}} = \left[\Gamma_n \left(1 - \frac{\Delta_n}{\delta_n}\right)^{\alpha} \left(\frac{m}{\alpha} + \frac{\Delta_n}{\delta_n}\right)^{m} + \langle \phi_n - \phi_t \rangle\right]$$

$$\left(\frac{\Delta_{ti}^2 \Gamma_t}{\delta_t^2 \Delta_t^2}\left[-\frac{n\beta\left(1 - \frac{\Delta_t}{\delta_t}\right)^{\beta}\left(\frac{n}{\beta} + \frac{\Delta_t}{\delta_t}\right)^{n-1}}{1 - \frac{\Delta_t}{\delta_t}} + \frac{n(n-1)\left(1 - \frac{\Delta_t}{\delta_t}\right)^{\beta}\left(\frac{n}{\beta} + \frac{\Delta_t}{\delta_t}\right)^{n-1}}{\frac{n}{\beta} + \frac{\Delta_t}{\delta_t}}\right.\right.$$

$$\left. + \frac{\beta(\beta-1)\left(1 - \frac{\Delta_t}{\delta_t}\right)^{\beta-1}\left(\frac{n}{\beta} + \frac{\Delta_t}{\delta_t}\right)^{n}}{1 - \frac{\Delta_t}{\delta_t}} - \frac{\beta n\left(1 - \frac{\Delta_t}{\delta_t}\right)^{\beta-1}\left(\frac{n}{\beta} + \frac{\Delta_t}{\delta_t}\right)^{n}}{\frac{n}{\beta} + \frac{\Delta_t}{\delta_t}}\right] \qquad \text{(A. 4)}$$

$$+ \left(n\left(1 - \frac{\Delta_t}{\delta_t}\right)^{\beta}\left(\frac{n}{\beta} + \frac{\Delta_t}{\delta_t}\right)^{n-1} - \beta\left(1 - \frac{\Delta_t}{\delta_t}\right)^{\beta-1}\left(\frac{n}{\beta} + \frac{\Delta_t}{\delta_t}\right)^{n}\right)\frac{\Gamma_t}{\delta_t}\left[\frac{1}{\Delta_t}\right.$$

$$\left.\left. - \frac{\Delta_{ti}}{(\Delta_{t1}^2 + \Delta_{t2}^2)^{3/2}}\right]\right)$$

$$\frac{\partial T_{t1}}{\partial \Delta_{t2}} = \frac{\partial T_{t2}}{\partial \Delta_{t1}} = \Gamma_t \Delta_{t1} \Delta_{t2} \beta(n+\beta)\left[\Gamma_n \left(1 - \frac{\Delta_n}{\delta_n}\right)^{\alpha}\left(\frac{m}{\alpha} + \frac{\Delta_n}{\delta_n}\right)^{m} + \langle \phi_n - \phi_t \rangle\right]$$

$$\left[\frac{\beta\left(1 - \frac{\Delta_t}{\delta_t}\right)^{\beta}\left(\frac{n}{\beta} - \frac{\Delta_t}{\delta_t}\right)^{n}}{(\delta_t - \Delta_t)^2(n\delta_t + \beta\Delta_t)\Delta_t} - \frac{\beta n\left(1 - \frac{\Delta_t}{\delta_t}\right)^{\beta}\left(\frac{n}{\beta} - \frac{\Delta_t}{\delta_t}\right)^{n}}{(\delta_t - \Delta_t)(n\delta_t + \beta\Delta_t)^2\Delta_t}\right. \qquad \text{(A. 5)}$$

$$\left. + \frac{\beta\left(1 - \frac{\Delta_t}{\delta_t}\right)^{\beta}\left(\frac{n}{\beta} - \frac{\Delta_t}{\delta_t}\right)^{n}}{(\delta_t - \Delta_t)(n\delta_t + \beta\Delta_t)^2\Delta_t} - \frac{\left(1 - \frac{\Delta_t}{\delta_t}\right)^{\beta}\left(\frac{n}{\beta} - \frac{\Delta_t}{\delta_t}\right)^{n}}{(\delta_t - \Delta_t)^2(n\delta_t + \beta\Delta_t)\Delta_t}\right]$$

$$\frac{\partial T_{\mathrm{n}}}{\partial \Delta_{\mathrm{n}}} = \frac{\Gamma_{\mathrm{n}}}{\delta_{\mathrm{n}}}\left[\Gamma_{\mathrm{t}}\left(1-\frac{\Delta_{\mathrm{t}}}{\delta_{\mathrm{t}}}\right)^{\beta}\left(\frac{n}{\beta}+\frac{\Delta_{\mathrm{t}}}{\delta_{\mathrm{t}}}\right)^{n} - \langle \phi_{\mathrm{t}} - \phi_{\mathrm{n}} \rangle\right]\left[-\frac{m\left(1-\frac{\Delta_{\mathrm{n}}}{\delta_{\mathrm{n}}}\right)^{\alpha}\alpha\left(\frac{m}{\alpha}+\frac{\Delta_{\mathrm{n}}}{\delta_{\mathrm{n}}}\right)^{m-1}}{1-\frac{\Delta_{\mathrm{n}}}{\delta_{\mathrm{n}}}}\right.$$
$$+\frac{m\left(1-\frac{\Delta_{\mathrm{n}}}{\delta_{\mathrm{n}}}\right)^{\alpha}\left(\frac{m}{\alpha}+\frac{\Delta_{\mathrm{n}}}{\delta_{\mathrm{n}}}\right)^{m-1}(m-1)}{\frac{m}{\alpha}+\frac{\Delta_{\mathrm{n}}}{\delta_{\mathrm{n}}}}$$
$$+\frac{\alpha\left(1-\frac{\Delta_{\mathrm{n}}}{\delta_{\mathrm{n}}}\right)^{\alpha-1}(\alpha-1)\left(\frac{m}{\alpha}+\frac{\Delta_{\mathrm{n}}}{\delta_{\mathrm{n}}}\right)^{m}}{1-\frac{\Delta_{\mathrm{n}}}{\delta_{\mathrm{n}}}} \qquad \text{(A. 6)}$$
$$\left.-\frac{\alpha\left(1-\frac{\Delta_{\mathrm{n}}}{\delta_{\mathrm{n}}}\right)^{\alpha-1}\left(\frac{m}{\alpha}+\frac{\Delta_{\mathrm{n}}}{\delta_{\mathrm{n}}}\right)^{m}m}{\frac{m}{\alpha}+\frac{\Delta_{\mathrm{n}}}{\delta_{\mathrm{n}}}}\right]$$

2. Unloading / Reloading

Define $\Delta_{\mathrm{n}}^{max}$ and $\Delta_{\mathrm{t}}^{max}$ to be the maximum normal and tangential separations, respectively, reached during loading / unloading. If $\Delta_{\mathrm{n}} = \Delta_{\mathrm{n}}^{max}$ and $\Delta_{\mathrm{t}} = \Delta_{\mathrm{t}}^{max}$, meaning that both the normal and shear are in the loading phase, the material tangent stiffness matrix is given by Equation A.2.

If $\Delta_{\mathrm{n}} < \Delta_{\mathrm{n}}^{max}$ and $\Delta_{\mathrm{t}} = \Delta_{\mathrm{t}}^{max}$, meaning that the normal is in the unload / reload phase and shear is loading, the matrix is given by:

$$\mathbf{D} = \begin{bmatrix} \frac{\partial T_{\mathrm{t1}}(\Delta_{\mathrm{n}}^{max}, \Delta_{\mathrm{t}}, |\Delta_{\mathrm{t1}}|)}{\partial \Delta_{\mathrm{t1}}} & \frac{\partial T_{\mathrm{t1}}(\Delta_{\mathrm{n}}^{max}, \Delta_{\mathrm{t}}, |\Delta_{\mathrm{t1}}|)}{\partial \Delta_{\mathrm{t2}}} & \frac{\partial T_{\mathrm{t1}}(\Delta_{\mathrm{n}}^{max}, \Delta_{\mathrm{t}}, |\Delta_{\mathrm{t1}}|)}{\partial \Delta_{\mathrm{n}}} \\ \frac{\partial T_{\mathrm{t2}}(\Delta_{\mathrm{n}}^{max}, \Delta_{\mathrm{t}}, |\Delta_{\mathrm{t2}}|)}{\partial \Delta_{\mathrm{t1}}} & \frac{\partial T_{\mathrm{t2}}(\Delta_{\mathrm{n}}^{max}, \Delta_{\mathrm{t}}, |\Delta_{\mathrm{t2}}|)}{\partial \Delta_{\mathrm{t2}}} & \frac{\partial T_{\mathrm{t2}}(\Delta_{\mathrm{n}}^{max}, \Delta_{\mathrm{t}}, |\Delta_{\mathrm{t2}}|)}{\partial \Delta_{\mathrm{n}}} \\ \frac{\partial T_{\mathrm{n}}(\Delta_{\mathrm{n}}^{max}, \Delta_{\mathrm{t}})}{\partial \Delta_{\mathrm{t1}}}\frac{\Delta_{\mathrm{n}}}{\Delta_{\mathrm{n}}^{max}} & \frac{\partial T_{\mathrm{n}}(\Delta_{\mathrm{n}}^{max}, \Delta_{\mathrm{t}})}{\partial \Delta_{\mathrm{t2}}}\frac{\Delta_{\mathrm{n}}}{\Delta_{\mathrm{n}}^{max}} & \frac{T_{\mathrm{n}}(\Delta_{\mathrm{n}}^{max}, \Delta_{\mathrm{t}})}{\Delta_{\mathrm{n}}^{max}} \end{bmatrix} \qquad \text{(A. 7)}$$

If $\Delta_{\mathrm{n}} = \Delta_{\mathrm{n}}^{max}$ and $\Delta_{\mathrm{t}} < \Delta_{\mathrm{t}}^{max}$, meaning that the normal is loading and the shear is in the unload / reload phase, the matrix is given by:

$$\mathbf{D} = \begin{bmatrix} \dfrac{T_{\mathrm{t}}(\Delta_{\mathrm{n}}, \Delta_{\mathrm{t}}^{max})}{\Delta_{\mathrm{t}}^{max}} & 0 & \dfrac{\partial T_{\mathrm{t}}(\Delta_{\mathrm{n}}, \Delta_{\mathrm{t}}^{max})}{\partial \Delta_{\mathrm{n}}} \dfrac{|\Delta_{\mathrm{t1}}|}{\Delta_{\mathrm{t}}^{max}} \\ 0 & \dfrac{T_{\mathrm{t}}(\Delta_{\mathrm{n}}, \Delta_{\mathrm{t}}^{max})}{\Delta_{\mathrm{t}}^{max}} & \dfrac{\partial T_{\mathrm{t}}(\Delta_{\mathrm{n}}, \Delta_{\mathrm{t}}^{max})}{\partial \Delta_{\mathrm{n}}} \dfrac{|\Delta_{\mathrm{t2}}|}{\Delta_{\mathrm{t}}^{max}} \\ \dfrac{\partial T_{\mathrm{n}}(\Delta_{\mathrm{n}}, \Delta_{\mathrm{t}})}{\partial \Delta_{\mathrm{t1}}} & \dfrac{\partial T_{\mathrm{n}}(\Delta_{\mathrm{n}}, \Delta_{\mathrm{t}})}{\partial \Delta_{\mathrm{t2}}} & \dfrac{\partial T_{\mathrm{n}}(\Delta_{\mathrm{n}}, \Delta_{\mathrm{t}})}{\partial \Delta_{\mathrm{n}}} \end{bmatrix} \quad \text{(A. 8)}$$

Finally, if $\Delta_{\mathrm{n}} < \Delta_{\mathrm{n}}^{max}$ and $\Delta_{\mathrm{t}} < \Delta_{\mathrm{t}}^{max}$, meaning that the normal and shear are unloading / reloading, the matrix is given by:

$$\mathbf{D} = \begin{bmatrix} \dfrac{T_{\mathrm{t}}(\Delta_{\mathrm{n}}, \Delta_{\mathrm{t}}^{max})}{\Delta_{\mathrm{t}}^{max}} & 0 & \dfrac{\partial T_{\mathrm{t}}(\Delta_{\mathrm{n}}, \Delta_{\mathrm{t}}^{max})}{\partial \Delta_{\mathrm{n}}} \dfrac{|\Delta_{\mathrm{t1}}|}{\Delta_{\mathrm{t}}^{max}} \\ 0 & \dfrac{T_{\mathrm{t}}(\Delta_{\mathrm{n}}, \Delta_{\mathrm{t}}^{max})}{\Delta_{\mathrm{t}}^{max}} & \dfrac{\partial T_{\mathrm{t}}(\Delta_{\mathrm{n}}, \Delta_{\mathrm{t}}^{max})}{\partial \Delta_{\mathrm{n}}} \dfrac{|\Delta_{\mathrm{t2}}|}{\Delta_{\mathrm{t}}^{max}} \\ \dfrac{\partial T_{\mathrm{n}}(\Delta_{\mathrm{n}}^{max}, \Delta_{\mathrm{t}})}{\partial \Delta_{\mathrm{t1}}} \dfrac{\Delta_{\mathrm{n}}}{\Delta_{\mathrm{n}}^{max}} & \dfrac{\partial T_{\mathrm{n}}(\Delta_{\mathrm{n}}^{max}, \Delta_{\mathrm{t}})}{\partial \Delta_{\mathrm{t2}}} \dfrac{\Delta_{\mathrm{n}}}{\Delta_{\mathrm{n}}^{max}} & \dfrac{T_{\mathrm{n}}(\Delta_{\mathrm{n}}^{max}, \Delta_{\mathrm{t}})}{\Delta_{\mathrm{n}}^{max}} \end{bmatrix} \quad \text{(A. 9)}$$

3. Contact

Material self-penetration is prevented through a penalty method. When $\Delta_{\mathrm{n}} < 0$, the normal traction is given by:

$$T_{\mathrm{n}}(\Delta_{\mathrm{n}} < 0, \Delta_{\mathrm{t1}}, \Delta_{\mathrm{t2}}) = \Delta_{\mathrm{n}} \left\{ \frac{\Gamma_{\mathrm{n}} \alpha}{\delta_{\mathrm{n}}^2} \left[-\left(\frac{m}{\alpha}\right)^{m-1} - \left(\frac{m}{\alpha}\right)^{m} \right] \left[\Gamma_{\mathrm{t}} \left(\frac{n}{\beta}\right)^{n} + \langle \phi_t - \phi_n \rangle \right] \right\}, \quad \text{(A. 10)}$$

where the expression in braces, the penalty stiffness, is assigned to the D_{nn} entry of the material tangent stiffness matrix. The matrix is given by:

$$\mathbf{D} = \begin{bmatrix} \dfrac{\partial T_{\mathrm{t1}}(0, \Delta_{\mathrm{t}}, |\Delta_{\mathrm{t1}}|)}{\partial \Delta_{\mathrm{t1}}} & \dfrac{\partial T_{\mathrm{t1}}(0, \Delta_{\mathrm{t}}, |\Delta_{\mathrm{t1}}|)}{\partial \Delta_{\mathrm{t2}}} & 0 \\ \dfrac{\partial T_{\mathrm{t2}}(0, \Delta_{\mathrm{t}}, |\Delta_{\mathrm{t2}}|)}{\partial \Delta_{\mathrm{t1}}} & \dfrac{\partial T_{\mathrm{t2}}(0, \Delta_{\mathrm{t}}, |\Delta_{\mathrm{t2}}|)}{\partial \Delta_{\mathrm{t2}}} & 0 \\ 0 & 0 & \dfrac{\Gamma_{\mathrm{n}} \alpha}{\delta_{\mathrm{n}}^2} \left[-\left(\dfrac{m}{\alpha}\right)^{m-1} - \left(\dfrac{m}{\alpha}\right)^{m} \right] \left[\Gamma_{\mathrm{t}} \left(\dfrac{n}{\beta}\right)^{n} + \langle \phi_t - \phi_n \rangle \right] \end{bmatrix} \quad \text{(A. 11)}$$

APPENDIX II

ABAQUS PPR UEL

```
! ============================================================================
! Three-Dimensional Linear Cohesive Zone Element for the Intrinsic PPR Model
!
!   4,8        3,7
!   x----------x
!   |          |
!   |          |
!   x----------x
!   1,5        2,6
!
! Developed by Albert Cerrone, 2013 (arc247@cornell.edu)
!
! Adapted from 2D PPR UEL written by Kyoungsoo Park and Glaucio H. Paulino,
! which is published in Computational Implementation of the PPR Potential-
! Based Cohesive Model in ABAQUS: Educational Perspective (Engineering
! Fracture Mechanics, Vol 93, 2012, pp. 239-262)
! ============================================================================
SUBROUTINE UEL (RHS, AMATRX, SVARS, ENERGY, NDOFEL, NRHS, NSVARS, PROPS, &
        NPROPS, COORDS, MCRD, NNODE, U, DU, V, A, JTYPE, TIME, DTIME, KSTEP, &
        KINC, JELEM, PARAMS, NDLOAD, JDLTYP, ADLMAG, PREDEF, NPREDF, LFLAGS, &
        MLVARX, DDLMAG, MDLOAD, PNEWDT, JPROPS, NJPRO, PERIOD)
INCLUDE 'ABA_PARAM.INC'
!
! ABAQUS Variables
DIMENSION RHS(MLVARX,*), AMATRX(NDOFEL,NDOFEL), PROPS(*), SVARS(8), ENERGY(8), &
        COORDS(MCRD, NNODE), U(NDOFEL), DU(MLVARX,*), V(NDOFEL), A(NDOFEL), &
        TIME(2), PARAMS(*), JDLTYP(MDLOAD,*), ADLMAG(MDLOAD,*), DDLMAG(MDLOAD,*), &
        PREDEF(2, NPREDF, NNODE), LFLAGS(*), JPROPS(*)
! where...
! SVARS : Maximum separation at each integration point (two per GP, eight total)
!
! Input parameters (defined in .inp file)
! PROPS(1): Normal fracture energy (Gn)
! PROPS(2): Tangential fracture energy (Gt)
! PROPS(3): Normal cohesive strength (Tn_m)
! PROPS(4): Tangential cohesive strength (Tt_m)
! PROPS(5): Normal shape parameter (alph)
! PROPS(6): Tangential shape parameter (beta)
! PROPS(7): Normal initial slope indicator (ln)
! PROPS(8): Tangential initial slope indicator (lt)
!
! Other Variables:
! MCRD : Largest active degree of freedom (Coordinates parameter)
! NNODE : Number of nodes
! COORDS: matrix of nodal coordinates
!
    ! Variables used in the UEL subroutine
    DIMENSION Sc(ndofel,ndofel), Fc(ndofel,nrhs), &
        T(mcrd,nrhs), T_d(mcrd,mcrd), U_l(ndofel), R(mcrd, mcrd), &
        Bc(mcrd,ndofel), Bct(ndofel,mcrd), ShapeN(nnode), &
        del(mcrd), GP_xi(4), GP_eta(4), GP_w(4), tmp(ndofel,mcrd), &
        L(3,24)
    !   where...
    !   Sc : Element stiffness matrix of a cohesive element
    !   Fc : Cohesive internal force vector
    !   T : Cohesive traction vector
    !   T_d : Derivative of the cohesive traction (Tangent matrix)
    !   U_l : Nodal displacement in the local coordinate system
    !   R : Coordinate transformation matrix
    !   Bc : Global displacement-separation relation matrix
    !   L: Relation Matrix
    !   del : Normal and tangential separation
    !   GP : Gauss points
```

```
!   GP_W: Weight at the Gauss points
!
! Initialize
DOUBLE PRECISION Gn, Gt, Tn_m, Tt_m, alph, beta, ln, lt, th, &
    dn, dt, m, n, Gam_n, Gam_t, dGnt, dGtn, L, scalar, &
    N1, N2, del1, del2, del3, del4, deln_max, delt_max, &
    N3, N4, del5, del6, del7, del8, del9, del10, del11, del12, R, Bc, &
    Tt1, Tt2, UTol, mediff, NSlopeInit, T, T_d, del, delt, &
    DeltTbar, DeltNbar, dx_gauss, dy_gauss, dz_gauss, DJ
!   where ...
!   Gn, Gt: Fracture energy
!   Tn_m, Tt_m: Cohesive strength
!   alph, beta: Shape parameter
!   ln, lt: Initial slope indicators
!   th : Thickness of a cohesive element
!   dn, dt: Final crack opening width
!   m, n : Exponents in the PPR potential
!   Gam_n, Gam_t: Energy constants in the PPR potential
!   dGnt : <Gn - Gt>
!   dGtn : <Gt - Gn>
!   N1, N2: Linear shape functions
!   del1, del2, del3, del4: Nodal separations
!   deln_max, delt_max: Maximum separations in a loading history
!   n_GP: Number of Gauss points
!
! Read input data
Gn = PROPS(1)
Gt = PROPS(2)
Tn_m = PROPS(3)
Tt_m = PROPS(4)
alph = PROPS(5)
beta = PROPS(6)
ln = PROPS(7)
lt = PROPS(8)
n_GP = 4
!
! Specify Gauss point coordinates and weights
data GP_xi / -0.577350269189626 , 0.577350269189626 , &
                    0.577350269189626 , -0.577350269189626 /
data GP_eta / -0.577350269189626 , -0.577350269189626 , &
                    0.577350269189626 , 0.577350269189626 /
data GP_W / 1.0 , 1.0 , 1.0 , 1.0 /
!
! Initialize RHS (f) and stiffness matrix (K)
call k_Matrix_Zero (RHS,ndofel,nrhs)
call k_Matrix_Zero (AMATRX,ndofel,ndofel)
!
! Calculate m, n, energy constants, final opening widths, etc.
m = (alph-1)*alph*ln**2/(1-alph*ln**2)
n = (beta-1)*beta*lt**2/(1-beta*lt**2)
dn = alph*Gn/(m*Tn_m)*(1-ln)**(alph-1) &
    * (alph/m*ln+1)**(m-1)*(alph+m)*ln
dt = beta*Gt/(n*Tt_m)*(1-lt)**(beta-1) &
    * (beta/n*lt+1)**(n-1)*(beta+n)*lt
if (dt .LT. dn) then
    UTol = 1E-13*dt
else
    UTol = 1E-13*dn
endif
if (Gt .GT. Gn) then
    dGnt = 0
    dGtn = Gt - Gn
elseif (Gt .LT. Gn) then
    dGnt = Gn - Gt
    dGtn = 0
else
    dGnt = 0
    dGtn = 0
endif
```

```
if (Gn .EQ. Gt) then
    Gam_n = -Gn*(alph/m)**(m)
    Gam_t = (beta/n)**(n)
else
    Gam_n = (-Gn)**(dGnt/(Gn-Gt))*(alph/m)**(m)
    Gam_t = (-Gt)**(dGtn/(Gt-Gn))*(beta/n)**(n)
endif
if (-(Gn-Gt) .GT. 0) then
    mediff = -(Gn-Gt)
else
    mediff = 0
endif
NSlopeInit = ((Gam_n*alph)/(dn*dn)) * (-(m/alph)**(m-1)-(m/alph)**m) * &
    (Gam_t*(n/beta)**n+mediff)
!
! Calculate conjugate final crack opening widths
DeltTbar = 0
DeltNbar = 0
call FindConjugateDeltTb (Gam_n, dt, beta, n, Gn, Gt, DeltTbar)
call FindConjugateDeltNb (Gam_t, dn, alph, m, Gn, Gt, DeltNbar)
!
! Numerical Integration at the Gauss points
do i = 1, n_GP
    !
    ! get rotation matrix
    call get_rotation (R, DJ, COORDS, U, ndofel, &
           nnode, mcrd, GP_xi(i), GP_eta(i))
    !
    ! calculate B matrix
    call get_B (L, Bc, R, GP_xi(i), GP_eta(i))
    !
    ! calculate del
    del(1)=0.0; del(2)=0.0; del(3)=0.0
    do j = 1, 3
           do k = 1, 24
                  del(j) = del(j) + Bc(j,k) * U(k)
           end do
    end do
    !
    ! get state variables
    delt_max = SVARS(2*(i-1)+1)
    deln_max = SVARS(2*(i-1)+2)
    !
    ! zero traction and tangent stiffness
    T(1,1)=0.0; T(2,1)=0.0; T(3,1)=0.0
    call k_Matrix_Zero (T_d, MCRD, MCRD)
    !
    ! get cohesive tractions and material tangent stiffness matrix
    call k_Cohesive_PPR (T, T_d, Gam_n, Gam_t, alph, beta, m, n, &
           dn, dt, dGtn, dGnt, del, deln_max, delt_max, &
           UTol, NSlopeInit, Gn, Gt, Gam_n, Gam_t, &
           DeltTbar, DeltNbar, i)
    !
    ! transpose(B) * D * B
    call k_Matrix_Transpose (Bc,Bct,mcrd,ndofel)
    call k_Matrix_Multiply (Bct,T_d,tmp,ndofel,mcrd,mcrd)
    call k_Matrix_Multiply (tmp,Bc,Sc,ndofel,mcrd,ndofel)
    !
    ! transpose(B) * T
    call k_Matrix_Multiply (Bct,T,Fc,ndofel,mcrd,nrhs)
    !
    ! add contribution to global stiffness matrix and RHS
    scalar = DJ*GP_W(i)
    call k_Matrix_PlusScalar (AMATRX,Sc,scalar,ndofel,ndofel)
    call k_Matrix_PlusScalar (RHS,-Fc,scalar,ndofel,nrhs)
    !
    ! update the state variables
    delt = (del(1)*del(1) + del(2)*del(2))**0.5
    if ((delt_max.LT.delt).AND.(delt.GT.lt*dt)) then
```

```
                SVARS(2*(i-1)+1) = delt
            end if
            if ((deln_max .LT. del(3)) .AND. (del(3) .GT. ln*dn)) then
                SVARS(2*(i-1)+2) = del(3)
            end if
        end do
        RETURN
        END
! ------------------------------------------------------------------------
! begin definitions of not-main subroutines
! ------------------------------------------------------------------------
! ======== Cohesive traction-separation relation for the PPR model ==========
        SUBROUTINE k_Cohesive_PPR (T, T_d, Gam_n, Gam_t, alph, beta, m, n, &
              dn, dt, dGtn, dGnt, del, deln_max, delt_max, UTol, NSlopeInit, &
              Gn, Gt, Gam_n, Gam_t, DeltTbar, DeltNbar, i)
        INCLUDE 'ABA_PARAM.INC'
        DIMENSION T(3,1), T_d(3,3), del(3), TEMP_TAN(3,3)
        DOUBLE PRECISION Gam_n, Gam_t, alph, beta, m, n, dn, dt, &
            dGtn, dGnt, deln_max, delt_max, Tn, Tt, deln, delt, &
            Tt1, Tt2, UTol, NSlopeInit, Gn, Gt, Gam_n, &
            Gam_t, DeltTbar, DeltNbar, sign1, sign2, signc, &
            Tn_max, Tt_max, T, T_d, TEMP_TAN, del
        INTEGER i
        delt = (del(1)*del(1) + del(2)*del(2))**0.5
        deln = del(3)
        call get_tangent_matrix (m, alph, n, beta, delt, Gam_t, Gam_n, dn, dt, &
                deln_max, delt_max, DeltTbar, DeltNbar, UTol, del, Gn, Gt, &
                NSlopeInit, dGtn, dGnt, T_d, i)
        call get_tractions (m, alph, n, beta, delt, Gam_t, Gam_n, dn, dt, &
                deln_max, delt_max, DeltTbar, DeltNbar, UTol, T, del, &
                Gn, Gt, NSlopeInit)
        RETURN
        END
! ======== tangent matrix ==========
        SUBROUTINE get_tangent_matrix (m, alph, n, beta, delt, &
                Gam_t, Gam_n, dn, dt, deln_max, &
                delt_max, DeltTbar, DeltNbar, UTol, del, Gam_n, Gam_t, &
                Gn, Gt, NSlopeInit, dGtn, dGnt, T_d, i)
        INCLUDE 'ABA_PARAM.INC'
        DIMENSION T_d(3,3), TEMP_TAN(3,3), del(3)
        DOUBLE PRECISION m, alph, n, beta, delt, dn, dt, Gam_t, Gam_n, &
                deln_max, delt_max, DeltTbar, DeltNbar, UTol, sign1, &
                sign2, signc, Gam_n, Gam_t, Gn, Gt, NSlopeInit, dGtn, &
                dGnt, del, T_d, TEMP_TAN
        INTEGER i
        TEMP_TAN(1,1)=0.0; TEMP_TAN(1,2)=0.0; TEMP_TAN(1,3)=0.0
        TEMP_TAN(2,1)=0.0; TEMP_TAN(2,2)=0.0; TEMP_TAN(2,3)=0.0
        TEMP_TAN(3,1)=0.0; TEMP_TAN(3,2)=0.0; TEMP_TAN(3,3)=0.0
        if (del(1) .LT. 0) then
            sign1 = -1
        else
            sign1 = 1
        endif
        if (del(2) .LT. 0) then
            sign2 = -1
        else
            sign2 = 1
        endif
        signc = sign1*sign2
        !   contact
        if (del(3) .LT. -UTol) then
            if (delt .LE. dt) then
                call DiffHelp (Gam_n, Gam_t, alph, beta, m, n, dn, dt, &
                       dGtn, dGnt, deln_max, delt_max, UTol, NSlopeInit, &
                       Gn, Gt, DeltNbar, DeltTbar, 0, abs(del(1)), &
                       abs(del(2)), TEMP_TAN, i)
                T_d(1,1) = TEMP_TAN(1,1)
                T_d(1,2) = signc*TEMP_TAN(1,2)
                T_d(2,1) = signc*TEMP_TAN(2,1)
```

```
            T_d(2,2) = TEMP_TAN(2,2)
        endif
        T_d(3,3) = NSlopeInit
        RETURN
    endif
    !   neither shear or tensile failure
    if ( (del(3).LT.DeltNbar) .AND. (abs(delt)).LT.DeltTbar ) then
        call DiffHelp (Gam_n, Gam_t, alph, beta, m, n, dn, dt, dGtn, &
                dGnt, deln_max, delt_max, UTol, NSlopeInit, Gn, Gt, &
                DeltNbar, DeltTbar, del(3), abs(del(1)), abs(del(2)), &
                TEMP_TAN, i)
        T_d(1,1) = TEMP_TAN(1,1)
        T_d(1,2) = signc*TEMP_TAN(1,2)
        T_d(1,3) = sign1*TEMP_TAN(1,3)
        T_d(2,1) = signc*TEMP_TAN(2,1)
        T_d(2,2) = TEMP_TAN(2,2)
        T_d(2,3) = sign2*TEMP_TAN(2,3)
        T_d(3,1) = sign1*TEMP_TAN(3,1)
        T_d(3,2) = sign2*TEMP_TAN(3,2)
        T_d(3,3) = TEMP_TAN(3,3)
        RETURN
    endif
    !   normal failure but shear still active
    if ( (delt.LT.dt) .AND. (del(3).LT.DeltNbar) ) then
        call DiffHelp (Gam_n, Gam_t, alph, beta, m, n, dn, dt, dGtn, &
                dGnt, deln_max, delt_max, UTol, NSlopeInit, Gn, Gt, &
                DeltNbar, DeltTbar, del(3), abs(del(1)), abs(del(2)), &
                TEMP_TAN, i)
        T_d(1,1) = TEMP_TAN(1,1)
        T_d(1,2) = signc*TEMP_TAN(1,2)
        T_d(1,3) = sign1*TEMP_TAN(1,3)
        T_d(2,1) = signc*TEMP_TAN(2,1)
        T_d(2,2) = TEMP_TAN(2,2)
        T_d(2,3) = sign2*TEMP_TAN(2,3)
        RETURN
    endif
    !   shear failure but normal still active
    if ( (del(3).LT.dn) .AND. (delt.LT.DeltTbar) ) then
        call DiffHelp (Gam_n, Gam_t, alph, beta, m, n, dn, dt, dGtn, &
                dGnt, deln_max, delt_max, UTol, NSlopeInit, Gn, Gt, &
                DeltNbar, DeltTbar, del(3), abs(del(1)), abs(del(2)), &
                TEMP_TAN, i)
        T_d(3,1) = sign1*TEMP_TAN(3,1)
        T_d(3,2) = sign2*TEMP_TAN(3,2)
        T_d(3,3) = TEMP_TAN(3,3)
        RETURN
    endif
    !   complete failure
    RETURN
    END
! ======== cohesive tractions ==========
    SUBROUTINE get_tractions (m, alph, n, beta, delt, Gam_t, Gam_n, dn, &
                      dt, deln_max, delt_max, DeltTbar, DeltNbar, UTol, &
                      T, del, Gn, Gt, NSlopeInit)
    INCLUDE 'ABA_PARAM.INC'
    DIMENSION T(3,1), del(3)
    DOUBLE PRECISION Tn, Tt, m, alph, n, beta, delt, Tn_max, Tt_max, &
                Gam_t, Gam_n, dn, dt, deln_max, delt_max, DeltTbar, &
                DeltNbar, UTol, Gn, Gt, NSlopeInit, T, del
    Tn = 0
    Tt = 0
    if ((del(3).LT.0) .OR. ((deln_max-del(3)).LT.UTol)) then
        call EvalNormal (m, alph, n, beta, delt, dt, del(3), dn, Gam_t, &
                Gam_n, DeltTbar, Gn, Gt, Tn, NSlopeInit)
    else
        call EvalNormal (m, alph, n, beta, delt, dt, deln_max, dn, Gam_t, &
                Gam_n, DeltTbar, Gn, Gt, Tn_max, NSlopeInit)
        Tn = del(3)*Tn_max/deln_max
    endif
```

```
      if ((abs(delt_max)-abs(delt)).LT.UTol) then
          call EvalShear (m, alph, n, beta, delt, dt, del(3), dn, Gam_t, &
                  Gam_n, DeltNbar, Gn, Gt, Tt)
      else
          call EvalShear (m, alph, n, beta, delt_max, dt, del(3), dn, Gam_t, &
                  Gam_n, DeltNbar, Gn, Gt, Tt_max)
          Tt = delt*Tt_max/delt_max
      endif
      if (del(1).EQ.0) then
          T(1,1) = 0
      else
          T(1,1) = Tt*del(1)/delt
      endif
      if (del(2).EQ.0) then
          T(2,1) = 0
      else
          T(2,1) = Tt*del(2)/delt
      endif
      T(3,1) = Tn
      RETURN
      END
! ======== zero out matrix ==========
      SUBROUTINE k_Matrix_Zero (A,n,m)
      INCLUDE 'ABA_PARAM.INC'
      DIMENSION A(n,m)
      do i = 1, n
          do j = 1, m
                  A(i,j) = 0.0
          end do
      end do
      RETURN
      END
! ======== transpose matrix ==========
      SUBROUTINE k_Matrix_Transpose (A,B,n,m)
      INCLUDE 'ABA_PARAM.INC'
      DIMENSION A(n,m), B(m,n)
      call k_Matrix_Zero (B,m,n)
      do i = 1, n
          do j = 1, m
                  B(j,i) = A(i,j)
          end do
      end do
      RETURN
      END
! ======== add scalar to matrix ==========
      SUBROUTINE k_Matrix_PlusScalar (A,B,c,n,m)
      INCLUDE 'ABA_PARAM.INC'
      DIMENSION A(n,m), B(n,m)
      do i = 1, n
          do j = 1, m
                  A(i,j) = A(i,j) + c*B(i,j)
          end do
      end do
      RETURN
      END
! ======== matrix multiply ==========
      SUBROUTINE k_Matrix_Multiply (A,B,C,l,n,m)
      INCLUDE 'ABA_PARAM.INC'
      DIMENSION A(l,n), B(n,m), C(l,m)
      call k_Matrix_Zero (C,l,m)
      do i = 1, l
          do j = 1, m
                  do k = 1, n
                          C(i,j) = C(i,j) + A(i,k) * B (k,j)
                  end do
          end do
      end do
      RETURN
      END
```

```
! ======== take first derivatives ==========
    SUBROUTINE DiffHelp (Gam_n, Gam_t, alph, beta, m, n, dn, dt, &
                         dGtn, dGnt, deln_max, delt_max, UTol, NSlopeInit, &
                         Gn, Gt, DeltNbar, DeltTbar, deln, delt1, delt2, tang, i)
    INCLUDE 'ABA_PARAM.INC'
    DIMENSION tang(3,3), Temp_Diff_Help(3,3)
    DOUBLE PRECISION Gam_n, Gam_t, alph, beta, m, n, dn, dt, &
        dGtn, dGnt, deln_max, delt_max, delt1, delt2, &
        UTol, deln, NSlopeInit, Gn, Gt, delt, NORMAL, SHEAR, &
        DeltTbar, DeltNbar, dTt_dn, tang, Temp_Diff_Help
    INTEGER i
    Temp_Diff_Help(1,1)=0.0; Temp_Diff_Help(1,2)=0.0; Temp_Diff_Help(1,3)=0.0
    Temp_Diff_Help(2,1)=0.0; Temp_Diff_Help(2,2)=0.0; Temp_Diff_Help(2,3)=0.0
    Temp_Diff_Help(3,1)=0.0; Temp_Diff_Help(3,2)=0.0; Temp_Diff_Help(3,3)=0.0
    call DiffHelp2 (Gam_n, Gam_t, alph, beta, m, n, &
        dn, dt, dGtn, dGnt, deln_max, delt_max, &
        UTol, NSlopeInit, Gn, Gt, Gam_n, Gam_t, &
        DeltNbar, DeltTbar, deln, delt1, delt2, tang, i)
    delt = (delt1*delt1 + delt2*delt2)**0.5
    NORMAL = 0.0
    SHEAR = 0.0
    dTt_dn = 0.0
    call EvalNormal (m, alph, n, beta, delt, dt, deln_max, dn, &
        Gam_t, Gam_n, DeltTbar, Gn, Gt, &
        NORMAL, NSlopeInit)
    call EvalShear (m, alph, n, beta, abs(delt_max), dt, deln, dn, &
        Gam_t, Gam_n, DeltNbar, Gn, Gt, &
        SHEAR)
    if ((deln.GT.0) .AND. ((deln_max-deln).GT.UTol)) then

        call DiffHelp2 (Gam_n, Gam_t, alph, beta, m, n, &
        dn, dt, dGtn, dGnt, deln_max, delt_max, &
        UTol, NSlopeInit, Gn, Gt, Gam_n, Gam_t, &
        DeltNbar, DeltTbar, deln_max, delt1, delt2, Temp_Diff_Help, i)

        tang(3,1) = deln*Temp_Diff_Help(3,1)/deln_max
        tang(3,2) = deln*Temp_Diff_Help(3,2)/deln_max
        tang(3,3) = NORMAL / deln_max
    endif
    if (abs(delt_max)-delt .GT. UTol) then
        call DiffdTt_dn (m, alph, n, beta, abs(delt_max), dt, deln, dn, &
                Gam_t, Gam_n, dTt_dn)
        tang(1,1) = SHEAR / delt_max; tang(1,2) = 0.0; tang(1,3) = delt1 * dTt_dn /
delt_max
        tang(2,1) = 0.0; tang(2,2) = tang(1,1); tang(2,3) = delt2 * dTt_dn / delt_max
    endif
    RETURN
    END
! ======== take second derivatives ==========
    SUBROUTINE DiffHelp2 (Gam_n, Gam_t, alph, beta, m, n, dn, dt, dGtn, &
                         dGnt, deln_max, delt_max, UTol, NSlopeInit, Gn, Gt, &
                         DeltNbar, DeltTbar, deln, delt1, delt2, tang, i)
    INCLUDE 'ABA_PARAM.INC'
    DIMENSION tang(3,3)
    DOUBLE PRECISION Gam_n, Gam_t, alph, beta, m, n, dn, dt, dGtn, dGnt, &
        deln_max, delt_max, delt1, delt2, UTol, deln, NSlopeInit, Gn, Gt, delt, &
        n1, n2, t1, t2, t3, t4, b1, b2, b3, b4, b5, b6, c1, c2, c3, c4, &
        d1, d2, d3, d4, d5, e1, e2, e3, e4, e5, a1, a2, a3, a4, a5, a6, &
        a7, a8, a9, ediff, mediff, tang
    INTEGER i
    if ((Gn-Gt) .GT. 0) then
        ediff = (Gn-Gt)
    else
        ediff = 0
    endif
    if (-(Gn-Gt) .GT. 0) then
        mediff = -(Gn-Gt)
    else
        mediff = 0
```

```
      endif
      delt = (delt1*delt1 + delt2*delt2)**0.5
      n1 = 1 - deln/dn
      n2 = m/alph + deln/dn
      t1 = 1 - delt/dt
      t2 = n/beta + delt/dt
      t3 = dt-delt
      t4 = n*dt + beta*delt
      if (delt .NE. 0) then
          a1 = Gam_t / (dt*dt * delt*delt)
          a2 = Gam_n * (n1**alph) * (n2**m) + ediff
          a3 = n * beta * (t1**beta) * (t2**(n-1)) / t1
          a4 = n * (n-1) * (t1**beta) * (t2**(n-1)) / t2
          a5 = beta * (beta-1) * (t1**(beta-1)) * (t2**n) / t1
          a6 = beta * n * (t1**(beta-1)) * (t2**n) / t2
          a7 = n*(t1**beta)*(t2**(n-1)) - beta*(t1**(beta-1))*(t2**(n))
          a8 = Gam_t / (dt * delt)
          a9 = Gam_t / (dt * ((delt1*delt1+delt2*delt2)**1.5))
          tang(1,1) = a2*(delt1*delt1*a1*(-a3+a4+a5-a6)+a7*(a8-delt1*delt1*a9))
          tang(2,2) = a2*(delt2*delt2*a1*(-a3+a4+a5-a6)+a7*(a8-delt2*delt2*a9))
          b1 = Gam_t * delt1 * delt2 * beta * (n+beta) * &
                  (Gam_n * (n1**alph) * (n2**m) + ediff)
          b2 = (t1**beta) * (t2**n)
          b3 = beta * b2 / (t3*t3*t4*delt)
          b4 = n * beta * b2 / (t3*t4*t4*delt)
          b5 = beta * b2 / (t3*t4*t4*delt)
          b6 = b2 / (t3*t3*t4*delt)
          tang(2,1) = b1 * (b3 - b4 + b5 - b6)
          tang(1,2) = tang(2,1)
          c1 = Gam_t * Gam_n / (dt*dn*delt)
          c2 = n * (t1**beta) * (t2**(n-1)) - beta * &
                  (t1**(beta-1)) * (t2**n)
          c3 = alph * (n1**alph) * (n2**m) / n1
          c4 = m * (n1**alph) * (n2**m) / n2
          tang(3,1) = delt1 * c1 *c2 * (-c3 + c4)
          tang(1,3) = tang(3,1)
          tang(3,2) = delt2 * c1 *c2 * (-c3 + c4)
          tang(2,3) = tang(3,2)
      else
          tang(1,2) = 0.0; tang(1,3) = 0.0
          tang(2,1) = 0.0; tang(2,3) = 0.0
          tang(3,1) = 0.0; tang(3,2) = 0.0
          e1 = n * beta * (t1**beta) * (t2**(n-1)) / t1
          e2 = n * (n-1) * (t1**beta) * (t2**(n-1)) / t2
          e3 = beta * (beta-1) * (t1**(beta-1)) * (t2**n) / t1
          e4 = n * beta * (t1**(beta-1)) * (t2**n) / t2
          e5 = Gam_n * (n1**alph) * (n2**m) + ediff
          tang(1,1) = Gam_t * (-e1+e2+e3-e4) * e5 / (dt*dt)
          tang(2,2) = tang(1,1)
      endif
      d1 = Gam_t * (t1**beta) * (t2**n) + mediff
      d2 = m * alph * (n1**alph) * (n2**(m-1)) / n1
      d3 = m * (m-1) * (n1**alph) * (n2**(m-1)) / n2
      d4 = alph * (alph-1) * (n1**(alph-1)) * (n2**m) / n1
      d5 = alph * m * (n1**(alph-1)) * (n2**m) / n2
      tang(3,3) = Gam_n * d1 * (-d2+d3+d4-d5) / (dn*dn)
      RETURN
      END
! ======== calculate Dnn ==========
      SUBROUTINE DiffdTt_dn (m, alph, n, beta, delt, dt, deln, dn, &
          Gam_t, Gam_n, dTt_dn)
      INCLUDE 'ABA_PARAM.INC'
      DOUBLE PRECISION m, alph, n, beta, delt, dt, deln, dn, n0, n1, &
          t0, t1, a1, a2, a3, Gam_t, Gam_n, dTt_dn
      n0 = 1 - deln/dn
      n1 = m/alph + deln/dn
      t0 = 1 - delt/dt
      t1 = n/beta + delt/dt
      a1 = n * (t0**beta) * (t1**(n-1)) - beta * (t0**(beta-1)) * (t1**n)
```

```
      a2 = alph * (n0**alph) * (n1**m) / n0
      a3 = m * (n0**alph) * (n1**m) / n1
      dTt_dn = Gam_t * Gam_n * a1 * (a3-a2) / (dn*dt)
      RETURN
      END
!  ======== evaluate tangential tractions ==========
      SUBROUTINE EvalShear (m, alph, n, beta, delt, dt, deln, dn, &
          Gam_t, Gam_n, DeltNbar, Gn, Gt, SHEAR)
      INCLUDE 'ABA_PARAM.INC'
      DOUBLE PRECISION m, alph, n, beta, delt, dt, deln, dn, n0, n1, &
          t0, t1, b0, b1, b2, Gam_t, Gam_n, ediff, SHEAR, sign1, &
          dtt, DeltNbar, Gn, Gt
      if (delt .GE. 0) then
          sign1 = 1
      else
          sign1 = -1
      endif
      dtt = abs(delt)
      if ((deln .GE. DeltNbar) .OR. (dtt .GE. dt)) then
          SHEAR = 0
          RETURN
      endif
      n0 = 1 - deln/dn
      t0 = 1 - dtt/dt
      n1 = m/alph + deln/dn
      t1 = n/beta + dtt/dt
      if (deln .LT. 0) then
          n0 = 1
          n1 = m/alph
      endif
      b0 = n * (t0**beta) * (t1**(n-1))
      b1 = beta * (t0**(beta-1)) * (t1**n)
      b2 = Gam_n * (n0**alph) * (n1**m)
      if ((Gn-Gt) .GT. 0) then
          ediff = (Gn-Gt)
      else
          ediff = 0
      endif
      SHEAR = (Gam_t/dt) * (b0-b1) * (b2+ediff) * sign1
      RETURN
      END
!  ======== evaluate the normal tractions ==========
      SUBROUTINE EvalNormal (m, alph, n, beta, delt, dt, deln, dn, &
                        Gam_t, Gam_n, DeltTbar, Gn, Gt, NORMAL, NSlopeInit)
      INCLUDE 'ABA_PARAM.INC'
      DOUBLE PRECISION m, alph, n, beta, delt, dt, deln, dn, n0, n1, &
          t0, t1, a0, a1, a2, Gam_t, Gam_n, ediff, DeltTbar, NORMAL, Gn, &
          Gt, NSlopeInit
      n0 = 1 - deln/dn
      t0 = 1 - abs(delt)/dt
      if (deln .LE. 0) then
          NORMAL = deln*NSlopeInit
          RETURN
      elseif ((deln .GE. dn) .OR. (abs(delt) .GE. DeltTbar)) then
          NORMAL = 0
          RETURN
      endif
      n1 = m/alph + deln/dn
      t1 = n/beta + abs(delt)/dt
      a0 = m * (n0**alph) * (n1**(m-1))
      a1 = alph * (n0**(alph-1)) * (n1**m)
      a2 = Gam_t * (t0**beta) * (t1**n)
      if (-(Gn-Gt) .GT. 0) then
          ediff = -(Gn-Gt)
      else
          ediff = 0
      endif
      NORMAL = (Gam_n/dn) * (a0-a1) * (a2+ediff)
      if (NORMAL .LT. 0) then
```

```
        NORMAL = 0
    endif
    RETURN
    END
! ======== calculate normal conjugate final crack opening width ==========
    SUBROUTINE FindConjugateDeltNb (Gam_n, dn, alph, m, Gn, Gt, DeltNbar)
    INCLUDE 'ABA_PARAM.INC'
    DOUBLE PRECISION dn, Gam_n, alph, m, Gn, Gt, DeltNbar, x0, &
                x1, tol, xm, f_x0, f_xm, sign_diff
    x0 = 0
    x1 = dn
    tol = 0.00000005
    if ( (Gn-Gt) .GE. 0 ) then
        sign_diff = Gn-Gt
    elseif ( (Gn-Gt) .LT. 0 ) then
        sign_diff = 0
    endif
    if (Gn .GT. Gt) then
        do while ((x1-x0).GT.tol)
                xm = x0+(x1-x0)/2
                f_x0 = Gam_n * ((1-x0/dn)**alph) * (((m/alph)+&
                        (x0/dn))**m) + sign_diff
                f_xm = Gam_n * ((1-xm/dn)**alph) * (((m/alph)+&
                        (xm/dn))**m) + sign_diff
                if ( (f_x0 .GT. 0 .AND. f_xm .GT. 0) .OR. &
                     (f_x0 .LT. 0 .AND. f_xm .LT. 0) .OR. &
                     (f_x0 .EQ. 0.0 .AND. f_xm .EQ. 0.0)) then
                       x0 = xm
                else
                       x1 = xm
                endif
        end do
        DeltNbar = xm
    elseif (Gn .LE. Gt) then
        DeltNbar = dn
    endif
    RETURN
    END
! ======== calculate tangential conjugate final crack opening width ==========
    SUBROUTINE FindConjugateDeltTb (Gam_t, dt, beta, n, Gn, Gt, DeltTbar)
    INCLUDE 'ABA_PARAM.INC'
    DOUBLE PRECISION dt, Gam_t, beta, n, Gn, Gt, DeltTbar, x0, &
                x1, tol, xm, f_x0, f_xm, sign_diff
    x0 = 0
    x1 = dt
    tol = 0.00000005
    if ( (Gt-Gn) .GE. 0 ) then
        sign_diff = Gt-Gn
    elseif ( (Gt-Gn) .LT. 0 ) then
        sign_diff = 0
    endif
    if (Gt .GT. Gn) then
        do while ((x1-x0).GT.tol)
                xm = x0+(x1-x0)/2
                f_x0 = Gam_t * ((1-abs(x0)/dt)**beta) * (((n/beta)+&
                        (abs(x0)/dt))**n) + sign_diff
                f_xm = Gam_t * ((1-abs(xm)/dt)**beta) * (((n/beta)+&
                        (abs(xm)/dt))**n) + sign_diff
                if ( (f_x0 .GT. 0 .AND. f_xm .GT. 0) .OR. &
                     (f_x0 .LT. 0 .AND. f_xm .LT. 0) .OR. &
                     (f_x0 .EQ. 0.0 .AND. f_xm .EQ. 0.0)) then
                       x0 = xm
                else
                       x1 = xm
                endif
        end do
        DeltTbar = xm
    elseif (Gn .LE. Gt) then
        DeltTbar = dt
```

```
      endif
      RETURN
      END
! ======== calculate rotation matrix (R) and determinant of the Jacobian (DJ) ==========

      SUBROUTINE get_rotation (R, DJ, COORDS, U, ndofel, nnode, mcrd, xi, eta)
      INCLUDE 'ABA_PARAM.INC'
      DIMENSION R_j(mcrd,mcrd), R(mcrd,mcrd), COORDS(mcrd,nnode), U(ndofel)
      DIMENSION Co_de(mcrd,nnode)
      DOUBLE PRECISION xi, eta, x1, x2, x3, x4, y1, y2, y3 ,y4, z1, z2, z3, z4, &
                  DJ, mag1, mag2, mag3, R_j, R, Co_de, dN1eta, dN2eta, dN3eta, &
                  dN4eta, dN1xi, dN2xi, dN3xi, dN4xi, COORDS, U
      ! Deformed configuration coordinates
      do i = 1, mcrd
          do j = 1, nnode
                Co_de(i,j) = COORDS(i,j) + U(3*(j-1)+i)
          end do
      end do
      ! mid-point at the deformed configuration
      x1 = (Co_de(1,1) + Co_de(1,5))*0.5
      y1 = (Co_de(2,1) + Co_de(2,5))*0.5
      z1 = (Co_de(3,1) + Co_de(3,5))*0.5
      x2 = (Co_de(1,2) + Co_de(1,6))*0.5
      y2 = (Co_de(2,2) + Co_de(2,6))*0.5
      z2 = (Co_de(3,2) + Co_de(3,6))*0.5
      x3 = (Co_de(1,3) + Co_de(1,7))*0.5
      y3 = (Co_de(2,3) + Co_de(2,7))*0.5
      z3 = (Co_de(3,3) + Co_de(3,7))*0.5
      x4 = (Co_de(1,4) + Co_de(1,8))*0.5
      y4 = (Co_de(2,4) + Co_de(2,8))*0.5
      z4 = (Co_de(3,4) + Co_de(3,8))*0.5
      ! derivative of shape functions
      dN1xi = eta/4 - 0.25
      dN2xi = -eta/4 + 0.25
      dN3xi = eta/4 + 0.25
      dN4xi = -eta/4 - 0.25
      dN1eta = xi/4 - 0.25
      dN2eta = -xi/4 - 0.25
      dN3eta = xi/4 + 0.25
      dN4eta = -xi/4 + 0.25
      ! calculate Jacobian
      R_j(1,1) = dN1xi*x1 + dN2xi*x2 + dN3xi*x3 + dN4xi*x4
      R_j(1,2) = dN1xi*y1 + dN2xi*y2 + dN3xi*y3 + dN4xi*y4
      R_j(1,3) = dN1xi*z1 + dN2xi*z2 + dN3xi*z3 + dN4xi*z4
      R_j(2,1) = dN1eta*x1 + dN2eta*x2 + dN3eta*x3 + dN4eta*x4
      R_j(2,2) = dN1eta*y1 + dN2eta*y2 + dN3eta*y3 + dN4eta*y4
      R_j(2,3) = dN1eta*z1 + dN2eta*z2 + dN3eta*z3 + dN4eta*z4
      R_j(3,1) = (dN1xi*y1 + dN2xi*y2 + dN3xi*y3 + dN4xi*y4)*(dN1eta*z1 &
             + dN2eta*z2 + dN3eta*z3 + dN4eta*z4) - (dN1eta*y1 + dN2eta*y2 &
             + dN3eta*y3 + dN4eta*y4)*(dN1xi*z1 + dN2xi*z2 + dN3xi*z3 + dN4xi*z4)
      R_j(3,2) = (dN1eta*x1 + dN2eta*x2 + dN3eta*x3 + dN4eta*x4)*(dN1xi*z1 &
             + dN2xi*z2 + dN3xi*z3 + dN4xi*z4) - (dN1xi*x1 + dN2xi*x2 + dN3xi*x3 &
             + dN4xi*x4)*(dN1eta*z1 + dN2eta*z2 + dN3eta*z3 + dN4eta*z4)
      R_j(3,3) = (dN1xi*x1 + dN2xi*x2 + dN3xi*x3 + dN4xi*x4)*(dN1eta*y1 + dN2eta*y2 &
             + dN3eta*y3 + dN4eta*y4) - (dN1eta*x1 + dN2eta*x2 + dN3eta*x3 &
             + dN4eta*x4)*(dN1xi*y1 + dN2xi*y2 + dN3xi*y3 + dN4xi*y4)
      ! get determinant of Jacobian
      DJ = R_j(1,1)*R_j(2,2)*R_j(3,3) + R_j(1,2)*R_j(2,3)*R_j(3,1) + &
           R_j(1,3)*R_j(2,1)*R_j(3,2) - R_j(1,3)*R_j(2,2)*R_j(3,1) - &
           R_j(1,2)*R_j(2,1)*R_j(3,3) - R_j(1,1)*R_j(2,3)*R_j(3,2)
      DJ = (((R_j(3,1))**2+(R_j(3,2))**2+(R_j(3,3))**2)**0.5)
      ! get un-normalized rotation matrix
      R(1,1) = R_j(1,1); R(1,2) = R_j(1,2); R(1,3) = R_j(1,3)    ! first row
      R(3,1) = R_j(3,1); R(3,2) = R_j(3,2); R(3,3) = R_j(3,3)    ! third row
      R(2,1) = R_j(1,2)*R_j(3,3)-R_j(3,2)*R_j(1,3)               ! second row
      R(2,2) = -R_j(1,1)*R_j(3,3)+R_j(3,1)*R_j(1,3)              !    .
      R(2,3) = R_j(1,1)*R_j(3,2)-R_j(3,1)*R_j(1,2)               !    .
      ! normalize rows of R to get rotation matrix
      mag1 = (((R(1,1))**2+(R(1,2))**2+(R(1,3))**2)**0.5)
```

```
    mag2 = (((R(2,1))**2+(R(2,2))**2+(R(2,3))**2)**0.5)
    mag3 = (((R(3,1))**2+(R(3,2))**2+(R(3,3))**2)**0.5)
    R(1,1) = R(1,1)/mag1; R(1,2) = R(1,2)/mag1; R(1,3) = R(1,3)/mag1
    R(2,1) = R(2,1)/mag2; R(2,2) = R(2,2)/mag2; R(2,3) = R(2,3)/mag2
    R(3,1) = R(3,1)/mag3; R(3,2) = R(3,2)/mag3; R(3,3) = R(3,3)/mag3
    RETURN
    END
! ======== calculate the B matrix ==========
    SUBROUTINE get_B (L, Bc, R, xi, eta)
    INCLUDE 'ABA_PARAM.INC'
    DIMENSION Bc(3,24), R(3,3), L(3,24)
    DOUBLE PRECISION xi, eta, N1, N2, N3, N4, Bc, L, R
    INTEGER i, j, k
    ! initialize Bc with zeros
    do i = 1,3
        do j = 1,24
                Bc(i,j) = 0.0
        end do
    end do
    ! initialize L with zeros
    do i = 1,3
        do j = 1,24
                L(i,j) = 0.0
        end do
    end do
    ! Shape Functions
    N1 = 0.25*(1-xi)*(1-eta)
    N2 = 0.25*(1+xi)*(1-eta)
    N3 = 0.25*(1+xi)*(1+eta)
    N4 = 0.25*(1-xi)*(1+eta)
    ! Relation matrix
    L(1,1)=-N1; L(1,4)=-N2; L(1,7)=-N3; L(1,10)=-N4; L(1,13)=N1; L(1,16)=N2; L(1,19)=N3;
L(1,22)=N4
    L(2,2)=-N1; L(2,5)=-N2; L(2,8)=-N3; L(2,11)=-N4; L(2,14)=N1; L(2,17)=N2; L(2,20)=N3;
L(2,23)=N4
    L(3,3)=-N1; L(3,6)=-N2; L(3,9)=-N3; L(3,12)=-N4; L(3,15)=N1; L(3,18)=N2; L(3,21)=N3;
L(3,24)=N4
    ! Matrix multiplication to get B matrix
    do i = 1, 3
        do j = 1, 24
                do k = 1, 3
                        Bc(i,j) = Bc(i,j) + R(i,k) * L(k,j)
                end do
        end do
    end do
    RETURN
    END
```

BIBLIOGRAPHY

[1] Dugdale D. Yielding of Steel Sheets Containing Slits. J Mech Phys Solids 1960;8:100–4.

[2] Barenblatt GI. The Mathematical Theory of Equilibrium Cracks in Brittle Fracture. Adv Appl Mech 1962;7:55–129.

[3] Hillerborg A, Modeer M, Petersson P. Analysis of Crack Formation and Crack Growth in Concrete by Means of Fracture Mechanics and Finite Elements. Cem Concr Res 1976;6:773–81.

[4] Boone TJ, Wawrzynek PA, Ingraffea AR. Simulation of the Fracture Processes in Rock with Application to Hydrofracturing. Int J Rock Mech Min Sci 1986;23:255–65.

[5] Needleman A. A Continuum Model for Void Nucleation by Inclusion Debonding. J Appl Mech 1987;54:525–31.

[6] Iesulauro E. Decohesion of Grain Boundaries in Statistical Representations of Aluminum Polycrystals. Cornell University, 2006.

[7] Tvergaard V, Hutchinson JW. The Relation Between Crack Growth Resistance and Fracture Process Parameters in Elastic-Plastic Solids. J Mech Phys Solids 1992;40:1377–97.

[8] Scheider I, Brocks W. Simulation of Cup-Cone Fracture Using the Cohesive Model. Eng Fract Mech 2003;70:1943–61.

[9] Ingraffea AR, Gerstle WH, Gergely P, Saouma V. Fracture Mechanics of Bond in Reinforced Concrete. J Struct Eng 1984;110:871–90.

[10] Elices M, Guinea GV, Gomez J, Planas J. The Cohesive Zone Model: Advantages, Limitations and Challenges. Eng Fract Mech 2002;69:137–63.

[11] Park K, Paulino GH, Roesler J. Cohesive Fracture Model for Functionally Graded Fiber Reinforced Concrete. Cem Concr Res 2010;40:956–65.

[12] Tomar V. Modeling of Dynamic Fracture and Damage in Two-Dimensional Trabecular Bone Microstructures Using the Cohesive Finite Element Method. J Biomech Eng 2008;130:1–10.

[13] Ural A, Vashishth D. Cohesive Finite Element Modeling of Age-Related Toughness Loss in Human Cortical Bone. J Biomech 2006;39:2974–82.

[14] Zhang ZJ, Zhang P, Li LL, Zhang ZF. Fatigue Cracking at Twin Boundaries : Effects of Crystallographic Orientation and Stacking Fault Energy. Acta Mater 2012;60:3113–27.

[15] Song SH, Paulino GH, Buttlar WG. A Bilinear Cohesive Zone Model Tailored for Fracture of Asphalt Concrete Considering Viscoelastic Bulk Material. Eng Fract Mech 2006;73:2829–48.

[16] Hui CY, Ruina A, Long R, Jagota A. Cohesive Zone Models and Fracture. J Adhes 2011;87:1–52.

[17] Park K, Paulino GH. Cohesive Zone Models: A Critical Review of Traction-Separation Relationships Across Fracture Surfaces. Appl Mech Rev 2013;64:060802.

[18] Tvergaard V. Material Failure by Void Growth to Coalescence. Adv Appl Mech 1990;27:83–151.

[19] Needleman A. An Analysis of Tensile Decohesion Along an Interface. J Mech Phys Solids 1990;38:289–324.

[20] Xu XP, Needleman A. Void nucleation by inclusion debonding in a crystal matrix. Model Simul Mater Sci Eng 1993;1:111–32.

[21] Park K, Paulino GH, Roesler JR. A Unified Potential-Based Cohesive Model of Mixed-Mode Fracture. J Mech Phys Solids 2009;57:891–908.

[22] Heber G, Schneider D, Wawrzynek P. Finite Element All-Wheel Drive (FEAWD) n.d.

[23] Balay S, Gropp WD, McInnes LC, Smith BF. Efficient Management of Parallelism in Object-Oriented Numerical Software Libraries. Mod. Softw. Tools Sci. Comput., Birkhäuser Boston; 1997, p. 163–202.

[24] Balay S, Brown J, Buschelman K, Eijkhout V, Gropp WD, Kaushik D, et al. PETSc Users Manual 2010.

[25] Balay S, Brown J, Buschelman K, Gropp WD, Kaushik D, Knepley MG, et al. PETSc Web Page 2011.

[26] Alfano M, Furgiuele F, Lubineau G, Paulino GH. Simulation of Debonding in Al/Epoxy T-Peel Joints Using a Potential-Based Cohesive Zone Model. Procedia Eng 2011;10:1760–5.

[27] Alfano M, Lubineau G, Furgiuele F, Paulino GH. On the Enhancement of Bond Toughness for Al/Epoxy T-Peel Joints with Laser Treated Substrates. Int J Fract 2011;171:139–50.

[28] Rice JR. Mathematical Analysis in the Mechanics of Fracture. In: Liebowitz H, editor. Fract. An Adv. Treatise, vol. 2, Academic Press; 1968, p. 191–311.

[29] ASTM. Standard Test Method for Mixed Mode I–Mode II Interlaminar Fracture Toughness of Unidirectional Fiber Reinforced Polymer Matrix Composites. 2006.

[30] Reeder JR, Crews Jr. JH. Mixed-Mode Bending Method for Delamination Testing. Am Inst Aeronaut Astronaut J 1990;28:1270–6.

[31] Mi Y, Crisfield MA, Davies GAO, Hellweg HB. Progressive Delamination Using Interface Elements. J Compos Mater 1998;32:1246–72.

[32] Ratcliffe JG. Characterization of the Edge Crack Torsion (ECT) Test for Mode III Fracture Toughness Measurement of Laminated Composites. 2004.

[33] Krueger R, O'Brien T. Analysis of Flexure Tests for Transverse Tensile Strength Characterization of Unidirectional Composites. J Compos Technol Res 2003;25:11231.

[34] Igi S, Kawaguchi S, Suzuki N. Running Ductile Fracture Analysis for X80 Pipeline in JGA Burst Tests. Pipeline Technol. Conf., Ostend, Belgium: 2009.

[35] Nonn A, Kalwa C. Modeling of Damage Behavior of High Strength Pipeline Steel. 18th Eur. Conf. Fract., Dresden, Germany: 2010.

[36] ASTM. Standard Test Method for Drop-Weight Tear Tests of Ferritic Steel. 2008.

[37] API. Recommended Practice for Conducting Drop Weight Tear Tests on Line Pipe. 1996.

[38] EN. Metallic Materials – Drop Weight Tear Test. 1999.

[39] Nègre P, Steglich D, Brocks W. Crack Extension at an Interface: Prediction of Fracture Toughness and Simulation of Crack Path Deviation. Int J Fract 2005;134:209–29.

[40] Roy YA, Dodds RH. Simulation of Ductile Crack Growth in Thin Aluminum Panels Using 3-D Surface Cohesive Elements. Int J Fract 2001;110:21–45.

[41] Scheider I, Schödel M, Brocks W, Schönfeld W. Crack Propagation Analyses with CTOA and Cohesive Model: Comparison and Experimental Validation. Eng Fract Mech 2006;73:252–63.

[42] Raj R, Ashby MF. Intergranular Fracture at Elevated Temperatures. Acta Metall 1975;23:653–66.

[43] Groeber M, Ghosh S, Uchic MD, Dimiduk DM. A Framework for Automated Analysis and Simulation of 3D Polycrystalline Microstructures. Part 1: Statistical Characterization. Acta Mater 2008;56:1257–73.

[44] Groeber M, Ghosh S, Uchic MD, Dimiduk DM. A Framework for Automated Analysis and Simulation of 3D Polycrystalline Microstructures. Part 2: Synthetic Structure Generation. Acta Mater 2008;56:1274–87.

[45] Christodoulou L, Larsen JM. Using Materials Prognosis to Maximize the Utilization Potential of Complex Mechanical Systems. JOM 2004;56:15–9.

[46] Glaessgen E, Stargel D. The Digital Twin Paradigm for Future NASA and U.S. Air Force Vehicles. 53rd Struct. Struct. Dyn. Mater. Conf. Spec. Sess. Digit. Twin, Honolulu: 2012, p. 1–14.

[47] Tuegel EJ, Ingraffea AR, Eason TG, Spottswood SM. Reengineering Aircraft Structural Life Prediction Using a Digital Twin. Int J Aerosp Eng 2011;2011:1–14.

[48] Boyce BL, Kramer SLB, Fang HE, Cordova TE, Neilsen MK, Dion K, et al. The Sandia Fracture Challenge: Blind Round Robin Predictions of Ductile Tearing. Int J Fract 2014;186:5–68.

[49] Wojtkiewicz SF, Eldred MS, Field R V, Urbina A, Red-Horse JR. Uncertainty Quantification In Large Computational Engineering Models. Proc. 42rd AIAA/ASME/ASCE/AHS/ASC Struct. Struct. Dyn. Mater. Conf., Seattle: 2001, p. 1–11.

[50] Assessing the Reliability of Complex Models: Mathematical and Statistical Foundations of Verification, Validation, and Uncertainty Quantification. Washington, D.C.: 2013.

[51] Kent E. The Brains of Men and Machines. 1st ed. Peterborough, NH: BYTE / McGraw Hill; 1981.

[52] Gross AJ, Ravi-Chandar K. Prediction of Ductile Failure Using a Local Strain-to-Failure Criterion. Int J Fract 2014;186:69–91.

[53] Nahshon K, Miraglia M, Cruce J, DeFrese R, Moyer ET. Prediction of the Sandia Fracture Challenge Using a Shear Modified Porous Plasticity Model. Int J Fract 2013;186:93–105.

[54] Pack K, Luo M, Wierzbicki T. Sandia Fracture Challenge: Blind Prediction and Full Calibration to Enhance Fracture Predictability. Int J Fract 2014.

[55] Zhang T, Fang E, Liu P, Lua J. Modeling and Simulation of 2012 Sandia Fracture Challenge Problem: Phantom Paired Shell for Abaqus and Plane Strain Core Approach. Int J Fract 2013;186:117–39.

[56] Simulia. Abaqus 6.11 User Manual. Providence, RI: 2011.

[57] Gurson AL. Continuum Theory of Ductile Rupture by Void Nucleation and Growth: Part I—Yield Criteria and Flow Rules for Porous Ductile Media. J Eng Mater Technol 1977;99:2.

[58] Tvergaard V. Influence of Voids on Shear Band Instabilities Under Plane Strain Conditions. Int J Fract 1981;17:389–407.

[59] Courant R, Friedrichs K, Lewy H. On the Partial Difference Equations of Mathematical Physics. IBM J Res Dev 1967;11:215–34.

[60] Nahshon K, Hutchinson JW. Modification of the Gurson Model for Shear Failure. Eur J Mech - A/Solids 2008;27:1–17.

[61] Chabanet O, Steglich D, Besson J, Heitmann V, Hellmann D, Brocks W. Predicting Crack Growth Resistance of Aluminium Sheets. Comput Mater Sci 2003;26:1–12.

[62] Rider WJ, Kamm JR, Weirs VG. Verification , Validation and Uncertainty Quantification Workflow in CASL. Sandia National Labs. Albuquerque: 2010.

[63] Tvergaard V, Needleman A. Analysis of the Cup-Cone Fracture in a Round Tensile Bar. Acta Metall 1984;32:157–69.

[64] Brocks W, Klingbeil D, Kunecke G, Sun D-Z. Application of the Gurson Model to Ductile Tearing Resistance. Consttraint Eff. Fract. Theory Appl. Second Vol., Philadelphia: ASTM; 1995, p. 232–54.

[65] Krueger D, Kissinger R. Fatigue Crack Growth Resistant Nickel-Base Article and Alloy and Method for Making. 4957567, 1990.

[66] Mazur Z, Luna-Ramírez A, Juárez-Islas JA, Campos-Amezcua A. Failure Analysis of a Gas Turbine Blade Made of Inconel 738LC Alloy. Eng Fail Anal 2005;12:474–86.

[67] Findley KO, Saxena A. Low cycle Fatigue in Rene 88DT at 650 °C: Crack Nucleation Mechanisms and Modeling. Metall Mater Trans A 2006;37:1469–75.

[68] Miao J, Pollock TM, Wayne Jones J. Crystallographic Fatigue Crack Initiation in Nickel-Based Superalloy René 88DT at Elevated Temperature. Acta Mater 2009;57:5964–74.

[69] Lim LC. Slip-Twin Interactions in Nickel at 573K at Large Strains. Scr Metall 1984;18:1139–42.

[70] Konopka K, Wyrzykowski JW. The Effect of the Twin Boundaries on the Yield Stress of a Material. J Mater Process Technol 1997;64:223–30.

[71] Pande CS, Rath BB, Imam MA. Effect of Annealing Twins on Hall – Petch Relation in Polycrystalline Materials. Mater Sci Eng A 2004;367:171–5.

[72] Li JCM. Petch relation and grain boundary sources. Trans TMS-AIME 1963;277:239–47.

[73] Thompson N, Wadsworth N, Louat N. The Origin of Fatigue Fracture in Copper. Philos Mag 1956;1:113–26.

[74] Boettner RC, McEvily AJ, Liu YC. On the Formation of Fatigue Cracks at Twin Boundaries. Philos Mag 1964;10:95–106.

[75] Stein C, Lee S, Rollett A. An Analysis of Fatigue Crack Initiation Using 2D Orientation Mapping and Full-Field Simulation of Elastic Stress Response. Superalloys 2012, Champion, PA: 2012.

[76] Heinz A, Neumann P. Crack Initiation During High Cycle Fatigue of an Austenitic Steel. Acta Metall Mater 1990;38:1933–40.

[77] Neumann P. Analytical Solution for the Incompatibility Stresses at Twin Boundaries in Cubic Crystals. Fatigue 99, Beijing: 1999, p. 107–14.

[78] Stein C, Cerrone A, Ozturk T, Lee S, Kenesei P, Tucker H, et al. Fatigue Crack Initiation, Slip Localization and Twin Boundaries in a Nickel-Based Superalloy. Curr Opin Solid State Mater Sci 2014.

[79] Gabb T, Gayda J, Telesman J, Kantzos P. Thermal and Mechanical Property Characterization of the Advanced Disk Alloy LSHR 2005.

[80] Johnson DA, John R. Room Temperature Tension Test Results Alloy: LSHR. 2012.

[81] Poulsen HF, Nielsen SF, Lauridsen EM, Schmidt S, Suter RM, Lienert U, et al. Three-Dimensional Maps of Grain Boundaries and the Stress State of Individual Grains in Polycrystals and Powders. J Appl Crystallogr 2001;34:751–6.

[82] Suter RM, Hennessy D, Xiao C, Lienert U. Forward Modeling Method for Microstructure Reconstruction Using X-Ray Diffraction Microscopy : Single-Crystal Verification. Rev Sci Instrum 2006;77:123905.

[83] Li SF, Suter RM. Adaptive Reconstruction Method for Three-Dimensional Orientation Imaging. J Appl Crystallogr 2013;46:512–24.

[84] MacSleyne JP, Simmons JP, De Graef M. On the Use of Moment Invariants for the Automated Analysis of 3D Particle Shapes. Model Simul Mater Sci Eng 2008;16:045008.

[85] Miao J, Pollock TM, Wayne Jones J. Microstructural Extremes and the Transition from Fatigue Crack Initiation to Small Crack Growth in a Polycrystalline Nickel-Base Superalloy. Acta Mater 2012;60:2840–54.

[86] Matouš K, Maniatty AM. Finite Element Formulation for Modelling Large Deformations in Elasto-Viscoplastic Polycrystals. Int J Numer Methods Eng 2004;60:2313–33.

[87] Beaudoin AJ, Acharya A, Chen SR, Korzekwa DA, Stout MG. Consideration of Grain-Size Effect and Kinetics in the Plastic Deformation of Metal Polycrystals. Acta Mater 2000;48:3409–23.

[88] Voce E. A Practical Strain-Hardening Function. Metallurgica 1955;51:219–26.

[89] Kocks UF. Laws for Work-Hardening and Low-Temperature Creep. ASME, Trans Ser H-Journal Eng Mater Technol 1976;98:76–85.

[90] Ashby MF. The Deformation of Plastically Non-Homogeneous Materials. Philos Mag 1970;21:399–424.

[91] Alers GA, Neighbours JR, Sato H. Temperature Dependent Magnetic Contributions to the High Field Elastic Constants of Nickel and an Fe-Ni Alloy. J Phys Chem Solids 1960;13:40–55.

[92] Wallow F, Neite G, Schröer W, Nembach E. Stiffness Constants, Dislocation Line Energies, and Tensions of Ni3Al and of the γ′-Phases of NIMONIC 105 and of NIMONIC PE16. Phys Status Solidi 1987;99:483–90.

[93] Roth H, Davis C, Thomson R. Modeling Solid Solution Strengthening in Nickel Alloys. Metall Mater Trans A 1997;28:1329–35.

[94] Gypen LA, Deruyttere A. Multi-Component Solid Solution Hardening. J Mater Sci 1977;12:1028–33.

[95] Kozar RW, Suzuki A, Milligan WW, Schirra JJ, Savage MF, Pollock TM. Strengthening Mechanisms in Polycrystalline Multimodal Nickel-Base Superalloys. Metall Mater Trans A 2009;40:1588–603.

[96] Reed C. The Superalloys: Fundamentals and Applications. 1st ed. Cambridge University Press; 2008.

[97] Gleiter H, Hornbogen E. Precipitation Hardening by Coherent Particles. Mater Sci Eng 1967;2:285–302.

[98] Soboyejo W. Mechanical Properties of Engineered Materials. 1st ed. New York: CRC Press; 2002.

[99] Baither D, Rentenberger C, Karnthaler HP, Nembach E. Three Alternative Experimental Methods to Determine the Antiphase-Boundary Energies of the γ′ Precipitates in Superalloys. Philos Mag A 2002;82:1795–805.

[100] Parthasarathy T, Rao S, Dimiduk D. A Fast Spreadsheet Model for the Yield Strength of Superalloys. Superalloys 2004 2004:887–96.

[101] Schänzer S, Nembach E. The Critical Resolved Shear Stress of γ′-Strengthened Nickel-Based Superalloys with γ′-Volume Fractions Between 0.07 and 0.47. Acta Metall Mater 1992;40:803–13.

[102] Fatemi A, Socie DF. A Critical Plane Approach to Multiaxial Fatigue Damage Including Out-of-Phase Loading. Fatigue Fract Eng Mater Struct 1988;11:149–65.

[103] Tschopp MA, McDowell DL. Influence of Single Crystal Orientation on Homogeneous Dislocation Nucleation Under Uniaxial Loading. J Mech Phys Solids 2008;56:1806–30.

[104] Kirane K, Ghosh S. A Cold Dwell Fatigue Crack Nucleation Criterion for Polycrystalline Ti-6242 Using Grain-Level Crystal Plasticity FE Model. Int J Fatigue 2008;30:2127–39.

[105] Ruiz G, Pandolfi A, Ortiz M. Three-Dimensional Cohesive Modeling of Dynamic Mixed-Mode Fracture. Int J Numer Methods Eng 2001;52:97–120.

[106] Simkin B, Crimp M, Bieler T. A Factor to Predict Microcrack Nucleation at γ–γ Grain Boundaries in TiAl. Scr Mater 2003;49:149–54.

[107] Kumar D, Bieler TR, Eisenlohr P, Mason DE, Crimp MA, Roters F, et al. On Predicting Nucleation of Microcracks Due to Slip-Twin Interactions at Grain Boundaries in Duplex Near γ-TiAl. J Eng Mater Technol 2008;130:021012.

[108] Rollett AD, Lebensohn RA, Groeber M, Choi Y, Li J, Rohrer GS. Stress Hot Spots in Viscoplastic Deformation of Polycrystals. Model Simul Mater Sci Eng 2010;18:074005.

[109] Cerrone AR. Parallelized Polycrystal Mesher 2014, <http://www.cfg.cornell.edu/~arc247/PPM/>.

[110] Cavalcante Neto JB, Wawrzynek PA, Carvalho MTM, Martha LF, Ingraffea AR. An Algorithm for Three-Dimensional Mesh Generation for Arbitrary Regions with Cracks. Eng Comput 2001;17:75–91.

[111] Cavalcante-Neto JB, Martha LF, Wawrzynek PA, Ingraffea AR. A Back-Tracking Procedure for Optimization of Simplex Meshes. Commun Numer Methods Eng 2005;21:711–22.

[112] Tucker JC, Chan LH, Rohrer GS, Groeber MA, Rollett AD. Comparison of Grain Size Distributions in a Ni-Based Superalloy in Three and Two Dimensions Using the Saltykov Method. Scr Mater 2012;66:554–7.

[113] Bostock M. Data-Driven Documents, <http://d3js.org/>.